

Ordering and Intermixing at Metallic Interfaces

Thesis submitted for the degree of
Doctor of Philosophy
at the University of Leicester

by

Paul Steadman BSc (Leicester)
Department of Physics and Astronomy
University of Leicester

September 1997

UMI Number: U105873

All rights reserved

INFORMATION TO ALL USERS

The quality of this reproduction is dependent upon the quality of the copy submitted.

In the unlikely event that the author did not send a complete manuscript and there are missing pages, these will be noted. Also, if material had to be removed, a note will indicate the deletion.



UMI U105873

Published by ProQuest LLC 2013. Copyright in the Dissertation held by the Author.
Microform Edition © ProQuest LLC.

All rights reserved. This work is protected against
unauthorized copying under Title 17, United States Code.



ProQuest LLC
789 East Eisenhower Parkway
P.O. Box 1346
Ann Arbor, MI 48106-1346

Intermixing and Ordering at Metallic Interfaces

by

Paul Steadman

Abstract

Using surface X-ray diffraction and synchrotron radiation the growth modes and structures of the metallic systems Cr on Cu(001), Cr on Ag(001) and Fe on Cu(001) have been studied.

The growth of Cr on Cu(001) was found to be disordered at all substrate temperatures. The growth at 100K and 300K was consistent with a random deposition model. In contrast the growth performed at higher substrate temperatures is consistent with significant surface diffusion allowing interlayer mass transport. The growth of Cr on Ag(001) is highly sensitive to the sample temperature. At 100K a poorly defined layer-by-layer growth mode is found and at 300K disordered growth takes place. At higher substrate temperatures coating of adsorbate atoms by substrate atoms describes the data. The growth of Fe on Cu(001) proceeds as layer-by-layer with some atoms sitting in non-epitaxial positions. The lateral order of the Fe islands oscillate in phase with the coverage.

In the case of Fe grown on Cu(001) at room temperature intermixing of the two atomic species takes place up to 4ML. After 6.2ML no intermixing could be detected. A 1.0ML Cr film grown on Ag(001) at 440K consists of an almost complete Ag film on top of an almost complete Cr film. A 2 and 5ML coverage of Cr on Ag(001) grown at 100K had only 50 and 80% of atoms respectively in epitaxial positions. In all of the films studied changes in the spacings of the film was found compared to a model which assumes the pseudomorphic packing of hard sphere radii.

Acknowledgements

I would like to thank Colin Norris for his excellent supervision during the course of my PhD. His constant help and guidance have been invaluable. I also wish to acknowledge the EPSRC for the provision of a studentship.

I would like to thank all my colleagues who are on and have been on the Surface X-ray Diffraction project. Special gratitude is reserved for Chris Nicklin whose experience in the computational, technical and theoretical aspects of the science made him an extremely useful postdoc. I also wish to thank Nigel Jones and Mark James with whom it has been a pleasure to work with. The technical support of Steven Taylor and his advice on the experimental aspects of the science have been extremely helpful.

I also wish to thank Elias Vlieg for his excellent analysis software and to both Martin Lohmeier and Elias Vlieg for the calculations for the six circle diffractometer. The Daresbury Laboratory staff, notably Dr. Tracy Turner, Dr S. Bennett and Gordon Milne are acknowledged for their support.

I would also like to acknowledge all of the members of the surface science group who have made my time as a research student both pleasant and exciting; those not already mentioned are Stuart Thornton, Anthony Keeno, Stuart "Dart" Mozley, Steve Barker and Chris Binns.

I am indebted to my family particularly my parents whose support has helped me throughout my education. I also wish to thank my brother Dave.

Contents

Chapter 1	Introduction	1
Chapter 2	Metallic Thin Films	
2.1	Introduction	3
2.2	The Growth of Metallic Films	3
2.3	Intermixing Segregation and Surface Alloys	4
2.4	Metastability in Epitaxial Magnetic Films	6
2.5	The Correlation between Structure and Magnetism	8
Chapter 3	Theory	
3.1	Introduction	12
3.2	The Fundamental Wave Equation	12
3.3	The Born Approximation	15
3.4	Scattering from the Bulk Crystal	17
3.5	Finite Temperature Effects	19
3.6	Surface X-ray Diffraction	
3.6.1	The Truncated Bulk Crystal	20
3.6.2	Surfaces	22
3.7	The Integrated Intensity	23
Chapter 4	Experimental	
4.1	Introduction	28
4.2	The UHV Chamber	28
4.3	Sample Preparation	29
4.4	Synchrotron Radiation	30
4.5	Beamlines	
4.5.1	Beamline 9.4 at Daresbury Laboratory	31
4.5.2	ID3 at the ESRF	32
4.6	Diffraction	
4.6.1	The Six Circle Diffractometer	32
4.6.2	Crystallographic Alignment	33
4.6.3	Measurement of Crystal Truncation Rods	34

	4.6.4	Choice of Base Vectors	34
4.7		Correction Factors	
	4.7.1	Introduction	35
	4.7.2	In-plane Data	37
	4.7.3	Out-of-plane Data	38
	4.7.4	The Specular Rod	38
	4.7.5	Non-specular Rods	40
	4.7.6	Gamma Circle Correction Factor	41
Chapter 5		The Growth and Structure of Chromium on Copper (001)	
	5.1	Summary	42
	5.2	Background	43
	5.3	Experimental Details	45
	5.4	Results	
	5.4.1	Growth	45
	5.4.2	In-plane Scans	47
	5.4.3	Rod Scans	49
	5.4.4	Rod Scans: The Clean Surface	49
	5.4.5	Rod Scans: Cr on Cu(001)	51
	5.5	Discussion	56
	5.6	Conclusion	59
Chapter 6		The Epitaxial Growth of Chromium on Silver (001)	
	6.1	Summary	60
	6.2	Background	60
	6.3	Experimental Details	62
	6.4	Results	
	6.4.1	Growth	62
	6.4.2	Rod Scans	65
	6.5	Discussion	69
	6.6	Conclusion	72
Chapter 7		The Growth and Structure of Iron on Copper (001)	
	7.1	Summary	74

7.2	Background	74
7.3	Experimental Details	78
7.4	Results	
7.4.1	Growth	78
7.4.2	Relaxation of the Pseudomorphic fct Structure	79
7.4.3	Rod Scans	80
7.4.4	The Stability of the 4ML Structure Grown at 100K	82
7.5	Discussion	82
7.6	Conclusion	83
Chapter 8	Summary and Suggestions for Future Work	
8.1	Introduction	85
8.2	The Growth and Structure of Cr on Cu(001)	85
8.3	The Epitaxial Growth of Cr on Ag(001)	86
8.4	The Growth and Structure of Fe on Cu(001)	88
8.5	Suggestions for Future Work	88
Appendix A	The Simplification of Equation 3.17	91
Appendix B	Evaluation of the Area Element in Terms of the Miller Indices	93
Appendix C	Publications and Reports	95
References		97

Chapter 1

Introduction

The bulk properties of a crystal strongly depend on the position of the atoms in the lattice and the type of atoms making up the structure. It is, therefore, not surprising that the properties of the crystal at the surface, which has a lower symmetry and atomic coordination number, are different from those of the bulk. The formation of a surface is often accompanied by a relaxation, where the layer spacings near the surface differ from those of the bulk, or a reconstruction, in which atoms move parallel to the surface to create a periodicity different to that of the bulk. A thin film of one or two monolayers supported on a substrate will also have properties which can differ substantially to that of the bulk material.

The study of such systems has been made possible by the huge developments in surface science techniques. Remarkable improvements in vacuum systems meant that by 1971 systems could be operated at 10^{-10} Torr (Patrician and Wyman 1971) allowing the study of systems in a clean environment over a period of several hours. Developments in Molecular Beam Epitaxy (MBE) allows the option of growing thin films one layer at a time. Synchrotron radiation offers a highly collimated, highly intense and tuneable beam of radiation. Over the last twenty years there has also been a huge increase in computing power enabling more complex systems to be modelled with the powerful theoretical techniques now available.

The electronic structure of a material depends on the local environment of the atom. An atom in the surface region of a solid will have a lower coordination number than a corresponding atom in the bulk. This will result in a lower orbital overlap and a narrowing of the valence band electron bands. In a magnetic material this can be accompanied by enhanced magnetism.

With a good choice of lattice parameter the growth of metallic thin films offers the opportunity to study the epitaxial growth of metastable phases which are not normally observed at room temperature. Such phases are accompanied by other phenomenon such as novel magnetic phases. With increasing thickness the strain energy associated with the lattice mismatch or the difference in energy

associated with the metastable phase will overcome the energy associated with dislocations and therefore the structure will relax to a lower energy structure.

It is now well known that intermixing of metal adsorbate atoms with those of the substrate forming a surface alloy can take place. This adds to the classical growth modes of Frank-van der Merwe (layer-by-layer), Stranski-Krastanov (initial complete layer growth followed by islanding), Volmer-Weber (Islanding) and simultaneous multilayer.

This thesis is a study of the systems Cr on Cu(001), Cr on Ag(001) and Fe on Cu(001) using the technique of surface X-ray diffraction. Cu and Ag were used as substrate as they are inert and should therefore form a stable interface with another material. In addition to this is the close lattice matching of fcc Fe with Cu(001) and bcc Cr with Ag(001) and the mutual immiscibility both systems. Cr on Cu(001) serves to highlight the difference from the Fe on Cu(001) even though Cr and Fe are structurally very similar. Moreover, both also have very similar high temperature phase fcc structures.

Surface X-ray diffraction is a powerful tool for surface crystallography. The weak scattering of the radiation allows the use of the kinematical approximation where scattering from individual atoms throughout the lattice is simply added. Moreover, the technique has now been extended to the monitoring of growth *in-situ*.

This thesis begins with a summary of metal growth on metal surfaces highlighting existing knowledge; chapter 3 describes the theory of X-ray diffraction, chapter 4 is an overview of the experiment. The growth and structures of Cr on Cu(001), Cr on Ag(001) and Fe on Cu(001) are discussed in chapters 5, 6 and 7 respectively. Finally chapter 8 is a summary chapter with some suggestions for future work.

Chapter 2

Metallic Thin Films

2.1 Introduction

The work contained in this thesis concerns the transition metals, Cr and Fe deposited on the (001) surfaces of the noble metals Cu and Ag. Such systems are interesting since the 3d metals exist in a variety of crystallographic and magnetic phases and it is thought that with careful lattice matching well ordered layers can be grown. Since noble metals are relatively inert a stable sharp interface should result. If this can be achieved then the magnetic properties of ultrathin layers which are strained and are possibly metastable phases, can be studied and compared to their respective bulk properties. It is possible to model such systems with the powerful theoretical techniques available. This chapter begins with a discussion on growth introducing the classical picture. Following this more complex growth modes are considered with some results from experiments. Also discussed is the epitaxial growth of high temperature phases of materials on suitable substrates at room temperature. The rest of the chapter examines the magnetic theory of surfaces and interfaces and the link between magnetism and structure.

2.2 The Growth of Metallic Films

The growth of a material on a substrate is usually classified as one of three modes: Frank-van der Merwe (or layer-by-layer), Stranski-Krastanov, where there is initial layer-by-layer growth followed by islanding and Volmer-Weber where three dimensional islands form on the surface. Bauer (1958) introduced a parameter Δ such that $\Delta = \gamma_f + \gamma_{in} - \gamma_s$ where γ_f is the surface free energy of the film, γ_{in} is the energy associated with the interface between the adsorbate film and the substrate surface and γ_s is the surface free energy of the substrate. Volmer-Weber growth would, therefore, be satisfied if $\Delta > 0$ and either Stranski-Krastanov

or Frank-van der Merwe would be satisfied if $\Delta \leq 0$. Moreover, for Frank-van der Merwe growth this condition must be fulfilled for each layer. For this to occur $\gamma_f \approx \gamma_s$ and $\gamma_{in} \approx 0$, that is, the substrate and the film are very similar and this condition can only be rigorously fulfilled for homoepitaxial growth where $\gamma_f = \gamma_s$ and $\gamma_{in} = 0$. In a practical situation a system which does grow layer-by-layer will eventually get to a certain thickness and start islanding so that Stranski-Krastanov growth will prevail. In practice it is difficult to predict the growth mode from the above considerations. To begin with using bulk values of the surface free energy for thin films is a poor approximation to the real case. For instance in a thin film the electronic structure will differ from the bulk, due to the different physical environment, and could be modified significantly by interaction with the substrate. In addition to this the interface energy between two lattices is not well known. Another problem is that in the above we have treated the growth as an equilibrium process. In reality the diffusion of adatoms on a substrate surface is so small that the equilibrium configuration is not achieved.

2.3 Intermixing, Segregation and Surface Alloys

When a metal film is grown one may expect one of the three classic growth modes mentioned above. It is often desirable to have a layer-by-layer mode as the electronic states can be modelled theoretically. Recent interest in magnetism has provoked the study of magnetic metal overlayers supported on a noble metal substrate. The noble metal substrate is desirable due to its inert nature. The problem with this, however, is that in many cases $\gamma_f > \gamma_s$ and energy considerations favour Volmer-Weber growth. This is because islanding will minimise some of the surface free energy by keeping some of the substrate uncovered.

The above picture is somewhat simplified and other growth modes have been found to be favourable to islanding.

An interesting growth mode has been reported for Rh on Ag(001) (Smitz *et al* 1989). Here the surface free energy of Rh (2.83J/m²) is more than twice that of Ag (1.30J/m²) so that islanding would be expected. The growth, however,

proceeds so that a Ag/Rh/Ag(001) sandwich is produced at a monolayer of Ag. The mobility of the Ag atoms at the surface is sufficient to allow diffusion onto the adsorbate structure. This will result in a lowering of the surface free energy. This mode is represented in figure 2.1.

Fe deposited on Au(001) is also found to naturally form a Au/Fe/Au(001) sandwich structure (Bader *et al* 1987). By monitoring their Auger signal they found that after depositing some Fe, the Au Auger signal stays constant indicating that a certain amount of Au has segregated from the bulk on to the top of the Fe overlayer. The Au signal was found to correspond to a monolayer.

Intermixing is another departure from the three classical growth models. Since Au and Ni are immiscible in the bulk it would be thought that Au would grow on Ni such that a sharp interface would result. Au on Ni(110), however, (Pleth Nielson *et al* 1993) has been found to grow in an unusual manner. Au atoms replace Ni atoms in the surface region only. The Ni atoms which are squeezed out agglomerate into islands on the surface. Even though the atoms do not mix in the bulk the surface region is still susceptible to alloying. This effect serves to highlight the contrasting nature of the physics of the surface and the bulk region of the solid. Such an effect may be explained by the electron density surrounding the Au atoms. In the Ni(110) surface a Au atom experiences the electron density from 8 Ni atoms as opposed to 12 if it was situated in the bulk Ni environment. Since the Ni atoms are closer together than the Au atoms in bulk Au the electron density felt by a Au atom in the surface region of the Ni substrate is closer to that experienced by a Au atom in a Au lattice than a Au atom situated in the Ni bulk. Figure 2.1 shows a schematic of this growth mode.

Mn on Cu(001) forms many different structures depending on the temperature of the substrate during deposition and the coverage. If 0.5 monolayers of Mn is deposited at a substrate temperature of 270K, an ordered c(2x2) surface alloy has been found to exist (Wuttig *et al* 1993, Flores *et al* 1992). A representation of this structure is shown in figure 2.2. Two similar alloy systems are Cu(100)c(2x2)Au (Wang *et al* 1987) and Cu(100)c(2x2)Pd (Wu *et al* 1988). The Cu(100)c(2x2)Mn system is unusual due to the large outwards relaxation of the Mn atoms of $0.30 \pm 0.02 \text{ \AA}$ compared to 0.1 \AA for Au and 0.03 \AA for Pd. From an argument based purely on the bulk hard sphere radius Mn should relax less than Pd and Au. This effect has been explained in terms of a magnetic stabilisation.

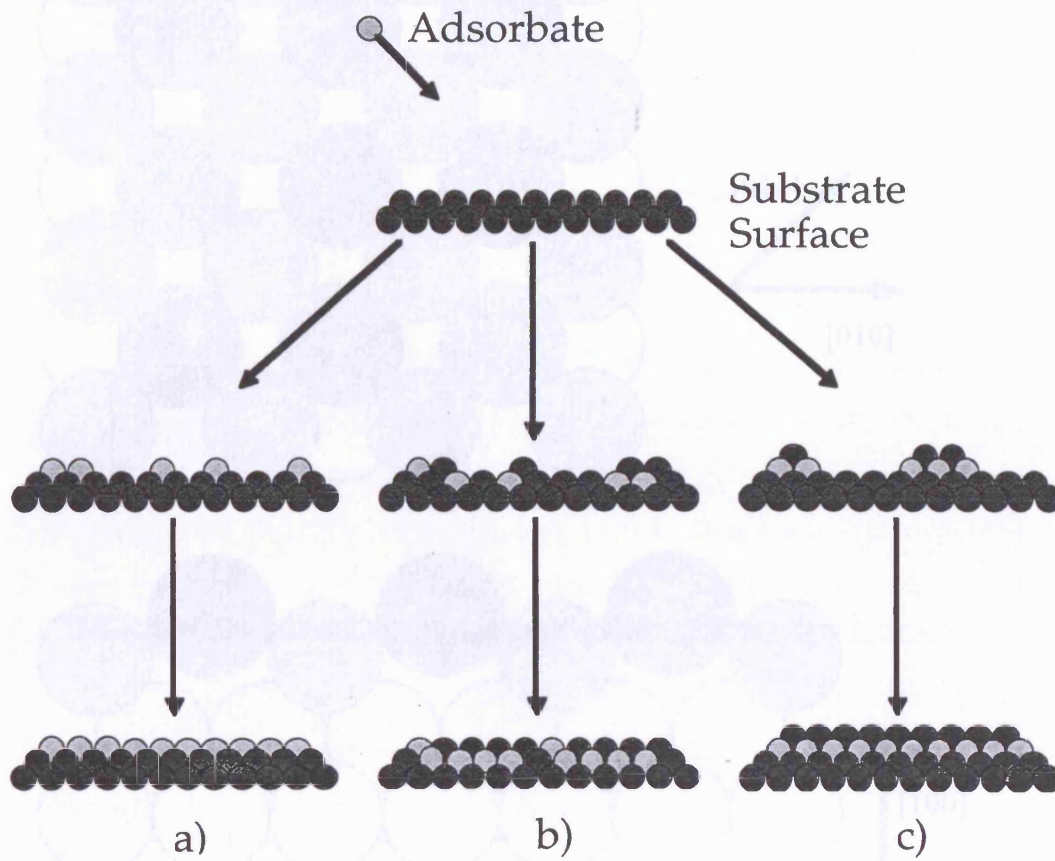
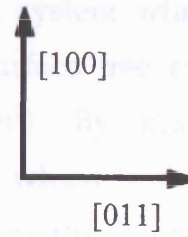
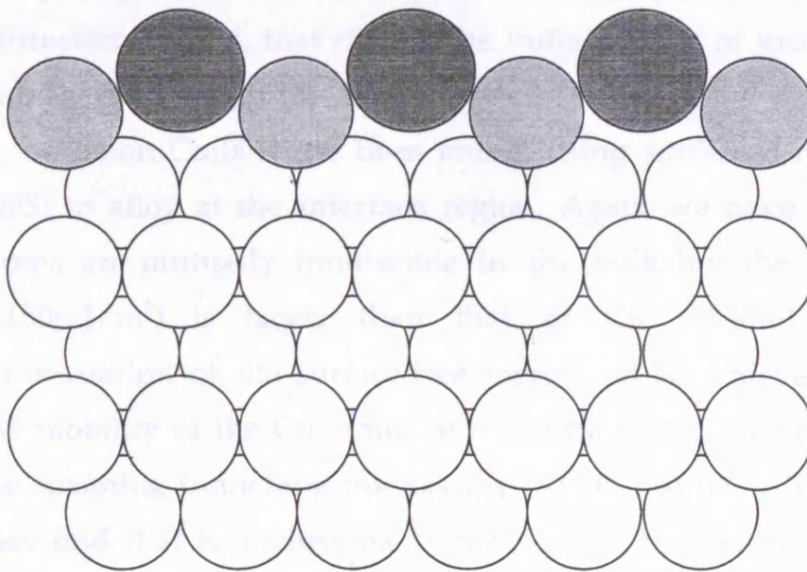
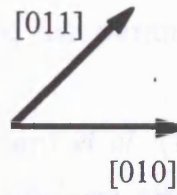
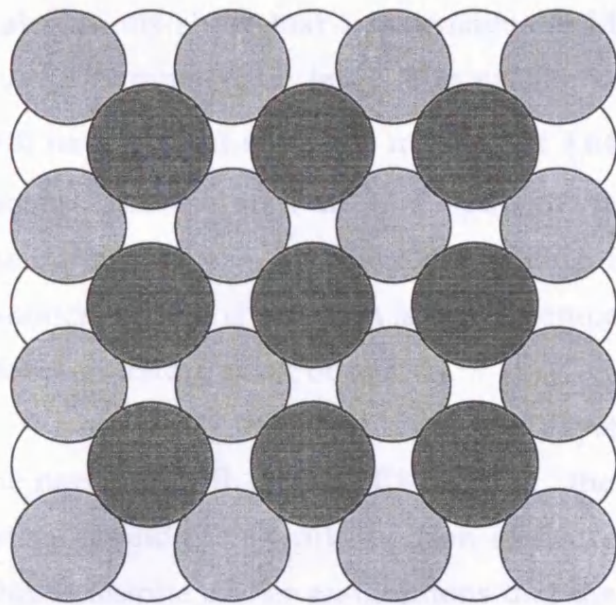


Figure 2.1. Three models for growth up to a monolayer equivalent. The classical Frank-van der Merwe or layer-by-layer growth is shown in a). Intermixing is shown in b) and coating of the deposited film by substrate atoms is shown in c).



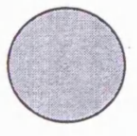
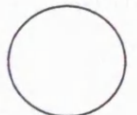
-  Mn atoms (surface layer)
-  Cu atoms (surface layer)
-  Cu atoms (substrate)

Figure 2.2. In-plane and out-of-plane structure of $\text{Cu}(100)c(2 \times 2)\text{-Mn}$.

Calculations show that a ferromagnetic MnCu layer is energetically more stable than a paramagnetic layer. The calculations show that a ferromagnetic system will have a giant magnetic moment of $3.64\mu_B$ per Mn atom. Such a large moment means that the spin up and spin down bands are almost entirely separated meaning that the numbers of bonding and antibonding electrons are almost identical so that d cohesion is small compared to the paramagnetic case. The Mn atoms therefore relax outwards.

In a study of the Cr on Au(001) system Hanf *et al* (1989) have interpreted the narrow width of their Cr 3d peak, the non-uniform attenuation of the Au 5d intensity and their work function measurements in terms of an interfacial alloy. This is despite earlier assumptions that the interface between the two materials is sharp (Zajac *et al* 1985). Rouyer *et al* (1993) also find, from their photoelectron diffraction results, that during the initial stages of growth Cr incorporates itself into fcc sites within the Au substrate.

Fe on Cu(001) has been found, using surface X-ray diffraction, (James *et al* 1995) to alloy at the interface region. Again we have a system where the two atoms are mutually immiscible in the bulk but the surface free energy of Fe ($2150\text{mJ}/\text{m}^2$) is larger than that of Cu ($1850\text{mJ}/\text{m}^2$). By intermixing a minimisation of the surface free energy can be achieved which is allowed for by the mobility of the Cu atoms at the surface. This supports the interpretation of the scanning tunnelling microscopy (STM) results of Johnson *et al* (1993) where they find that Fe inclusions in the Cu substrate surface initiate growth. After a coverage of 2.8ML the growth proceeds by layer-by-layer. Earlier results by Steigerwald *et al* (1987, 1988) also suggest that intermixing takes place.

2.4 Metastability in Epitaxial Magnetic Films.

A careful choice of a substrate with a suitable lattice parameter makes possible the growth of high temperature phases at room temperature.

Bulk Fe can exist in several phases depending on the temperature and pressure. Figure 2.3 shows a thermodynamic phase diagram of Fe (after Takahashi and Basset 1964). The well known ferromagnetic bcc α phase of Fe exists up to 910°C . An antiferromagnetic fcc γ phase then exists up to 1390°C . This

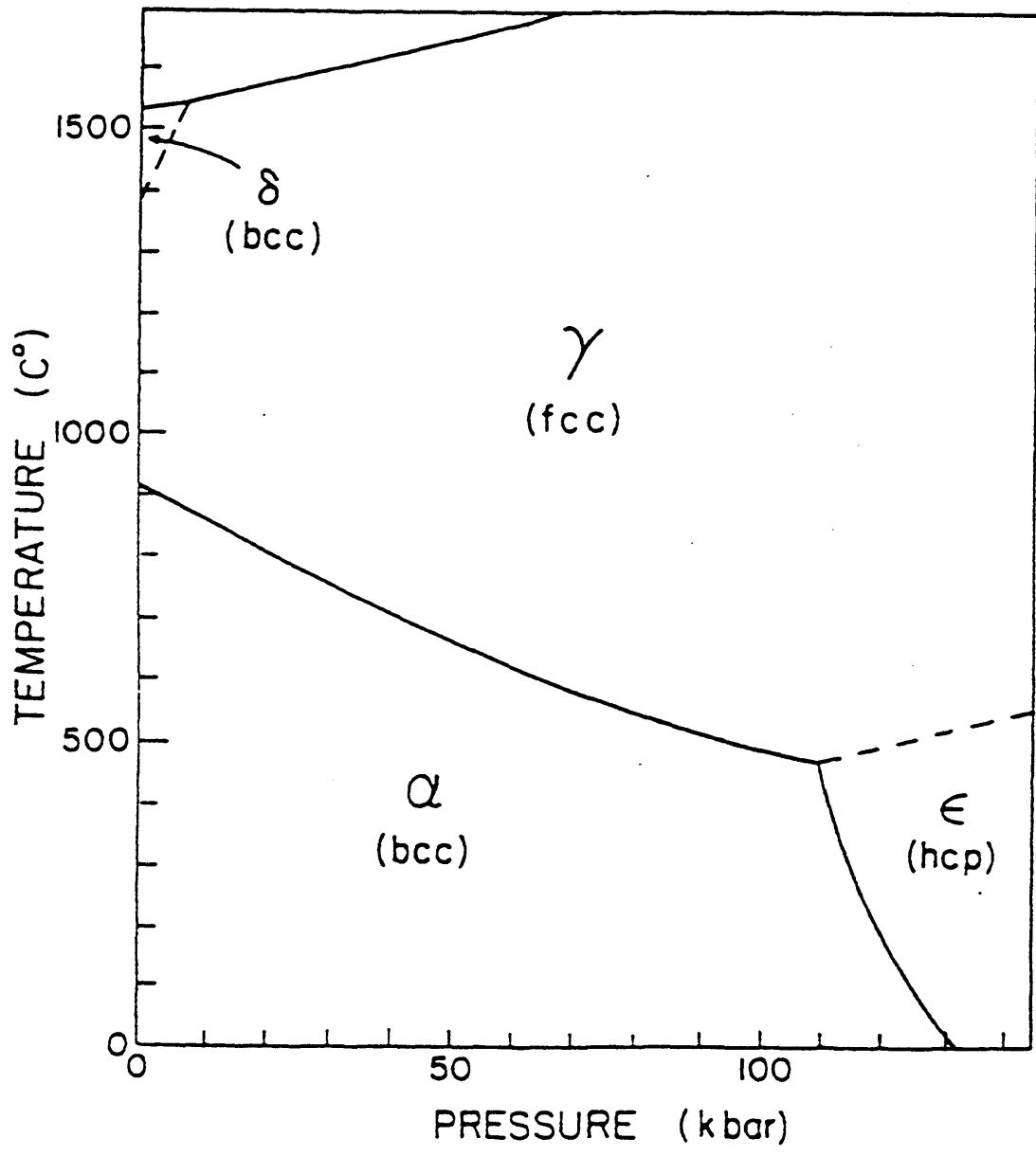


Figure 2.3. The thermodynamic phase diagram of Fe (Takahashi and Basset 1964).

is then followed by a non-magnetic bcc δ phase. In addition to this at high temperatures a non-magnetic hcp ϵ phase can be induced at high pressures.

If we can find a substrate with a suitable lattice parameter it would be expected that one of the high temperature phases could be supported at room temperature. The phase diagram in figure 2.3 concerns a bulk material which is subject to a hydrostatic pressure. On a substrate surface a film would only have a pressure exerted at the interface. The film would therefore be free to undergo a distortion perpendicular to the surface so that the energy could be minimised by maintaining the volume of the bulk unit cell. The resulting thin film structure does not necessarily have to lie in a global minimum of total energy but could lie in a higher local minimum i.e. it may be a metastable state.

The thickness that a uniaxially distorted film can grow to depends on the relative values of the energy associated with the bonding at the interface, the energy associated with strain relieving defects and the energy linked to the tetragonal uniaxial distortion. The value of the uniaxial distortion energy increases with the thickness of the film and when its value exceeds that of the other two energy contributions the structure of the film will relax to its bulk value. Even if we find a metastable film which is perfectly matched with the lattice of the supporting substrate the accumulation of the energy associated with the higher energy metastable structure with film thickness will surmount the energy needed to introduce defects or break bonds at the interface. The system will therefore relax to the lower energy structure of the material after a certain thickness.

Extrapolating the high temperature fcc Fe lattice constant down to room temperature yields a value of 3.59\AA . This is very close to the lattice constant of Cu which has a value of 3.61\AA . It would therefore be expected that the fcc γ Fe phase can be supported on the Cu(001) surface. There is also only a very small energy difference between the bcc α Fe and fcc γ Fe phases which is probably much smaller than the strain energy required to grow the bcc phase on Cu(001).

Shown in figure 2.4 is the calculated total energy of the fcc Fe as a function of the lattice parameter a_0 (after Moruzzi *et al* 1989). At the lattice parameter of Cu ($a_0=3.61\text{\AA}$) three different phases coincide with each other. This is a possible explanation for disagreement between experiments. The existence of a

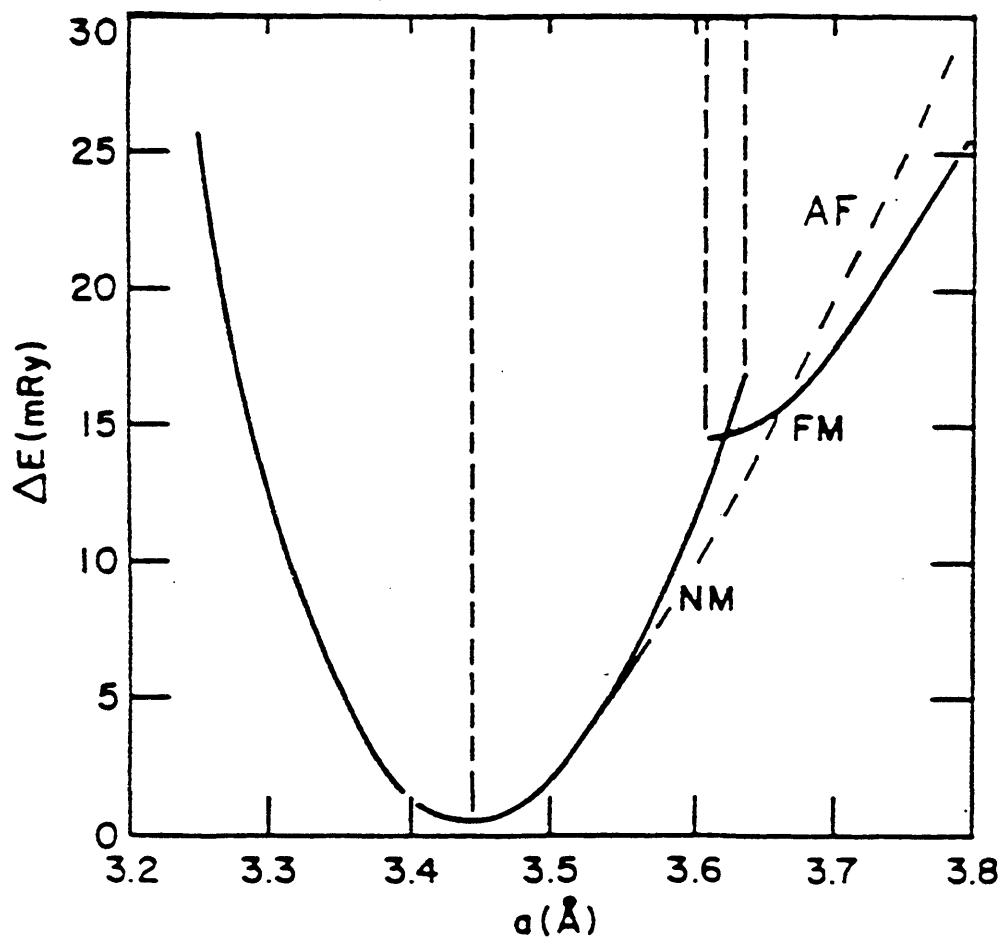


Figure 2.4. Calculated binding energy curves for fcc γ Fe versus the cubic lattice constant. Energy changes are in units of mRy per atom and are referenced to the minimum (Moruzzi et al 1989).

ferromagnetic fcc phase in some experiments is surprising since no known high temperature equivalent exists.

2.5 The Correlation between Structure and Magnetism.

In supported thin magnetic films a modification of the structural and magnetic properties is often found especially when the overlayer consists of a material that is weakly magnetic in its bulk form (Wuttig *et al* 1995). Similar modifications are found at the surfaces of magnetic materials indicating that the lower coordination number and lower symmetry are responsible.

The electronic structure of a ferromagnetic and a paramagnetic solid with a half filled d band are shown in figure 2.5. In the magnetic case the spin up and spin down electronic bands do not overlap. This is of course a simplification of the actual situation where the bands will overlap. In the paramagnetic case both the spin up and spin down bands are equally occupied. However, the antibonding states are totally empty. In the magnetic case the spin up band is completely occupied whilst the spin down band is totally empty. The complete separation of the spin up and spin down bands now means that the bonding and antibonding states are equally occupied. As a result of this the cohesive force between atoms is stronger for the non-magnetic case than it is for the magnetic case. The lattice spacing in the latter will therefore be larger. This is a simple case which demonstrates that magnetism can play an important role in the spacing between atoms.

The real case is quite different to the above. Figure 2.6 shows a more realistic picture of the electronic states of a collection of atoms in the bulk and in the surface region of a solid that is ferromagnetic. The spin up and spin down bands now overlap slightly. It can now be seen that if the solid is a weak magnet rather than a strong one then strong modifications of the population of the spin up and spin down bands is possible. A move from the bulk environment to the surface region of a solid is accompanied by a reduction in coordination number. The bands will therefore become smaller i.e. there is a narrowing of the density of states. This narrowing could in turn modify the relative populations of the bonding and antibonding states which would influence changes in the interatomic spacings.

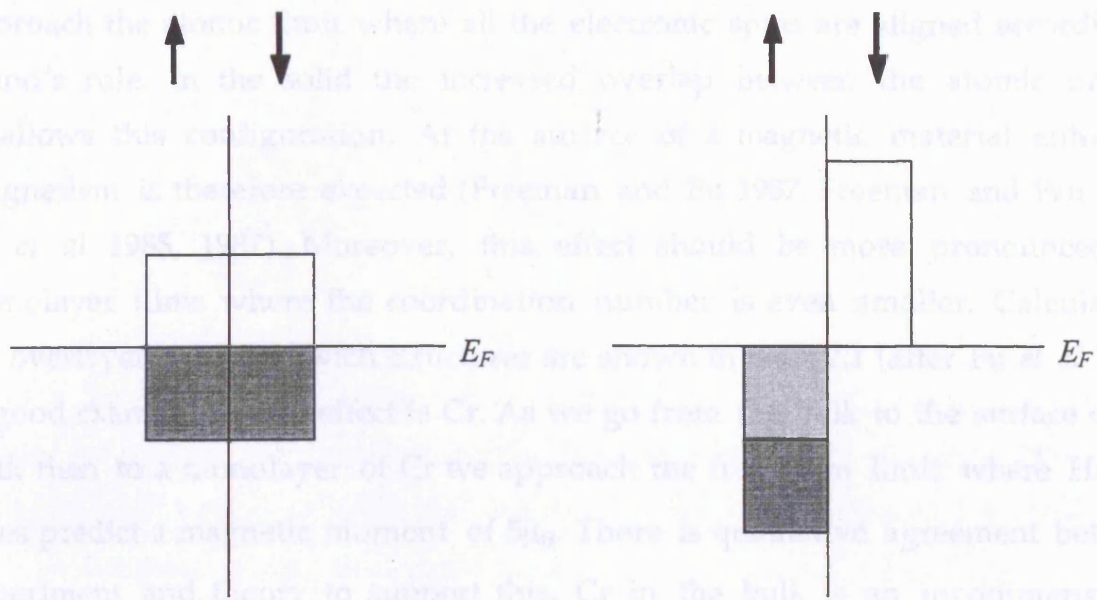


Figure 2.5. Schematic of the d -bands for the spin up and spin down electrons for a paramagnetic and a ferromagnetic solid. The lighter (darker) shaded area represent antibonding (bonding) states. E_F denotes the Fermi energy.

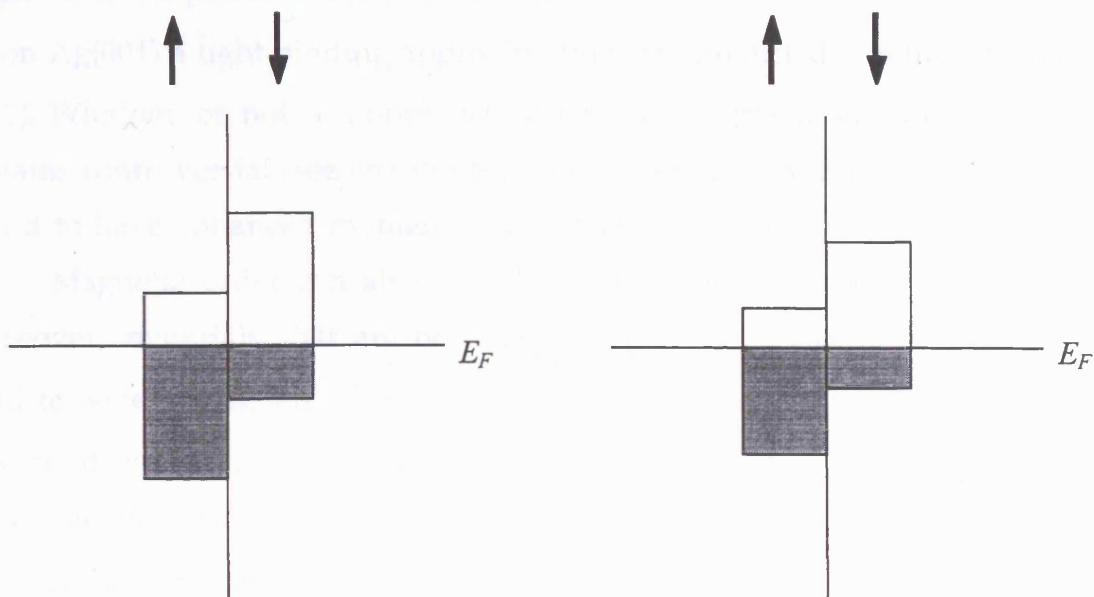


Figure 2.6. Comparison of the d bands for electrons in a ferromagnetic solid and a ferromagnetic surface.

The change in environment can also lead to changes in the magnetism itself. As transition metals become more diluted their magnetic moments approach the atomic limit where all the electronic spins are aligned according to Hund's rule. In the solid the increased overlap between the atomic orbitals disallows this configuration. At the surface of a magnetic material enhanced magnetism is therefore expected (Freeman and Fu 1987, Freeman and Wu 1991, Fu *et al* 1985, 1987). Moreover, this effect should be more pronounced for monolayer films where the coordination number is even smaller. Calculations for overlayers and sandwich structures are shown in table 2.1 (after Fu *et al* 1985). A good example of this effect is Cr. As we go from the bulk to the surface of the bulk then to a monolayer of Cr we approach the free atom limit where Hund's rules predict a magnetic moment of $5\mu_B$. There is qualitative agreement between experiment and theory to support this. Cr in the bulk is an incommensurate antiferromagnetic spin wave with a magnetic moment per atom of $0.45\mu_B$ (Bacon 1961). However, theoretical calculations of the (001) surface have predicted moments of $2.8\mu_B$ (Alan 1978, 1979), $2.6\mu_B$ (Gempel 1981), $3\mu_B$ (Victoria and Falicov 1985, Klebanoff *et al* 1985). This compares to values of $2.4\mu_B$ found from angle-resolved photoemission results (Klebanoff *et al* 1984). For a monolayer of Cr on Ag(001) a tight binding approximation has predicted a value of $3.6\mu_B$ (Alan 1991). Whether or not a monolayer of Cr can be grown supported on Ag (001) remains controversial (see chapter 6 of this thesis) but overlayers of Cr have been found to have enhanced moments (Newstead 1987, Johnson 1988).

Magnetic order can also be enhanced at the surfaces of magnetic solids. Moreover, materials that are non-magnetic can have magnetic surfaces. For a solid to be ferromagnetic the Stoner criterion $U\rho(E_F) > 1$ must be satisfied. When this condition is satisfied one spin population dominates another and the paramagnetic system becomes unstable towards ferromagnetism. The density of states at the Fermi energy $\rho(E_F)$ will vary with lattice spacing (Moruzzi *et al* 1988). If we imagine a situation where we can vary the atomic separation of a primarily paramagnetic material as the lattice spacing becomes larger, and the electronic bands narrow, $\rho(E_F)$ increases. Eventually the Stoner criterion will be satisfied so that ferromagnetism sets in. Changes in symmetry and coordination number also

effect $\rho(E_F)$. Calculations for Cr(001) (G. Allan 1979), Mo(001) (Kerker *et al* 1978) and W(001) (Posternak *et al* 1980) show how $\rho(E_F)$ at the surface can differ substantially from the bulk value. Since the bands narrow at the surface the local density of states at the Fermi energy will increase and ferromagnetism is then a possibility. For W(001) and Mo(001) it is believed that the surface states at E_F drive the observed surface reconstructions. The mechanism involves the forming of a charge density wave. In response to the charge density wave the lattice spontaneously distorts. The corresponding redistribution of the electron density is such that the Fermi energy, E_F , resides in a minimum between two local maximum in the local density of states (Posternak *et al* 1980, Tosatti 1978). Such a structure will be energetically favourable because the energies of occupied states will be lowered whilst unoccupied states will be raised. The Cr(001) surface, however, has no observed reconstruction and there is now evidence that there is a ferromagnetic surface layer which has an enhanced ordering temperature relative to the bulk Néel temperature (Klebanoff *et al* 1984, 1985) which is supported by theoretical calculations (Gempel 1981).

The above results have also been applied to 4d and 5d metals which are normally not magnetic in the bulk. Theoretical work has predicted that a Rh monolayer on Au (001) is a ferromagnetic layer with an enhanced moment (Ming *et al* 1991). Blugel (1992) has predicted magnetism in some 4d and 5d metals.

	Cr		E(para.)-E(spin-pol.)
Cr monolayer	4.12	...	1.69
1 Cr/Au(001)	3.70	0.14	0.78
2 Cr/Au(001)	2.90 (S)	-0.08	0.60
	-2.30 (S-1)		
Au/Cr/Au(001)	3.10	0.14 (S)	0.38
		0.13 (S-2)	
(1x1)Au/Cr CMS	2.95	0.10	0.25
Fe monolayer	3.20	...	1.34
1Fe/Cu(001)	2.85	0.04	0.70
1Fe/Ag(001)	2.96	0	1.14
2Fe/Ag(001)	2.94 (S-1)	0.05	1.15
	2.63 (S-1)		
Ag/Fe/Ag	2.80	0	0.88
Au/Fe/Au	2.92	0.08	0.97
1V/Au(001)	1.75	0.04	0.10
1V/Ag(001)	1.98	0.06	0.14
2V/Ag(001)	1.15 (S)	0	0
	<0.05 (S-1)		
Ag/V/Ag	0	0	...
Cr/Fe/Au(001)	3.10 (Cr)	-0.04	-0.04
	-1.96 (Fe)		
Fe/Cr/Ag(001)	2.30 (Fe)	-0.09	-0.09
	-2.40 (Cr)		

Table 2.1. Calculations of magnetic moments (in μ_B). S and S-1 indicate surface and subsurface layers. The Third column is the moment transferred to the substrate. The fourth column is the spin-polarisation energy (from Fu et al 1985).

Chapter 3

Theory

3.1 Introduction

In this chapter an outline of the theory of surface X-ray diffraction is presented. The wave equation describing the scattering process is solved using the single scattering or Born approximation which leads to the kinematical theory for X-ray diffraction. In this way it is seen that X-ray diffraction measures the Fourier transform of the electron density. This result is then applied to calculate an expression describing the scattering from an infinite single crystal. By truncating the crystal a two dimensional flat surface is formed and the modification of the scattering is deduced. Finally, the expression for the intensity is used to derive the integrated intensity, the quantity that is actually measured in experiment. More complete accounts of the theory are presented in the literature (Cowley 1984, Warren 1969, Robinson and Tweet 1992, Feidenhans'1 1989).

3.2 The Fundamental Wave Equation

When an X-ray beam illuminates a crystal the oscillatory electric field is absorbed by the electrons. Since these electrons are being accelerated they will in turn emit radiation, that is they will produce a scattered beam. In the crystal the displacement field \mathbf{D} is given by

$$\mathbf{D} = \epsilon_0 \mathbf{E} + \mathbf{P} = \epsilon_0 \epsilon_r \mathbf{E} \quad (3.1)$$

where \mathbf{E} is the electric field of the incident X-ray beam, \mathbf{P} and ϵ_r are the polarisation and relative permittivity of the medium respectively and ϵ_0 is the permittivity of free space. Using the Maxwell equations and the relations

$$\begin{aligned}\mathbf{D} &= \epsilon_0 \epsilon_r \mathbf{E} \\ \mathbf{B} &= \mu_0 \mu_r \mathbf{H}\end{aligned}\tag{3.2}$$

where \mathbf{B} is the magnetic flux density, \mathbf{H} is the magnetic field strength, μ_r is the relative permeability of the medium and μ_0 is the permeability of free space, we obtain the equation of a wave travelling through the medium

$$\nabla^2 \mathbf{E}(\mathbf{r}, t) = \epsilon_0 \epsilon_r \mu_0 \mu_r \frac{\partial^2}{\partial t^2} \mathbf{E}(\mathbf{r}, t)\tag{3.3}$$

Since the speed of light in a vacuum c is given by

$$c = \frac{1}{\sqrt{\epsilon_0 \mu_0}}\tag{3.4}$$

equation (3.3) can be rewritten as

$$\nabla^2 \mathbf{E}(\mathbf{r}, t) = \frac{\epsilon_r \mu_r}{c^2} \frac{\partial^2}{\partial t^2} \mathbf{E}(\mathbf{r}, t)\tag{3.5}$$

This is the equation describing the X-ray beam inside the crystal. It has the general form of the wave equation with the speed of the waves given by $c/\sqrt{\epsilon_r \mu_r}$. A similar equation could be derived for \mathbf{H} but the interaction of the magnetic part of the wave with the magnetic properties of the electrons is so small we will ignore it (Bruckel *et al* 1993, Blume 1985).

From now on \mathbf{E} will be treated as a scalar quantity and we allow for this by multiplying the final result by a polarisation factor. To further the analysis, only a single frequency ω will be used. This is justified since before analysis the inelastic background is subtracted from the data. Using this result and splitting up the time and space dependence of the electric field we obtain

$$E(\mathbf{r}, t) = E(\mathbf{r})e^{-i\omega t}\tag{3.6}$$

If we now substitute equation (3.6) into (3.5) and use the relation $k^2 = \epsilon_r \mu_r \omega^2 / c^2$, where k is the wave number of the X-ray radiation inside the material, we get

$$[\nabla^2 + k^2]E(\mathbf{r}) = 0 \quad (3.7)$$

This is a simplified version of equation (3.5) without the time dependence of the wave amplitude. The next step is to find an expression for the wave number in terms of the electron density of the system which the wave has entered.

We now need to consider the polarisation of a collection of charges. For a system with an electron density $\rho(\mathbf{r})$ where each electron has a dipole moment $-ex$, the polarisation (i.e. the dipole moment per unit volume) is

$$P = -e\rho(\mathbf{r})x \quad (3.8)$$

x , the electron displacement during absorption of the X-ray, is obtained using the equation of motion of the electron in the electric field E .

$$m \frac{\partial^2 x}{\partial t^2} = -eEe^{-i\omega t} \quad (3.9)$$

m being the electronic mass. Assuming that the electron vibrates with the same frequency as the impinging wave we get

$$x = \frac{eE}{m\omega^2} e^{-i\omega t} \quad (3.10)$$

Substituting equation (3.10) into (3.8) yields

$$P = -\frac{e^2 \rho(\mathbf{r})}{m\omega^2} Ee^{-i\omega t} \quad (3.11)$$

so that equation (3.1) can be rewritten by using this expression for the polarisation which will then give an equation for the relative permittivity

$$\epsilon_r = 1 - \frac{e^2 \rho(\mathbf{r})}{\epsilon_0 m \omega^2} \quad (3.12)$$

This equation gives us the variation of ϵ_r with the electron density. The X-ray radiation has a wavelength comparable to the spacing of atoms in a crystal lattice so we can no longer assume that the permittivity is a constant for a given material. The permittivity will vary with \mathbf{r} . This sensitivity to the electron density is what makes X-ray diffraction so useful in deducing the arrangement of the atoms in a material.

Putting equation (3.12) into (3.7) reveals

$$\left[\nabla^2 + k_0^2 - 4\pi r_e \rho(\mathbf{r}) \right] E(\mathbf{r}) = 0 \quad (3.13)$$

where $k_0 = \omega/c = 2\pi/\lambda$, the wave number of the incident X-ray beam, and $r_e = e^2/4\pi\epsilon_0 mc^2$ the classical electron radius. This is the fundamental equation that we need to solve for the crystal in order to obtain the diffracted intensities.

3.3 The Born Approximation

The solution to the equation 3.13 is

$$E(\mathbf{r}) = E_i(\mathbf{r}) - 4\pi r_e \int G(\mathbf{r}, \mathbf{r}') \rho(\mathbf{r}') E(\mathbf{r}') d\mathbf{r}' \quad (3.14)$$

where $E_i(\mathbf{r})$ is the electric field of the incoming beam and thus the solution of $[\nabla^2 + k_0^2]E(\mathbf{r}) = 0$ and the last term is the particular integral containing a suitable Green's function $G(\mathbf{r}, \mathbf{r}')$. The appropriate form of the Green's function is

$$G(\mathbf{r}, \mathbf{r}') = \frac{e^{-ik|\mathbf{r}-\mathbf{r}'|}}{4\pi|\mathbf{r}-\mathbf{r}'|} \quad (3.15)$$

where k is the wave number of the scattered beam.

The incident wave is a plane wave

$$E_i(\mathbf{r}) = E_0 e^{-i\mathbf{k}_i \cdot \mathbf{r}} \quad (3.16)$$

The form of the scattered part of the wave is difficult to solve because we need to know the solution before we can calculate the integral. It is found by a successive approximation procedure. The incident wave solution (the zeroth order solution) is put into the integral and then solved giving the first order solution. In principle this method can now be iterated i.e. we put the first order solution into the equation to get a second order solution etc. If we make use of the fact that X-rays are only scattered by matter very weakly then we can justify only taking the series to first order. This is known as the first Born approximation. What we are essentially doing is assuming that X-rays are only scattered once which is why the approximation is also known as the single scattering approximation. By taking higher order terms out of the Born approximation we are neglecting the higher order effects that arise from multiple scattering. This method is known as the kinematical theory for X-ray diffraction. By substituting equations (3.15) and (3.16) into the general solution (3.14) we get the result

$$E_i(\mathbf{r}) + E_s(\mathbf{r}) = E_0 e^{-i\mathbf{k}_i \cdot \mathbf{r}} - r_e E_0 \int \frac{e^{-ik|\mathbf{r}-\mathbf{r}'|}}{|\mathbf{r}-\mathbf{r}'|} \rho(\mathbf{r}') e^{-i\mathbf{k}_i \cdot \mathbf{r}'} d\mathbf{r}' \quad (3.17)$$

In an experiment the point of observation will be at a distance large compared with the dimensions of the sample. We can approximate the Green's function exponential so that the scattered part of the wave can be expressed as (see appendix A)

$$E_s(\mathbf{r}) = -r_e E_0 \frac{e^{-i\mathbf{k}_f \cdot \mathbf{r}}}{r} \int e^{i\mathbf{q} \cdot \mathbf{r}'} \rho(\mathbf{r}') d\mathbf{r}' \quad (3.18)$$

where $\mathbf{q} = \mathbf{k}_f - \mathbf{k}_i$ the momentum transfer vector, and \mathbf{k}_i and \mathbf{k}_f are the incident and scattered wave vectors.

Equation (3.18) describes what happens when an incoming X-ray beam is scattered by a collection of charges. Thus the Born approximation allows us to

express the scattering from a distribution of charge as the sum of the scattering from the individual elements. The integral is just the Fourier transform of the electron density. The term before the integral describes the scattering from a single electron, the Thompson expression. Since the value of r_e has an extremely small value of $3 \times 10^{-15} \text{m}$ the scattering from a single electron is indeed very weak. Even when the integral is evaluated for the large number of electrons in a crystal the total scattering cross section is still quite small. The $1/r$ dependence in equation (3.18) arises from the fact that a plane wave is incident on the electrons whilst a spherical wave is emitted.

3.4 Scattering from the Bulk Crystal

For a crystal made up of regularly repeating unit cells defined by the base vectors \mathbf{a}_1 , \mathbf{a}_2 and \mathbf{a}_3 equation 3.18 becomes

$$E_s = -r_e E_0 \frac{e^{-ikr}}{r} \int_{\text{unitcell}} \rho(\mathbf{r}) e^{i\mathbf{q}\cdot\mathbf{r}} d\mathbf{r} \sum_{n_1=0}^{N_1-1} \sum_{n_2=0}^{N_2-1} \sum_{n_3=0}^{N_3-1} e^{i\mathbf{q}\cdot(n_1\mathbf{a}_1+n_2\mathbf{a}_2+n_3\mathbf{a}_3)} \quad (3.19)$$

where N_i is the number of unit cells along the direction parallel to the vector \mathbf{a}_i . The integral over the unit cell is the structure factor $F(\mathbf{q})$

$$F(\mathbf{q}) = \int_{\text{unitcell}} \rho(\mathbf{r}) e^{i\mathbf{q}\cdot\mathbf{r}} d\mathbf{r} \quad (3.20)$$

which can alternatively and conveniently be expressed as a sum over the contribution from the individual atoms within the cell.

$$F(\mathbf{q}) = \sum_{j=1}^{N_c} f_j(\mathbf{q}) e^{i\mathbf{q}\cdot\mathbf{r}_j} \quad (3.21)$$

where $f_j(\mathbf{q})$ is the atomic form factor for atom j .

$$f(\mathbf{q}) = \int_{-\infty}^{+\infty} \rho(\mathbf{r}') e^{i\mathbf{q}\cdot\mathbf{r}'} d\mathbf{r}' \quad (3.22)$$

This is the Fourier transform of the electron density for the single atom. It is only written as the magnitude of the momentum transfer vector, independent of direction, because in most cases the atom is spherically symmetric. We have assumed, in the above expression, that the electrons are free which is a simplification of the real situation where the electrons are bound. If the X-rays are absorbed, or the X-ray is near a resonant frequency i.e. it excites electronic transitions, the polarisation is no longer described by equation (3.11). These problems are overcome by forming atomic scattering factors that are complex and wavelength dependent i.e.

$$f = f_0 + \Delta f' + i\Delta f'' \quad (3.23)$$

The term f_0 is constant whilst $\Delta f'$ and $\Delta f''$ are wavelength dependent dispersion corrections.

In an experiment we measure the intensity which is the square of the modulus of the above:

$$I_s = I_0 \left(\frac{r_e}{r} \right)^2 F(\mathbf{q})F(\mathbf{q})^* \sum_{n_1=0}^{N_1-1} \sum_{n_2=0}^{N_2-1} \sum_{n_3=0}^{N_3-1} e^{i\mathbf{q} \cdot (n_1 \mathbf{a}_1 + n_2 \mathbf{a}_2 + n_3 \mathbf{a}_3)} \sum_{n_1=0}^{N_1-1} \sum_{n_2=0}^{N_2-1} \sum_{n_3=0}^{N_3-1} e^{-i\mathbf{q} \cdot (n_1 \mathbf{a}_1 + n_2 \mathbf{a}_2 + n_3 \mathbf{a}_3)} \quad (3.24)$$

Where $I_0 = E_0 E_0^*$ is the intensity of the incident beam. Each summation is a simple geometric sum and can be evaluated

$$\sum_{n=0}^{N-1} e^{i\mathbf{q} \cdot n\mathbf{a}} = \frac{1 - e^{i\mathbf{q} \cdot N\mathbf{a}}}{1 - e^{i\mathbf{q} \cdot \mathbf{a}}} \quad (3.25)$$

Equation (3.25) will contain the square modulus of the above result which will be

$$\left| \sum_{n=0}^{N-1} e^{i\mathbf{q} \cdot n\mathbf{a}} \right|^2 = \frac{\sin^2(N\mathbf{q} \cdot \mathbf{a}/2)}{\sin^2(\mathbf{q} \cdot \mathbf{a}/2)} \quad (3.26)$$

In the limit of large N this will give us a series of delta functions that occur when the condition $\mathbf{q} \cdot \mathbf{a} = 2\pi n$ is satisfied, where n is an integer. i.e.

$$\begin{aligned}
\mathbf{q} \cdot \mathbf{a}_1 &= 2\pi h \\
\mathbf{q} \cdot \mathbf{a}_2 &= 2\pi k \\
\mathbf{q} \cdot \mathbf{a}_3 &= 2\pi l
\end{aligned} \tag{3.27}$$

which are the Laue conditions for diffraction where h , k and l are integers. The general condition $\mathbf{q} \cdot \mathbf{r} = 2\pi m$ is satisfied if

$$\mathbf{q} = h\mathbf{b}_1 + k\mathbf{b}_2 + l\mathbf{b}_3 \tag{3.28}$$

where the \mathbf{b}_i 's are defined by

$$\mathbf{a}_i \cdot \mathbf{b}_j = 2\pi\delta_{ij} \tag{3.29}$$

where δ_{ij} is the Kronecker delta. Equations (3.28) and (3.29) define the Miller indices h, k, l and the reciprocal lattice parameters $\mathbf{b}_1, \mathbf{b}_2, \mathbf{b}_3$. It follows that the reciprocal lattice parameters must have the form

$$\mathbf{b}_1 = 2\pi \frac{\mathbf{a}_2 \times \mathbf{a}_3}{\mathbf{a}_1 \cdot \mathbf{a}_2 \times \mathbf{a}_3} \quad \mathbf{b}_2 = 2\pi \frac{\mathbf{a}_3 \times \mathbf{a}_1}{\mathbf{a}_1 \cdot \mathbf{a}_2 \times \mathbf{a}_3} \quad \mathbf{b}_3 = 2\pi \frac{\mathbf{a}_1 \times \mathbf{a}_2}{\mathbf{a}_1 \cdot \mathbf{a}_2 \times \mathbf{a}_3} \tag{3.30}$$

The above vectors form an array of points in k space. When the momentum transfer vector $\mathbf{q} = \mathbf{k}_f - \mathbf{k}_i$ touches one of these points the condition for diffraction will be met.

3.5 Finite Temperature Effects

In the above derivation we have so far assumed that the atoms occupy definite positions in the crystal lattice. At finite temperatures, however, the atoms will vibrate about their equilibrium positions. This causes the peak intensity to decrease as some of the intensity will disappear into a thermally diffuse background. This drop in intensity is described by the Debye-Waller factor in the structure factor

$$F(\mathbf{q}) = \sum_{j=1}^{N_c} f_j(\mathbf{q}) e^{-B q^2 / 16\pi^2} e^{i\mathbf{q}\cdot\mathbf{r}_j} \quad (3.31)$$

The Debye-Waller parameter B is related to the mean square thermal vibrational amplitude $\langle u^2 \rangle$ by

$$B = 8\pi^2 \langle u^2 \rangle \quad (3.32)$$

The Debye-Waller parameter is actually dependent upon direction although here it is written as though it is isotropic. The structure factor represented in equation (3.31) is the form that is used when analysing data. Values of B are obtained from the International Tables for X-ray crystallography (1974, 1983).

3.6 Surface X-ray Diffraction

3.6.1 The Truncated Bulk Crystal

Mathematically a surface can be formed by truncating an infinite crystal. Equation (3.19) can be expressed separately into in-plane and out-of-plane parts as

$$E_s(\mathbf{r}) = -r_e E_0 \frac{e^{-ikr}}{r} F(\mathbf{q}) \sum_{n_1=0}^{N_1-1} \sum_{n_2=0}^{N_2-1} e^{i\mathbf{q}\cdot(n_1\mathbf{a}_1+n_2\mathbf{a}_2)} \sum_{n_3=0}^{N_3-1} e^{i\mathbf{q}\cdot n_3\mathbf{a}_3} \quad (3.33)$$

Since a scale factor is used in X-ray diffraction data analysis and what we measure is the modulus squared of the above all of the terms before $F(\mathbf{q})$ can be ignored. Moreover, if we analyse the above expression for the specular reflectivity ($h=0$ and $k=0$), so that we are only examining the profile of the amplitude in a direction perpendicular to the surface, the double summation involving the in plane parameters \mathbf{a}_1 and \mathbf{a}_2 can also be ignored. Equation (3.33) can therefore be simplified to

$$E_s(\mathbf{r}) = F(\mathbf{q}) \sum_{n_3=0}^{N_3-1} e^{i\mathbf{q} \cdot n_3 \mathbf{a}_3} \quad (3.34)$$

If we make use of equations (3.27) this can be rewritten in the form

$$E_{00}(l) = F_{00}(l) \sum_{n_3=0}^{N_3-1} e^{i2\pi l \cdot n_3 a_3} \quad (3.35)$$

Since the X-ray beam will be attenuated the expression is modified. The result using the linear absorption coefficient μ is

$$E_{00}(l) = F_{00}(l) \sum_{n_3=0}^{N_3-1} e^{i2\pi l \cdot n_3 a_3} e^{-n_3 a_3 / \mu} \quad (3.36)$$

The attenuation factor makes the above series convergent. If we let N_3 tend to ∞ the result for a geometric progression gives

$$E_{00}(l) = F_{00}(l) \frac{1}{1 - e^{2\pi i l} e^{-a_3 / \mu}} \quad (3.37)$$

This is the general equation for the specularly reflected amplitude as a function of l for a bulk terminated crystal. Equation (3.37) tells us that there is always a scattered amplitude between Bragg reflections in a direction perpendicular to the surface.

Since the absorption coefficient μ is much larger than the lattice parameter perpendicular to the surface a_3 . Equation (3.37) can be written as

$$E_{00}(l) = F_{00}(l) \frac{1}{1 - e^{2\pi i l}} \quad (3.38)$$

or as

$$E_{00}(l) = F_{00}(l) \frac{-e^{-\pi i l}}{2 \sin \pi l} \quad (3.39)$$

This formula is clearly incorrect at integer values of l where $E_{hk}(l)$ tends to infinity. At these points, which correspond to Bragg points, we need to take into account the absorption i.e. we need to use equation (3.37). Equation (3.39) is, however, accurate away from integer values of l . At a position halfway between two Bragg peaks ($l=0.5, 1.5 \dots$) the scattering is equivalent to 0.5 monolayers. It is this position, known as the anti-Bragg or antiphase condition, which offers maximum sensitivity to the presence of monolayer islands on the surface and is used in the monitoring of epitaxial growth in real time (Norris 1993).

The modification of the scattering in between the Bragg peaks is not limited to the specular reflectivity. Diffuse streaks perpendicular to the surface will connect all of the Bragg points. These streaks are all a result of the surface. In reciprocal space the streaks form a series of rods which are perpendicular to the surface. These rods are known as crystal truncation rods (CTRs). An infinite crystal and a semi-infinite crystal in real and reciprocal space are illustrated in figure 3.1.

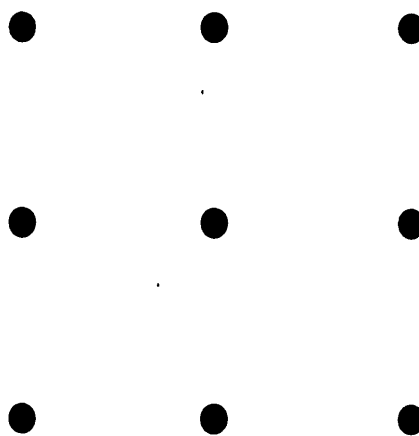
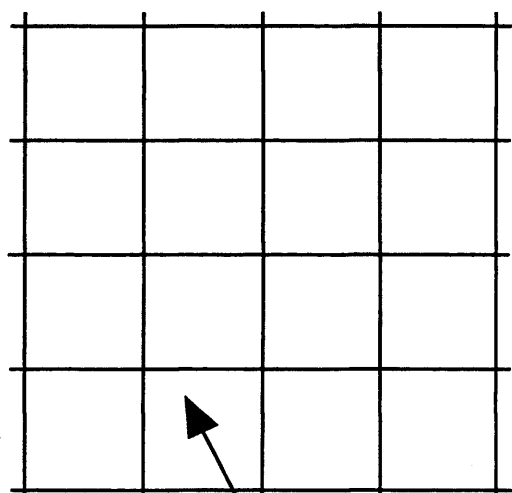
3.6.2 Surfaces

If the surface of a crystal has a different periodicity to the bulk or relaxes normally to the surface then we have a modification of the scattering along the crystal truncation rods. If the periodicity of the surface is a multiple to that of the bulk, fractional order rods occur as well as the CTRs. These fractional order rods do not interfere with the bulk scattering and only give information on the surface structure and not on its registry with the bulk crystal. The $(00l)$ rod due to the surface can be described by a summation.

$$E_{00}^{surface}(l) = F_{00}^{surface}(l) \sum_{n=1}^N \theta_n e^{-2\pi i l Z_n / a_3} \quad (3.40)$$

Where N is the number of surface layers, Z_n is the height of each layer from the bulk truncated crystal, θ_n is the coverage and $F_{00}^{surface}(l)$ is the structure factor due to the surface. Often this is defined in terms of the lattice parameters of the bulk if the surface structure has a simple relation to the bulk structure. We also have to substitute different atomic form factors if the surface consists of a different

Infinite Lattice



Unit Cell

$$\rho(\mathbf{r}) \longrightarrow F(\mathbf{q})$$

Semi-infinite Lattice

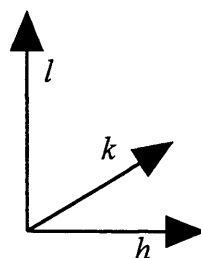
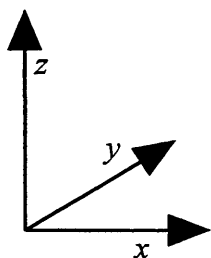
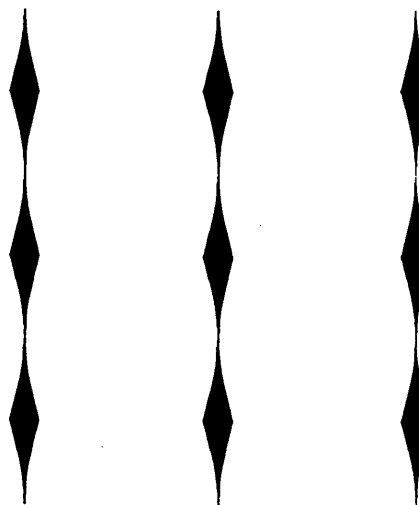
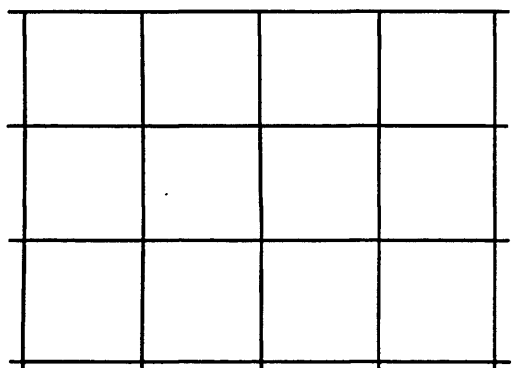


Figure 3.1. A schematic of real and reciprocal space for an infinite lattice and a semi-infinite lattice.

element to the bulk. We have assumed, by leaving the structure factor out of the summation, that the surface consists of one element. This may not be the case and we will then have to put the structure factor into the summation so that different form factors can be used.

To obtain the total scattering the surface and bulk contributions to the scattering amplitude are simply added.

$$E_{hk}^{total}(l) = E_{hk}^{bulk}(l) + E_{hk}^{surface}(l) \quad (3.41)$$

Figure 3.2 shows examples of how the above describes the specular rod ($h=0$ and $k=0$ for an (001) surface) from a simple cubic bulk lattice (1), a surface structure of a different element (b) and this surface structure on top of the bulk crystal (c).

3.7 The Integrated Intensity

The problem with the intensity given by equation (3.24) is that it is not a measurable quantity. This is because in deriving this we have assumed that the detector is a δ function in reciprocal space, that the impinging X-ray beam has zero wavelength spread and that the crystal is perfectly ordered. In reality this is not true and all these effects will contribute to a diffraction peak width. In an experiment the crystal is rotated about the surface normal until all of the diffracted intensity from a given reflection has passed through the diffraction slits. The quantity measured in this way is called the integrated intensity.

Going back to equation (3.19) for the scattering amplitude and splitting up the summation will give us

$$E_s(\mathbf{r}) = -r_e E_0 \frac{e^{-ikr}}{r} F(\mathbf{q}) \sum_{n_1=0}^{N_1-1} e^{iq \cdot n_1 \mathbf{a}_1} \sum_{n_2=0}^{N_2-1} e^{iq \cdot n_2 \mathbf{a}_2} \sum_{n_3=0}^{N_3-1} e^{iq \cdot n_3 \mathbf{a}_3} \quad (3.42)$$

Now we need to evaluate the summations. For simplicity only the intensity from a single layer of atoms will be considered such that we can ignore the last summation term. We can change the summations to integrals by dividing the summed terms by the corresponding lattice parameters. The integral limits will

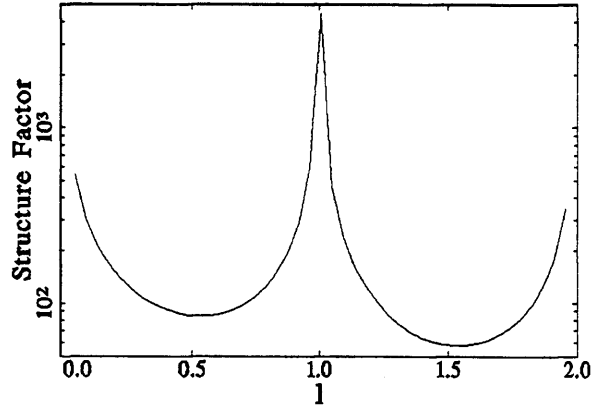
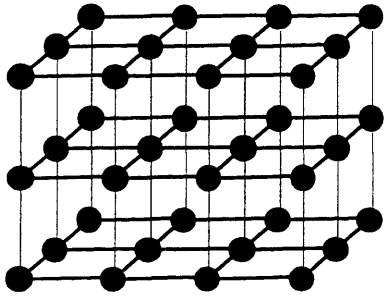


Fig 3.2 a) The bulk scattering $E_{hk}^{bulk}(l)$ from a truncated simple cubic lattice.

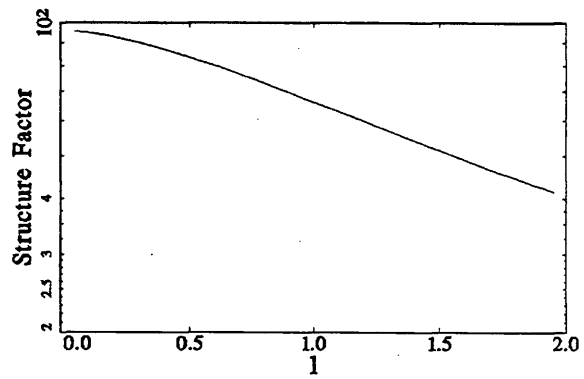
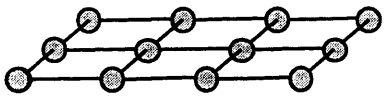


Fig 3.2 b) The surface scattering $E_{hk}^{surface}(l)$ from a simple square lattice.

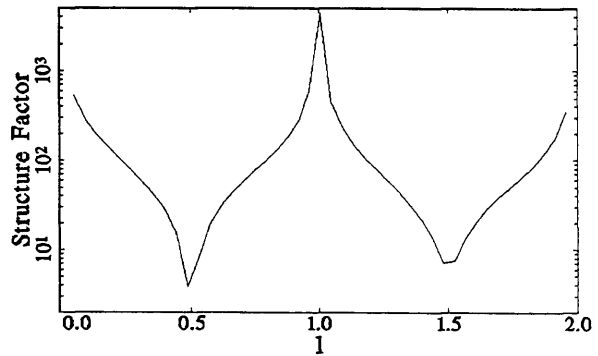
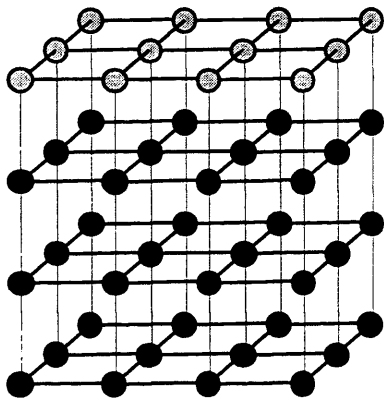


Fig 3.2 c) The total scattering $E_{hk}^{total}(l) = E_{hk}^{bulk}(l) + E_{hk}^{surface}(l)$ from a bulk solid as in a) having a surface b).

then be the lengths of the area along the h and k directions. Making use of the Laue conditions in (3.27) we obtain

$$E_s(\mathbf{q}) = -\frac{r_e}{A_u} E_0 \frac{e^{-ikr}}{r} F_{hkl} \int_0^{L_x} e^{-2\pi i h x / a_1} dx \int_0^{L_y} e^{-2\pi i k y / a_2} dy \quad (3.43)$$

where $x/a_1 = N_1$, $x/a_2 = N_2$ and $A_u = a_1 \times a_2$. Solving the integrals gives

$$E_s(\mathbf{q}) = -r_e E_0 \frac{e^{-ikr}}{r} F_{hkl} \frac{\sin \pi h L_x / a_1}{\pi h} \frac{\sin \pi k L_y / a_2}{\pi k} \quad (3.44)$$

Now taking the square of the modulus of the above gives us the intensity

$$I_s(\mathbf{q}) = I_0 \left(\frac{r_e}{r} \right)^2 |F_{hkl}|^2 \frac{\sin^2 \pi h L_x / a_1}{\pi^2 h^2} \frac{\sin^2 \pi k L_y / a_2}{\pi^2 k^2} \quad (3.45)$$

Now we need to obtain the differential scattering cross section. Since the differential scattering cross section is the number of X-ray photons scattered in a certain direction per unit time per unit solid angle divided by the incident flux

$$\frac{d\sigma}{d\Omega} = \frac{I_s(\mathbf{q}) dA}{I_0 d\Omega} \quad (3.46)$$

The area element dA appears because the incident flux is defined here as the number of photons crossing a point per unit time per unit area i.e. I_0/dA but as the solid angle element is given by $d\Omega = dA \cos i / r^2$, where i is the angle that a line parallel to r makes with the surface normal of the area element dA , the differential scattering cross section is now

$$\frac{d\sigma}{d\Omega} = \frac{I_s(\mathbf{q}) r^2}{I_0} \quad (3.47)$$

Substituting for $I_s(\mathbf{q})$ will lead to the equation

$$\frac{d\sigma}{d\Omega} = r_e^2 |F_{hkl}|^2 \frac{\sin^2 \pi h L_x / a_1}{\pi^2 h^2} \frac{\sin^2 \pi k L_y / a_2}{\pi^2 l^2} \quad (3.48)$$

The experimental arrangement is shown in figure 3.3. The incidence angle is denoted by β_{in} , the outgoing angle by β_{out} and the in plane scattering angle by 2θ . When measuring the integrated intensity the crystal is rotated at an angular velocity ω about the surface normal. The detector will accept the radiation over an angle $\Delta\psi$ along the in-plane direction and over $\Delta\lambda$ along the perpendicular direction. These are illustrated in figure 3.4. The total scattered intensity is now obtained by integrating the intensity over the acceptance of the detector and the time that it takes to scan the peak.

$$I_{int} = \int I_0 \frac{d\sigma}{d\Omega} dt d\psi d\lambda \quad (3.49)$$

if we define $d\alpha$ such that $dt = d\alpha/\omega$, then equation (3.49) can be written as

$$I_{int} = \frac{I_0}{\omega} \int \frac{d\sigma}{d\Omega} d\alpha d\psi d\lambda \quad (3.50)$$

The angles τ_1 and τ_2 are defined by $\tau_1 + \tau_2 = 2\theta$ and are shown in figure 3.4. The integration over time and space corresponds to an area element

$$dA = kq_1 \cos \tau_1 d\alpha d\psi \quad (3.51)$$

Using $\mathbf{q}_1 = h\mathbf{b}_1 + k\mathbf{b}_2$ we can express the area element in terms of the Miller indices. Treating the Miller indices as continuous it can be shown that (see appendix b) an area element in reciprocal space will have the form

$$dA = \frac{4\pi^2}{A_u} dhdk \quad (3.52)$$

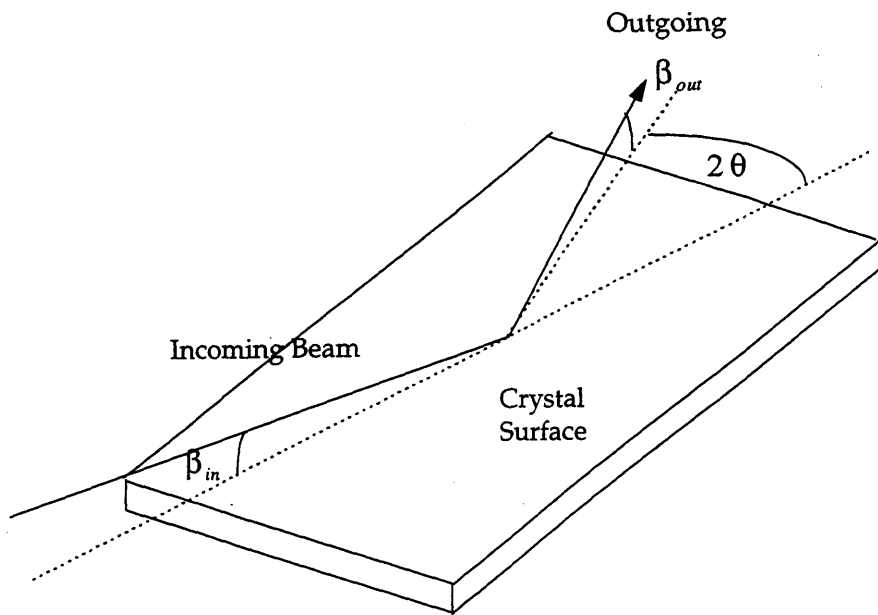


Figure 3.3. Schematic of a typical surface X-ray diffraction geometry. Also shown are the incoming angle β_{in} , outgoing angle β_{out} and the in-plane scattering angle 2θ .

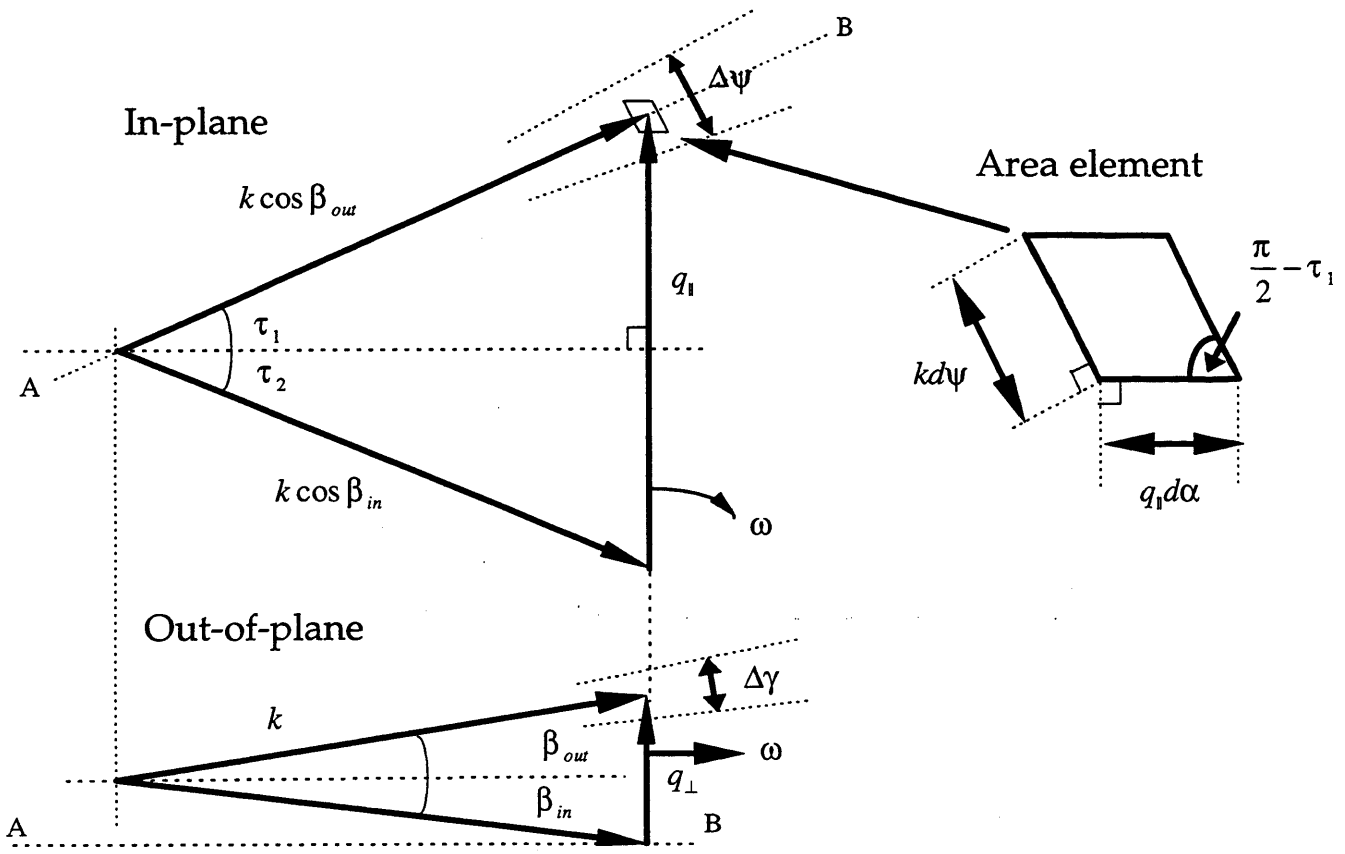


Figure 3.4. The geometry used for deriving the integrated intensity of a reflection. The top part of the diagram is a projection of the top view whilst the bottom part is a cross sectional view along the line AB. Also shown is a more detailed part of the top diagram showing the area element over which the intensity is integrated.

where A_u is the area of the surface unit cell. If this result is used with equation (3.51) to eliminate dA we get

$$d\alpha d\psi = \frac{4\pi^2}{A_u} \frac{1}{kq_{\parallel} \cos \tau_1} dh dk \quad (3.53)$$

If we make use of the definition of the Lorentz factor $F_{Lor} = k/q_{\parallel} \cos \tau_1$ then this reduces to

$$d\alpha d\psi = \frac{\lambda^2}{A_u} F_{Lor} dh dk \quad (3.54)$$

Substituting equation (3.54) and (3.46) into equation (3.50) will give

$$I_{int} = r_e^2 \frac{I_0}{\omega} \frac{\lambda^2}{A_u} F_{Lor} \int \frac{\sin^2 \pi h L_x / a_1}{\pi^2 h^2} dh \int \frac{\sin^2 \pi k L_y / a_2}{\pi^2 k^2} dk \int |F_{hkl}|^2 d\gamma \quad (3.55)$$

The integrals over dh and dk are tabulated. Moreover, we can assume that F_{hkl} is constant over the interval $d\lambda$ so that (3.55) is simplified to

$$I_{int} = r_e^2 \frac{I_0}{\omega} \frac{\lambda^2}{A_u} F_{Lor} \frac{L_x}{a_1} \frac{L_y}{a_2} |F_{hkl}|^2 \Delta\gamma \quad (3.56)$$

Substituting $A = L_x \times L_y$, the illuminated surface on the sample and $A_u = |\mathbf{a}_1 \times \mathbf{a}_2|$ the area of the surface unit cell yields

$$I_{int} = r_e^2 \frac{I_0}{\omega} \frac{\lambda^2 A}{A_u^2} F_{Lor} |F_{hkl}|^2 \Delta\gamma \quad (3.57)$$

Near the beginning of this chapter the vector nature of E was ignored. This is accounted for by putting a polarisation factor P into the result above so that

$$I_{int} = r_e^2 \frac{I_0}{\omega} \frac{\lambda^2 A}{A_u^2 P} F_{Lor} |F_{hkl}|^2 \Delta\gamma \quad (3.58)$$

In equation (3.58) only the illuminated surface area A , the Lorentz factor F_{Lor} , the polarisation factor P and the structure factor F_{hkl} will vary. The other terms are constant and are accounted for by using a scale factor in the analysis. The forms of the terms A , F_{Lor} and P will be discussed in chapter 4.

Chapter 4

Experimental Details

4.1 Introduction

This chapter describes the techniques and equipment used for collecting X-ray diffraction data. Since a surface is sensitive to contamination it is important to keep it clean during an experiment. This problem is aggravated by the amount of time measurements take (typically several hours) so an extremely clean environment, with a base pressure of 10^{-10} mbar, is necessary. A good vacuum is also required for techniques which employ low energy electrons such as Auger electron spectroscopy (AES) and low energy electron diffraction (LEED) to check the cleanliness and order of the surfaces. To detect the weak X-ray scattering from the surface, high intensity radiation is needed. This radiation is provided by a synchrotron. The scattered radiation from the crystal is measured, by either a solid state detector or a scintillation counter. The scattering geometry is provided by a six circle diffractometer.

The actual quantity measured in experiment is the integrated intensity. The deduction of the structure factors from the measured integrated intensities is achieved by the careful use of correction factors.

4.2 The UHV Chamber

The ultra high vacuum (UHV) chamber used at Daresbury laboratory is shown in figure 4.1. This has several ports which point at the sample that allow an electron analyser and gun for Auger electron spectroscopy, an argon gun, for sputtering and several vapour sources to be connected for a particular experiment. There is also a large port at the back of the chamber which is suitable either for a sample transfer system or LEED optics. A beryllium window allows incident X-rays to enter and scattered X-rays to leave the chamber.

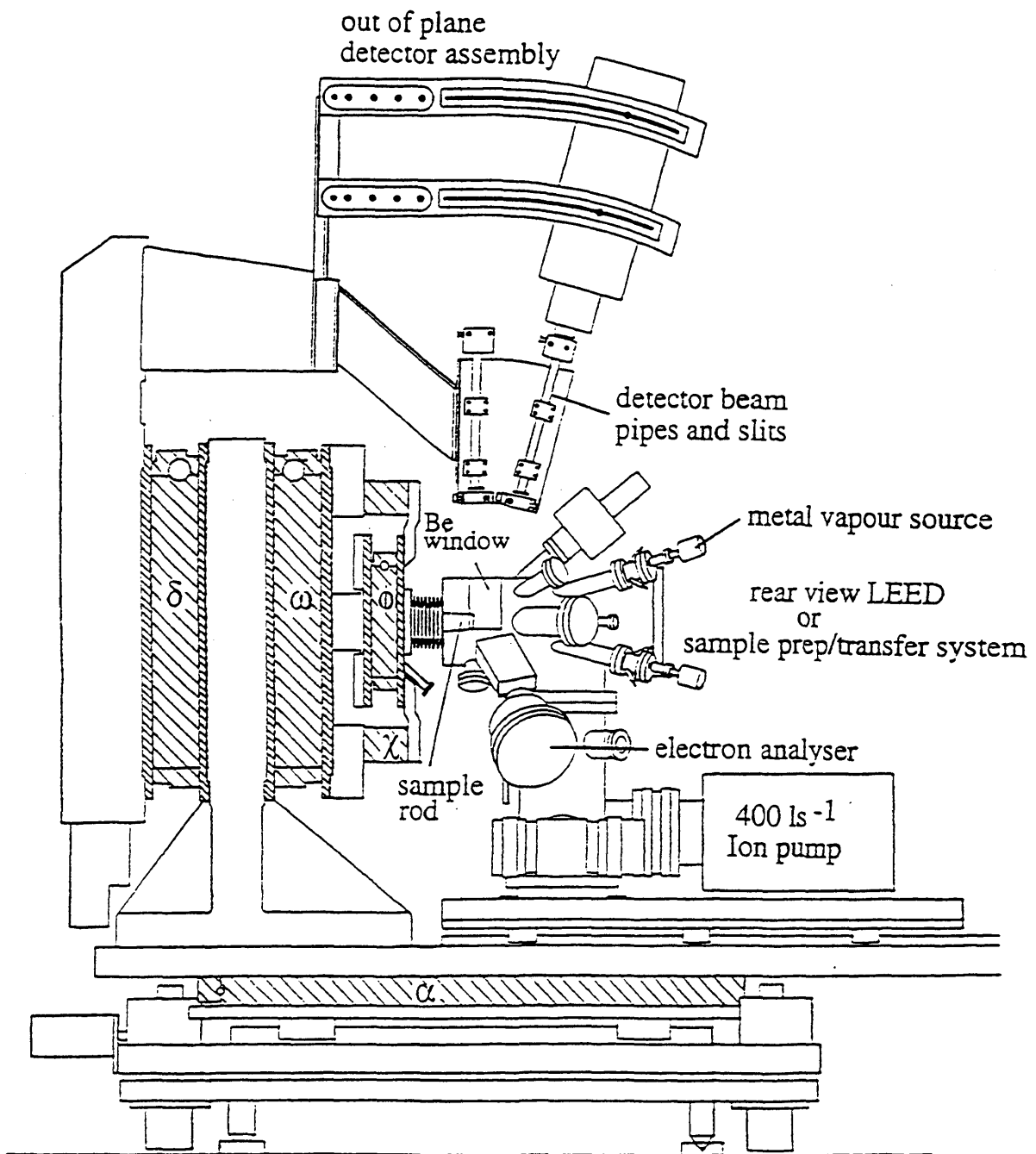


Figure 4.1. Schematic of the UHV environmental chamber used for SXR measurements mounted on the X-ray diffractometer showing the out-of-plane detector assembly.

Sample manipulation is achieved with a differentially pumped rotary seal (Taylor 1991). This consists of two stages: a high vacuum stage at 10^{-6} mbar and a low vacuum stage at 10^{-3} mbar. This allows the sample to be rotated by the diffractometer without any measurable effect on the vacuum inside the main chamber. The rotary seal is connected to the main chamber by a set of bellows. This allows further movement of the sample by the six circle diffractometer. A sample manipulator that allows cooling of the sample is also available (Taylor and Norris 1994, 1997). Both sample manipulators allow the sample to be transferred.

The chamber on the surface X-ray diffraction station on beamline ID3 (insertion device 3) at the European Synchrotron Radiation Facility (ESRF) is similar. It has a reflection high energy electron diffraction (RHEED) gun and greater out-of-plane access. As a result their sample transfer system remains on the chamber.

4.3 Sample Preparation

The substrates used in this work were either Ag(001) and Cu(001). They were spark cut to within 1° of the (001) crystallographic plane from 99.9999% purity boules, provided by Metal Crystals and Oxides Ltd, by the Centre for Materials Science at Birmingham University. The dimensions are shown in figure 4.2. Following this they were mechanically polished within 0.1° of the (001) plane. The alignment for the polishing was achieved using Laue diffraction from the crystal and then adjusting the goniometer that held the sample in place.

Cu crystals were electropolished in a solution of 2:1 orthophosphoric acid and water for 15 minutes with a current and voltage of 20mA and 1.5V. This was followed by rinsing the Cu crystal in a very weak orthophosphoric acid solution and then distilled water.

Several cycles of sputtering and annealing were used to obtain atomically ordered and clean samples once they were in the vacuum chamber. For Cu samples, repeated 15 minute sputters at 1kV followed by 15 minute anneals at 500°C were used. For the Ag samples the same sputtering method was used but the anneal time

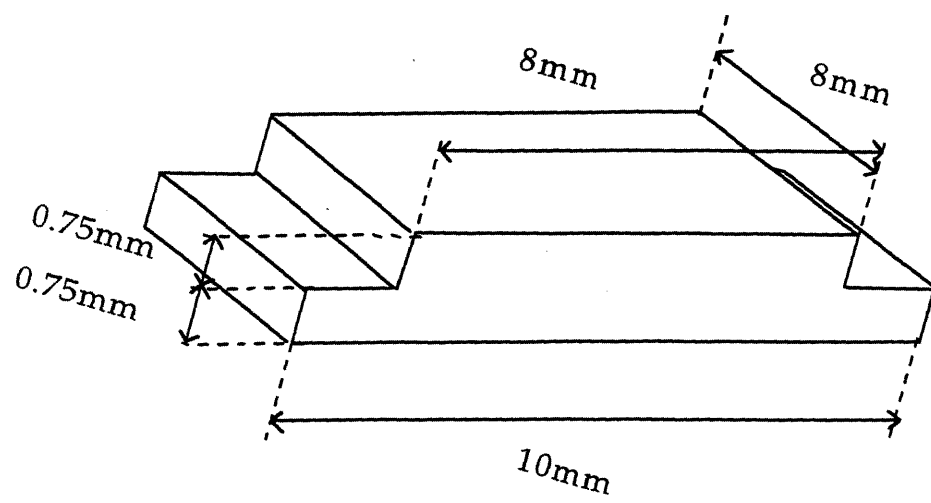


Figure 4.2. Dimensions of the substrates used in the experiment.

was increased to an hour. The cleanliness and atomic order was checked with LEED and AES. When removing a deposited layer care was taken to remove all of the adsorbate atoms before annealing to avoid possible interdiffusion of these atoms into the substrate.

4.4 Synchrotron Radiation

The widespread and increasing use of synchrotron sources for research reflects the unique properties of the radiation. An electron synchrotron, or more commonly an electron storage ring, provides a highly collimated and intense beam of radiation with a broad, continuous range of energies. The radiation is highly polarised in the plane of the electron orbit and the source is ultra clean. Any one of these properties would, by itself, be useful but all five together makes synchrotron radiation a powerful probe of all forms of matter from atoms and molecules to large complex structures found in living organisms

An electron storage ring (figure 4.3) consists of a series of straight sections joined together so as to form a polygon. At each bend is situated a bending dipole magnet that produces a field in the vertical direction. Electrons passing through this arrangement will pass through the straight sections and then, as they pass through the field, be bent through a circular arc, by means of the Lorentz force. This sends the electron through the next straight section. When the electron is subjected to this force it accelerates to the centre of the arc and, therefore, emits electromagnetic radiation. If the electron is moving at speeds close to the speed of light the classical toroidal distribution of the energy in the electrons rest frame becomes a highly collimated beam in the frame of the laboratory.

To offset the energy lost in producing the radiation each electron bunch is accelerated in each orbit by the radio frequency cavity. A series of quadrupole magnets is used to keep the bunches focused.

The synchrotron radiation source (SRS) at Daresbury laboratory has a beam energy of 2GeV. In a typical multibunch mode the beam parameters are around 200mA current and 24 hours lifetime. At the ESRF the beam energy is 6Gev with a beam current and lifetime of 100mA and 24 hours.

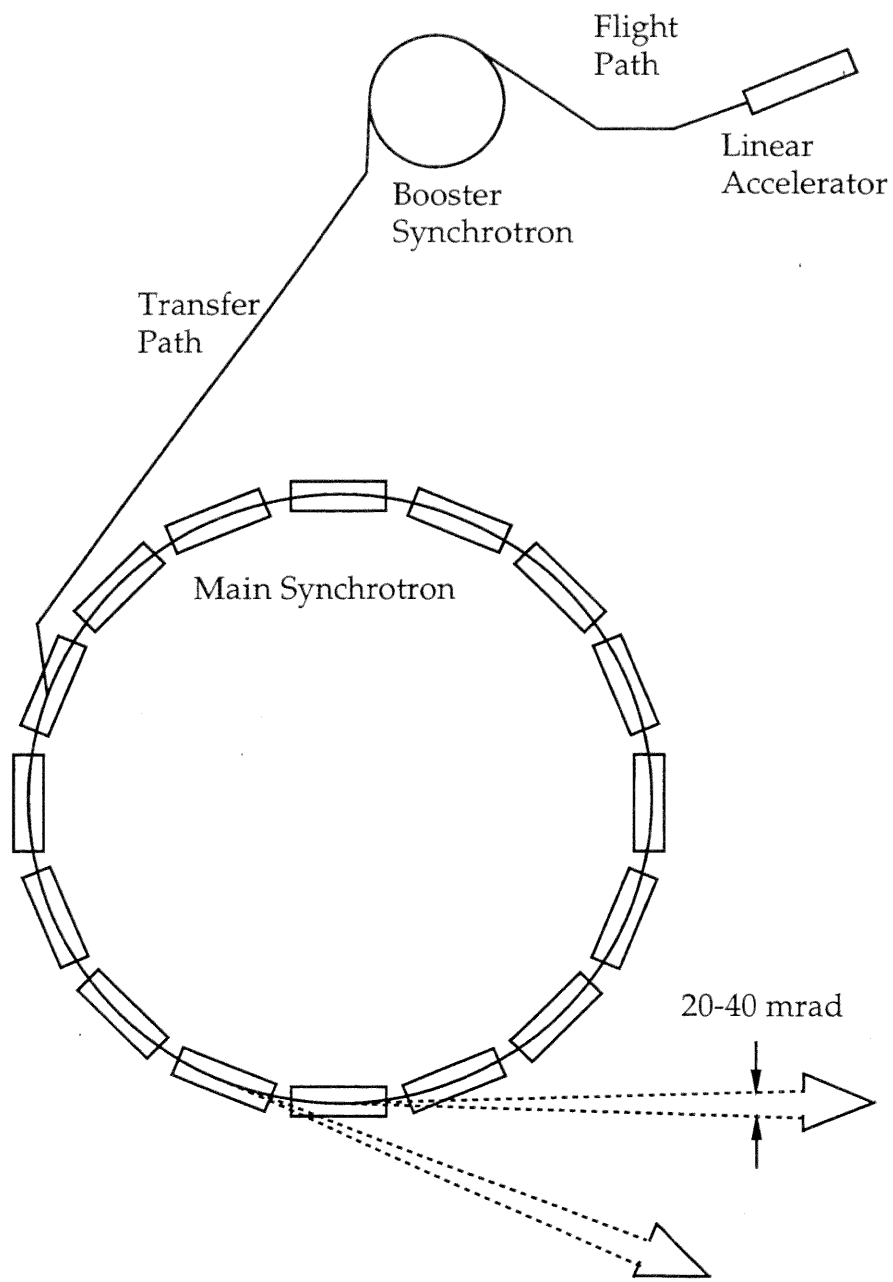


Figure 4.3. Schematic of a synchrotron radiation source.

4.5 Beamlines

4.5.1 Beamline 9.4 at Daresbury Laboratory

In addition to using dipole bending magnets, to produce synchrotron radiation, insertion devices can be employed. These are placed along the straight sections of the storage ring. Figure 4.4 shows a schematic of beamline 9.4 at Daresbury laboratory (Norris *et al* 1992). This line makes use of radiation produced from a Wiggler which is a type of insertion device (Baynham 1978). The wiggler consists of three liquid helium cooled magnets that produce a magnetic field of 5T. They are arranged so that the middle magnet has opposite polarity to the two outer ones. When an electron enters the field produced by this configuration it is forced into a wiggle in the plane of the orbit. The reduced bending radius, by comparison to that produced by a bending magnet shifts the spectrum of radiation to higher energies. The central part of the fan of radiation produced from the wiggler magnet reaches a double focusing toroidal mirror. A mirror is used to focus the radiation because the refractive index of X-ray radiation is very close to unity. Suitable wavelengths are chosen using a channel cut Si(111) monochromator.

At the end of the beamline an air filled ion chamber measures the total flux. This is essential to normalise the data and thus allow for any variations in the incident intensity. The ion chamber is separated from the monochromator by a beryllium window. Situated just before the monitor are a set of four jaw slits that define the area of beam reaching the sample.

The beamline is not connected to the vacuum chamber which moves with the diffractometer table. The radiation, therefore, passes through a small air space before entering and leaving the vacuum chamber via a beryllium window. The scattered radiation then enters the detector beampipe. This is either evacuated or filled with He to reduce scattering of the X-rays by air. The two sets of slits, before and after the beampipe, define the amount of radiation that is detected and the resolution perpendicular to the surface. The actual detector consists of a Ge crystal. X-ray photons reaching the Ge detector will generate electrical signals that are

SPECIAL NOTE

**THIS ITEM IS BOUND IN SUCH A
MANNER AND WHILE EVERY
EFFORT HAS BEEN MADE TO
REPRODUCE THE CENTRES, FORCE
WOULD RESULT IN DAMAGE**

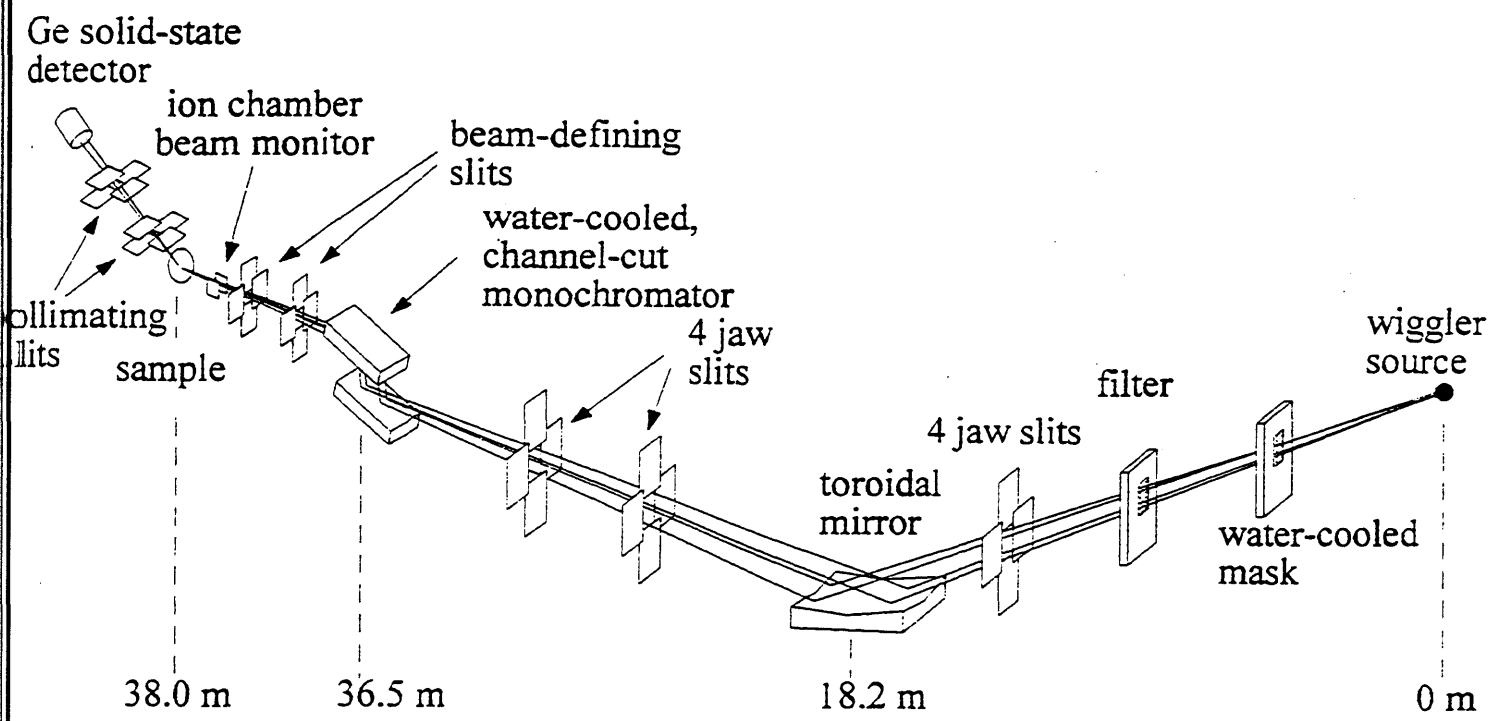
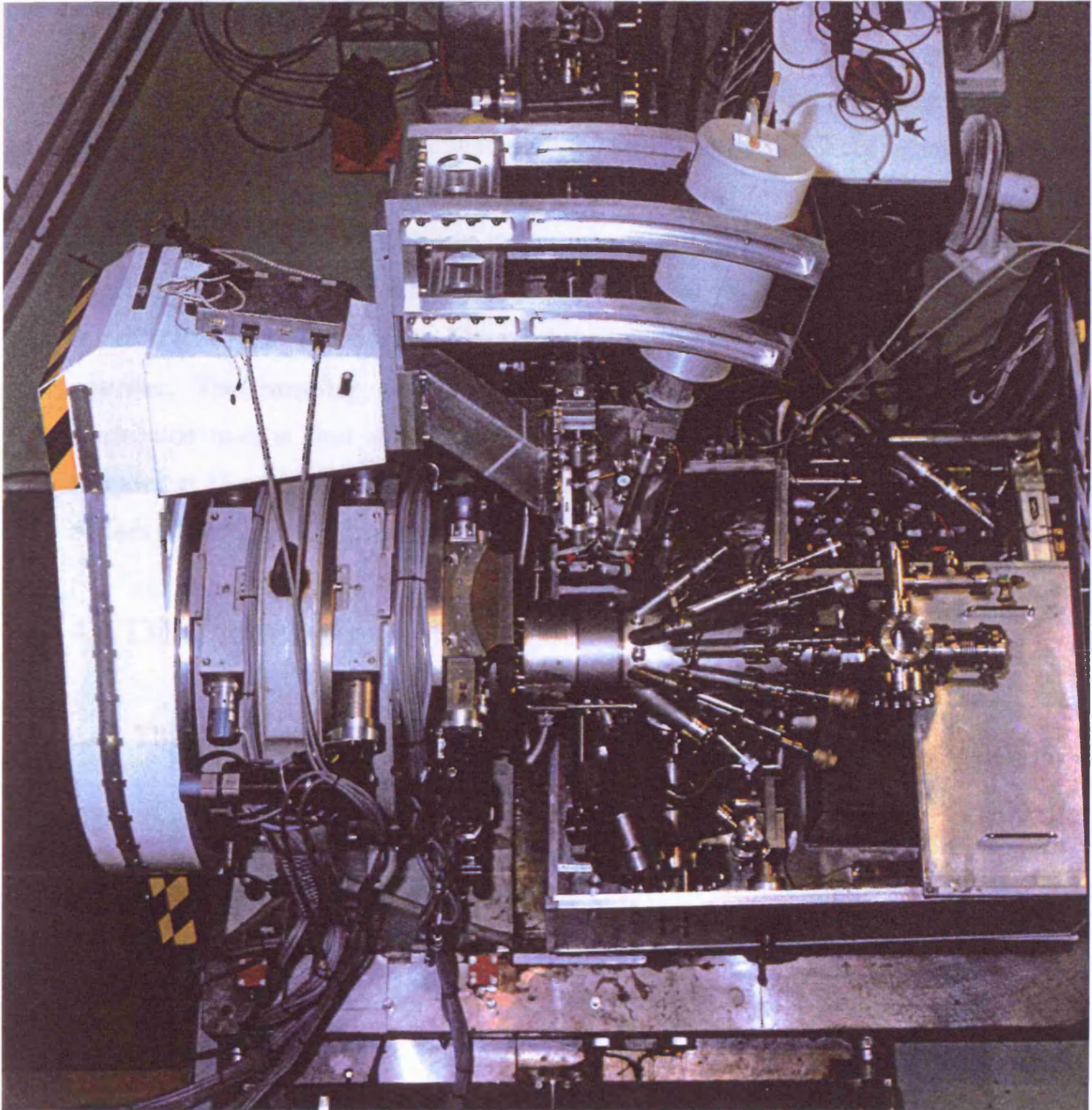


Figure 4.4. Schematic of beamline 9.4 of the SRS at Daresbury laboratory.

Plate 4.1. A top view of the experimental set up on the surface X-ray diffraction station at Daresbury Laboratory

driven by a potential difference. To reduce thermal radiation, liquid nitrogen is used to cool the detector.

Fig. 1.10. The DSSP



amplified by a potential difference. To reduce thermal excitation liquid nitrogen is used to cool the detector.

4.5.2 ID3 at the ESRF

Beamline ID3 at Grenoble uses another type of insertion device: an undulator. This has several magnets that force the electron beam into several wiggles. If the angle of bend is less than the natural opening angle of the synchrotron radiation emitted from each wiggle, constructive interference can take place giving rise to a series of sharp peaks superimposed on the synchrotron radiation spectrum. The radiation from the undulator passes through two carbon foils before reaching a sagittally focusing cryogenically cooled Si(111) monochromator. A pair of mirrors are used to filter out harmonics. The scattered radiation is detected by a NaI scintillation counter. The smaller source size and the non-uniform spectral output of the undulator means that although the total flux is comparable to that produced by the wiggler at Daresbury, the monochromatised flux on the sample is more than two orders of magnitude greater.

4.6 Diffractometry

4.6.1 The Six Circle Diffractometer

To take advantage of the strong horizontal polarisation of the beam a vertical scattering geometry is used. This is to avoid the near zero polarisation factors that would occur at scattering angles close to 90° .

A schematic of the Frank-Heydrich diffractometer is shown in figure 4.5. The sample is oriented using three orthogonal axes ω , ϕ , and χ . The χ movement is provided by two parallel axes limiting the movement to $\pm 20^\circ$. The presence of the environmental chamber prevents the use of a conventional χ circle as employed in a standard four-circle diffractometer. The five circle diffractometer (Fuoss and Robinson 1984) consists of a 4-circle diffractometer mounted on top of a rotary table

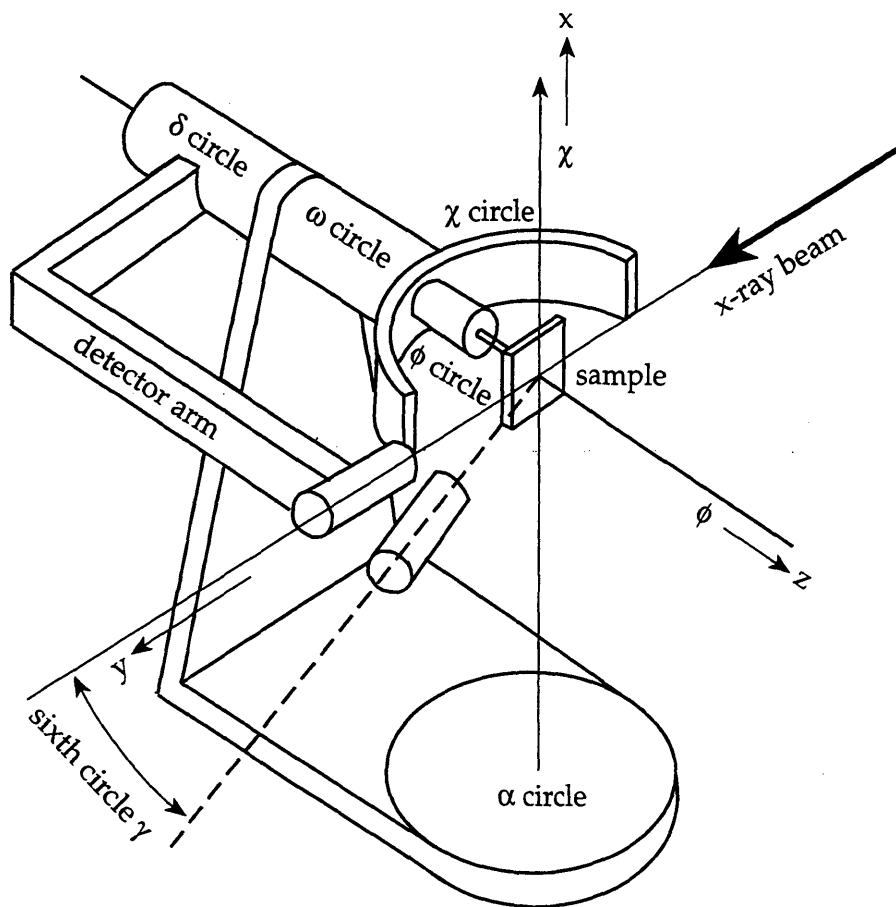


Figure 4.5. Schematic of the six circle diffractometer on station 9.4 of the SRS at Daresbury Laboratory.

which is controlled by the α circle. This enables the grazing angle to be set independently and increases the volume of reciprocal space that can be measured. The δ circle moves the detector about a horizontal axis.

In addition to the above circles a new γ movement has been commissioned that offers a cheap method to increase the measurable amount of reciprocal space (Taylor *et al* 1996). This circle only has two positions: one at 0° and another at 15° . To change from one position to the other requires manual adjustment. Such a configuration has several advantages over a fully motorised circle. For example a motorised circle would be expensive and would limit the weight of the detector. Moreover, all the fine tuning, that such a circle would provide, is already provided by the χ arcs.

The diffractometer on ID3 at the ESRF uses the same principle as that on beamline 9.4 at Daresbury laboratory. It was built by Huber and uses a motorised γ arm.

4.6.2 Crystallographic Alignment

The preliminary step in crystallographic alignment involves defining the physical surface normal of the crystal. This is achieved by reflecting a low divergence laser beam from the sample. The χ and ϕ circles are then adjusted until a full rotation of the ω circle causes the reflected laser beam to move no more than 1cm when 4m away from the sample. By doing this a trial angle position for a given hkl reflection can be calculated.

Full crystallographic alignment is then undertaken by searching for this reflection and then optimising the intensity by adjusting χ and ϕ . When this is done a second reflection is searched for and the procedure is repeated. A UB matrix, which relates the angular positions of the diffractometer to the crystallographic axes, can then be calculated. Further refinement of this UB matrix can be achieved by searching for more reflections (Vlieg 1987, Lohmeier and Vlieg 1993).

4.6.3 Measurement of Crystal Truncation Rods

Surface X-ray diffraction measurements involve measuring the integrated intensity of a particular hkl reflection. This is done by moving to a particular hkl point and then rotating the crystal about the surface normal, using the ϕ circle, with the detector fixed. This has the effect of scanning the whole region of reciprocal space where intensity is present. To define the resolution in l the out-of-plane detector slits are set to a desired value.

To obtain a value for the integrated intensity the background must be found. This is done by fitting a Lorentzian curve to the peak using a constant background. This background is then subtracted from the integration. Each reflection measured is normalised to the incident flux.

To measure a crystal truncation rod the above method is repeated as a function of l for suitable values for h and k . The structure factors for the rod are then obtained by use of the correction factors described in the last section of this chapter.

4.6.4 Choice of Base Vectors

For the fcc (001) surface of Cu or Ag the atomic arrangement is described by a body centred tetragonal unit cell defined by three orthogonal base vectors which are related to the conventional cubic coordinate system by:

$$\mathbf{a}_1 = \frac{1}{2}(1\bar{1}0)_{\text{cubic}} \quad \mathbf{a}_2 = \frac{1}{2}(110)_{\text{cubic}} \quad \mathbf{a}_3 = \frac{1}{2}(001)_{\text{cubic}} \quad (4.1)$$

with $|\mathbf{a}_1| = |\mathbf{a}_2| = a_0/\sqrt{2}$ and $|\mathbf{a}_3| = a_0$ where a_0 is the lattice constant of silver (4.086Å) or copper (3.615Å). This geometry is illustrated in figure 4.6. Using this convention \mathbf{a}_1 and \mathbf{a}_2 are both parallel to the surface and \mathbf{a}_3 is directed normal to the surface. The corresponding reciprocal lattice vectors are:

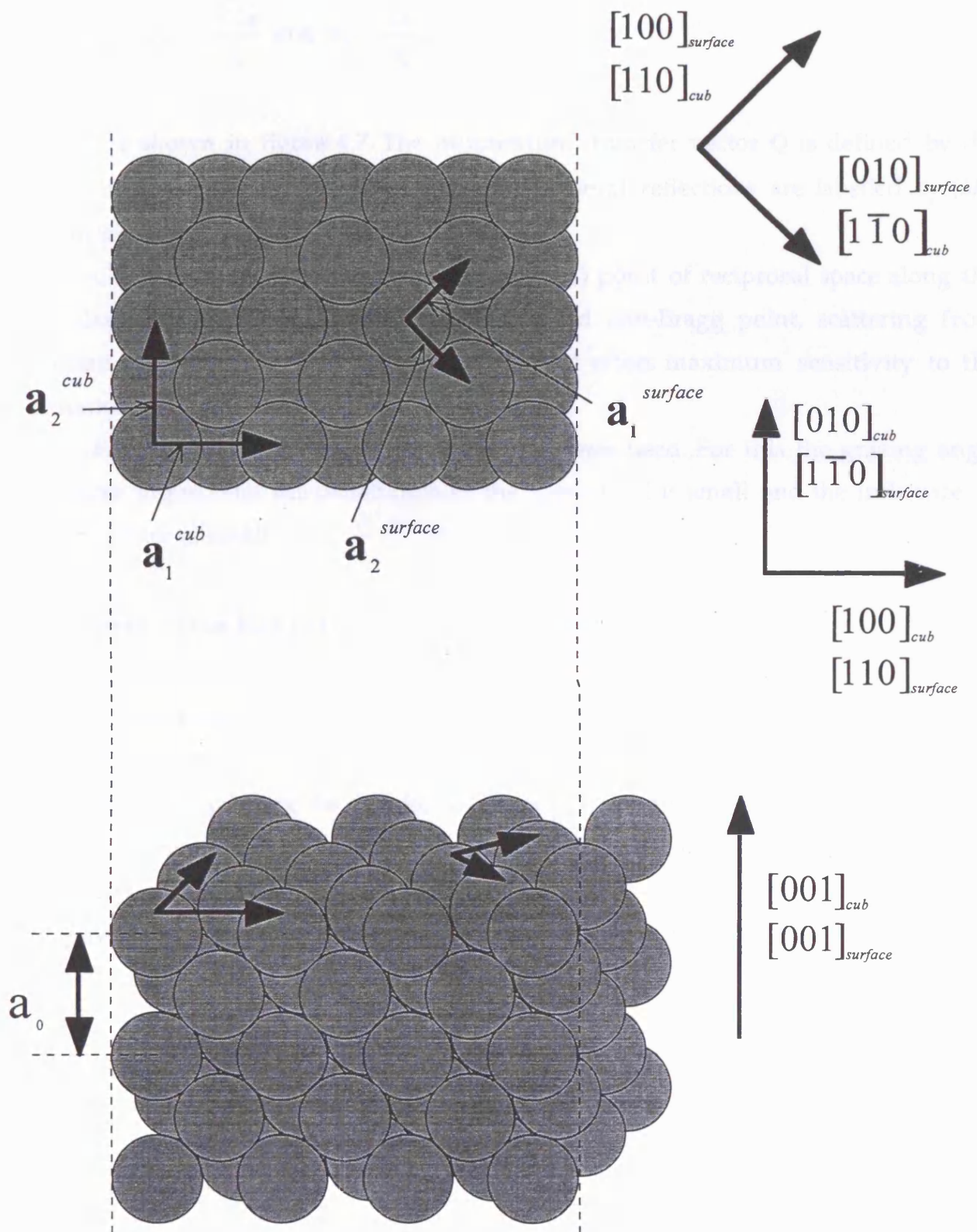


Figure 4.6. Schematic showing the base vectors used to describe the atomic geometry.

$$\mathbf{b}_1 = \frac{2\pi}{a_0}(1\bar{1}0)_{\text{cubic}} \quad \mathbf{b}_2 = \frac{2\pi}{a_0}(110)_{\text{cubic}} \quad \mathbf{b}_3 = \frac{2\pi}{a_0}(001)_{\text{cubic}} \quad (4.2)$$

$$\text{with } |\mathbf{b}_1| = |\mathbf{b}_2| = \frac{2\sqrt{2}\pi}{a_0} \text{ and } |\mathbf{b}_3| = \frac{2\pi}{a_0}.$$

These are shown in figure 4.7. The momentum transfer vector \mathbf{Q} is defined by the Miller indices (hkl) with $\mathbf{Q} = h\mathbf{b}_1 + k\mathbf{b}_2 + l\mathbf{b}_3$. General reflections are labelled by (hkl) and in-plane reflections ($l \sim 0$) by (hk) .

Growth is normally monitored at the (001) point of reciprocal space along the specular reflectivity. At this point, the so called anti-Bragg point, scattering from adjacent (001) atomic planes is out of phase and offers maximum sensitivity to the formation of monolayer height islands.

For some measurements the (100) point was used. For this the grazing angle was close to zero and the penetration of the X-ray field is small and the influence of bulk disorder is small.

4.7 Correction Factors

4.7.1 Introduction

Prior to analysing the data from a surface X-ray diffraction (SXRD) experiment certain correction factors need to be used. This is to allow for the experimental geometry.

The factors come from the equation relating the structure factor to the integrated intensity

$$I_{int} = r_e^2 \frac{I_0}{\omega} \frac{\lambda^2 A}{A_u^2 P} F_{Lor} |F_{hkl}|^2 \Delta\gamma \quad (4.3)$$

where r_e is the classical electron radius, I_0 is the intensity of the incident beam, ω is the angular velocity of rotation of the sample during the phi scan, λ is the

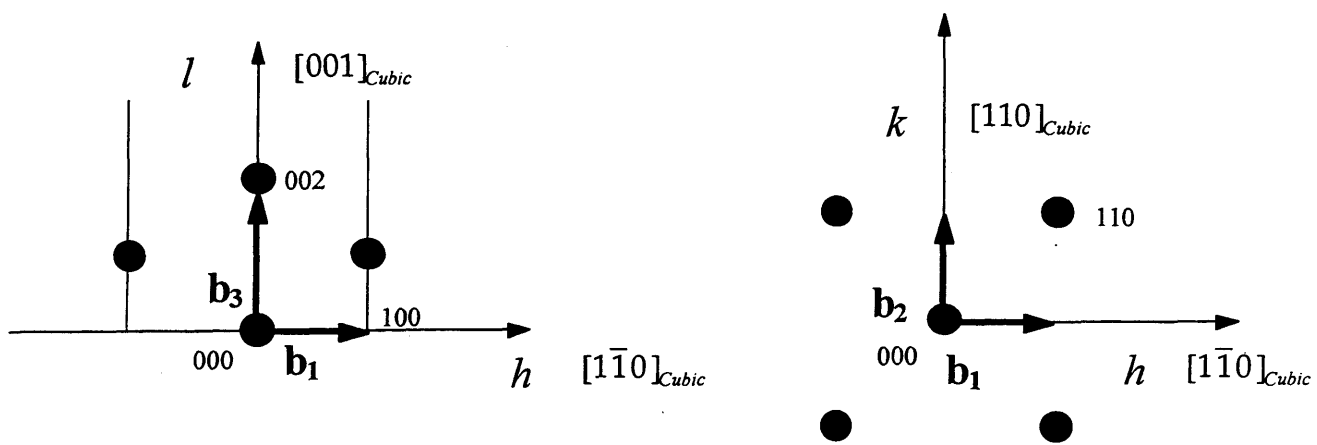


Figure 4.7. Diagram of reciprocal space for an fcc lattice.

wavelength of the radiation, A is the active sample area, A_u is the area of the unit cell, P is a factor to allow for the polarisation of the beam, F_{Lor} is the Lorentz factor, $|F_{hkl}|$ is the modulus of the structure factor and I_{int} is the integrated intensity.

From the experiment we will have the I_{int} for a set of points in reciprocal space. To unravel the structure we need to find $|F_{hkl}|$. Since the terms r_e , I_0 , ω , λ , and A_u are all constant we only need to consider A , P and F_{Lor} . These last three terms are the correction factors and are all consequences of the experimental geometry. The remaining constant terms will effectively merge into one the result being the scale factor which is found from the data analysis procedure.

The active sample area A , which is shown schematically in figures 4.8 and 4.9, is the illuminated area of the surface that is seen by the detector. Not all of the beam reflected from the sample will reach the detector because of the two sets of defining slits between the sample and the detector i.e. the illuminated surface area is not equal to the active sample area.

The Lorentz factor is defined by

$$F_{Lor} = \frac{k}{q_{\parallel} \cos \tau_1} \quad (4.4)$$

where k is the wave number of the radiation, q_{\parallel} is the projection of the momentum transfer vector on to the surface and τ_1 is the angle the projection of the outgoing vector k onto the surface makes with the normal of q_{\parallel} parallel to the surface (see figure 3.4). The Lorentz factor allows for the angle at which the Ewald sphere cuts the rod. The expression 4.4 is of no use in its present form and needs to be simplified to a form pertaining to the experimental geometry.

The polarisation factor is needed mainly for out of plane data. This is because synchrotron radiation is heavily polarised in the horizontal plane. For in-plane data this is very close to 1, however, for out-of-plane data it is important. This is because the projection of the wave amplitude onto the detector decreases as the angle from the in-plane position increases. The factor which allows for this will only depend on the position of the detector and not the position of the sample. The only angles that

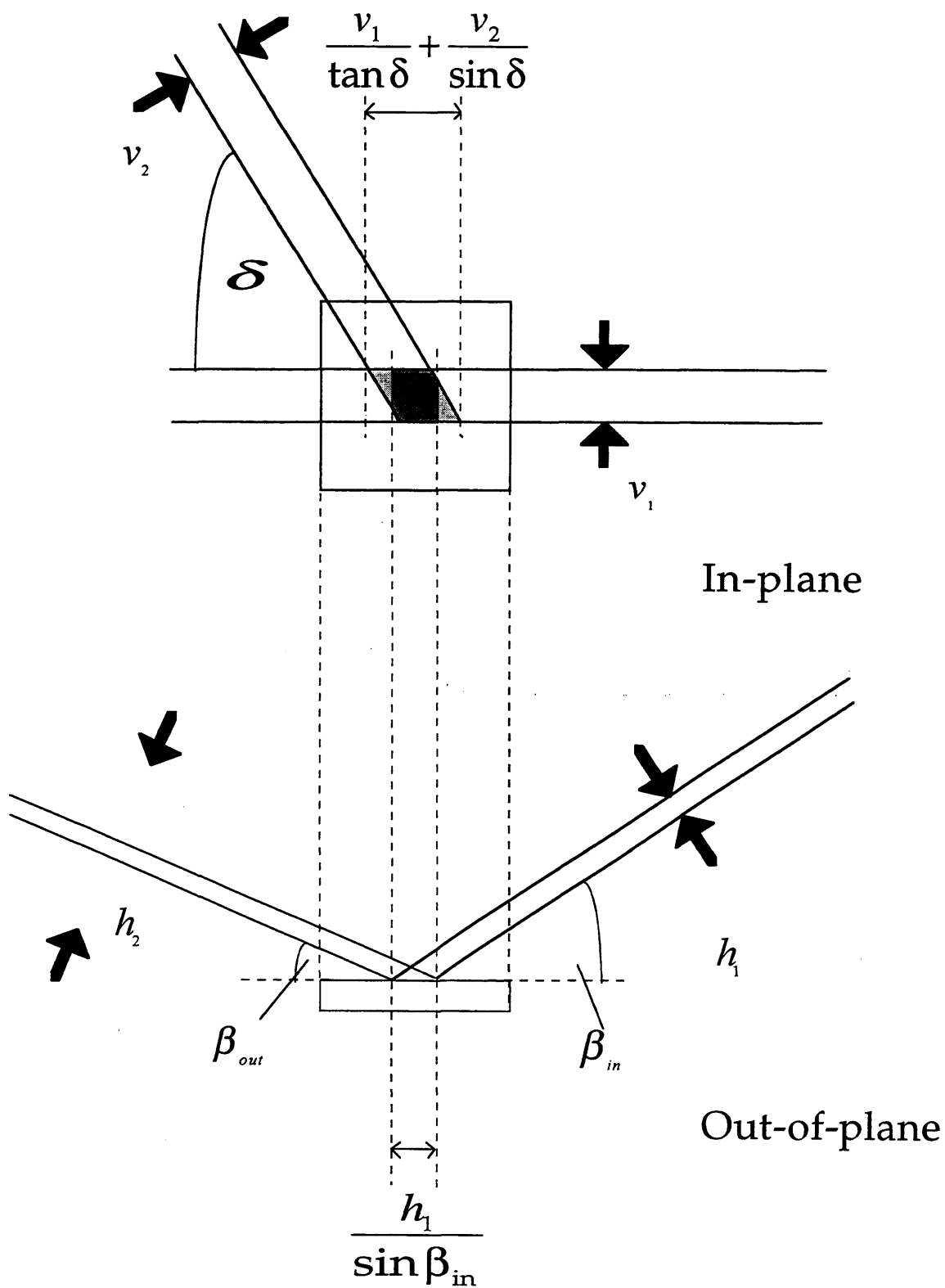
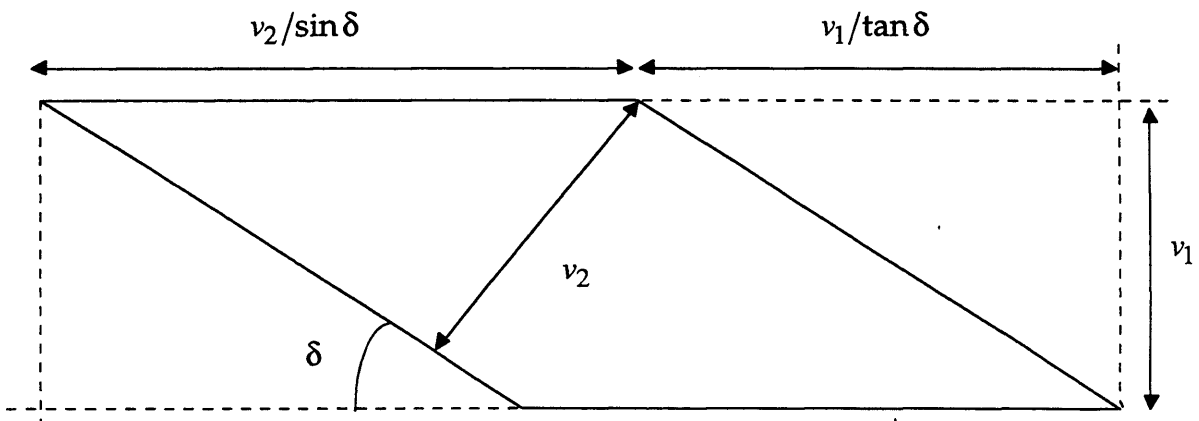
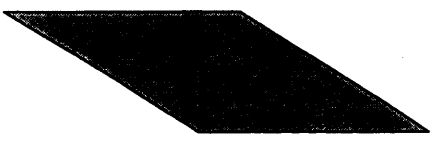


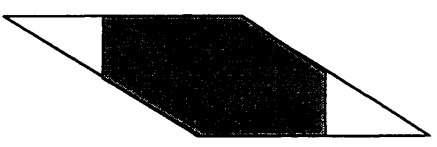
Figure 4.8. Schematic showing the active sample area in both in-plane and out-of-plane configurations.



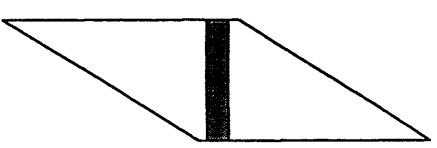
$$\frac{v_1}{\tan \delta} < \frac{v_2}{\sin \delta}$$



$$A = \frac{v_1 v_2}{\sin \delta}$$

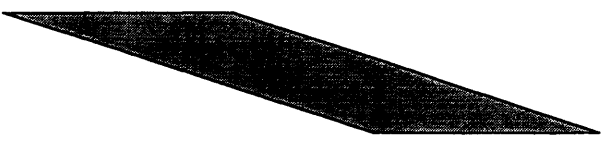


$$A = \frac{v_1 v_2}{\sin \delta} - \left(\frac{v_2}{\sin \delta} + \frac{v_1}{\tan \delta} - \frac{h_1}{\sin \beta_{in}} \right)^2 \frac{\tan \delta}{4}$$

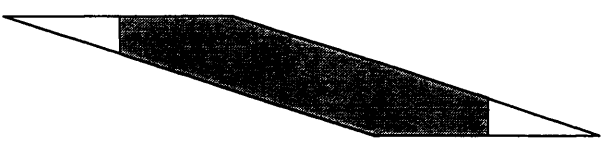


$$A = \frac{h_1 v_1}{\sin \beta_{in}}$$

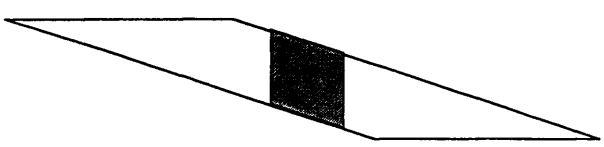
$$\frac{v_1}{\tan \delta} \geq \frac{v_2}{\sin \delta}$$



$$A = \frac{v_1 v_2}{\sin \delta}$$



$$A = \frac{v_1 v_2}{\sin \delta} - \left(\frac{v_2}{\sin \delta} + \frac{v_1}{\tan \delta} - \frac{h_1}{\sin \beta_{in}} \right)^2 \frac{\tan \delta}{4}$$



$$A = \frac{h_1 v_1}{\sin \beta_{in} \cos \delta}$$

Figure 4.9. Schematic showing how the form of the active sample area changes with the incoming angle.

move the detector are α and δ which move the detector about a vertical and horizontal axis respectively. The resulting correction factor is

$$P = \frac{1}{\sin^2 \delta + \cos^2 \delta \cos^2 \alpha} \quad (4.5)$$

To find the structure factor from the integrated intensity we require the above three correction factors and then simply use the formula

$$|F_{hkl}| = \sqrt{\frac{PI_{\text{int}}}{F_{\text{Lor}}A}} \quad (4.6)$$

which is basically equation (4.3) with the constant terms taken out. These are allowed for by using the scale factor.

4.7.2 In-plane Data

In-plane scans are achieved with the incident radiation and the detector at very small angles to the sample surface. The sample is therefore flooded with radiation in the horizontal direction. Therefore, it is only the vertical post-sample and pre-sample slits that define the area of beam that reaches the detector (figure 4.9). The area is given by

$$A = \frac{v_1 v_2}{\sin \delta} \quad (4.7)$$

where v_1 and v_2 are the separations of the vertical pre-sample and post-sample slits respectively and δ is the scattering angle projected onto the plane of the surface and not the actual scattering angle. Since we are using a scale factor during the data analysis we do not need the actual slit quantities unless they are changed during the experiment. As a result of this the only information we need to know is δ i.e.

$$A = \frac{1}{\sin \delta} \quad (4.8)$$

If we keep the incoming angle equal to the outgoing angle during the phi scans the Lorentz factor, given by equation (4.4), is simplified to

$$F_{Lor} = \frac{1}{\cos \beta \sin \delta} \quad (4.9)$$

Equation (4.5), describing the polarisation, cannot be simplified but since α is very close to 0° it is nearly equal to 1.

4.7.3 Out-of-plane Data

When measuring diffraction rods the polarisation factor keeps the form of equation (4.5). However, the Lorentz factor and active sample area may both change depending on the experimental geometry. The Lorentz factor will have the form of equation (4.9) when measuring the specular rod since here the rod is measured by symmetrically increasing the incoming and outgoing angles. For measuring other rods, this is not possible, and either the incoming or outgoing angles is kept at a suitable constant value. The area correction factor is also more involved for the out-of-plane measurements since the parallelogram formed on the sample surface for non-specular measurements will not always be flooded. The correction factors for the specular rod data will be discussed first. Following this the more involved case for non-specular rods will be dealt with.

4.7.4 The Specular Rod

The specular rod, as mentioned previously, is measured by symmetrically increasing the incoming and outgoing angles of the beam to the surface. Since the resulting diffraction vector is perpendicular to the surface only the distances normal

to the surface are probed. This actual geometry is realised by keeping δ at 0° , keeping the surface normal horizontal and then moving α and χ , in a horizontal plane, such that the incoming and outgoing angles remain equal.

The area of the beam on the surface will be a rectangle which will flood the sample along the horizontal direction at low angles. When the sample is flooded the area stays constant and has a value approximately given by

$$A = sv_1 \quad (4.10)$$

where s is the length of the sample in the horizontal direction and v_1 is the distance between the vertical pre-sample slits. When the sample is no longer flooded i.e. when $s \sin \theta > h_1$, where h_1 is the distance between the horizontal pre-sample slits, the area becomes

$$A = \frac{h_1 v_1}{\sin \theta} \quad (4.11)$$

Since v_1 appears in both of the formulae it is not necessary to include it since we are only worried about the parameters that change. Therefore we can say that when $s \sin \theta \leq h_1$,

$$A = s \quad (4.12)$$

and when $s \sin \theta > h_1$

$$A = \frac{h_1}{\sin \theta} \quad (4.13)$$

The Lorentz factor, as mentioned before, takes the form of equation (4.9). The polarisation factor in equation (4.5) can be simplified since δ is equal to 0° . The result is

$$P = \frac{1}{\cos^2 \alpha} \quad (4.14)$$

4.7.5 Non-specular Rods

The active sample area is a flooded parallelogram at low angles of incidence so it is given by equation (4.7). However, at slightly higher angles the triangles at the end of the parallelogram will not be illuminated (see figure 4.9). This area will need to be subtracted. The resulting area will be

$$A = \frac{v_1 v_2}{\sin \delta} - \left(\frac{v_2}{\sin \delta} + \frac{v_1}{\tan \delta} - \frac{h_1}{\sin \beta_{in}} \right)^2 \frac{\tan \delta}{4} \quad (4.15)$$

If the incoming angle increases to a high enough value the area will not have the form of equation (4.15). At this point the area of the beam will require more than the area of two triangles to be subtracted from the area of the parallelogram. The actual form of the correction factor will depend on the parallelogram. Figure 4.9 shows two slightly different parallelograms. The first one has the condition that $v_1/\tan \delta < v_2/\sin \delta$. In this case the area will be a simple rectangle of area

$$A = \frac{v_1 h_1}{\sin \beta_{in}} \quad (4.16)$$

The other is recognised by the condition $v_1/\tan \delta \geq v_2/\sin \delta$. Since the area is a parallelogram it is given by the equation

$$A = \frac{h_1 v_2}{\sin \beta_{in} \cos \delta} \quad (4.17)$$

The Lorentz factor represented by equation (4.5) can be simplified to

$$L = \frac{1}{\cos \beta_{in} \cos \beta_{out} \sin \delta} \quad (4.18)$$

(Arndt and Willis 1966) and the polarisation factor keeps the form of equation (4.5).

4.7.6 Gamma Circle Correction Factor

At the ESRF the six circle diffractometer's gamma circle moves along an axis parallel to the surface normal rather than about a true circle. Due to this the resolution function changes as a function of the outgoing angle. To correct for this the integrated intensity is multiplied by $1/\cos \beta_{out}$.

Chapter 5

The Growth and Structure of Chromium on Copper (001)

5.1 Summary

In this chapter the growth and structure of ultrathin Cr films on Cu(001) is described. The featureless decay of the intensity of the specularly reflected X-ray beam recorded at room and higher temperatures is shown to be consistent with the growth of a multilayered film. At 100K the time plot shows a feature which is attributed to a poorly defined layer-by-layer growth mode. In-plane scans show that a bulk bcc phase, with bcc (110) plane parallel to fcc (001) plane of the Cu substrate develops for thicknesses greater than about 1 monolayer (ML) at room temperature. The specular reflectivity for two films of thickness equivalent to 0.5ML and 1.0ML were scanned as a function of momentum transfer normal to the surface. The plots were fitted using four different roughness models to fix the occupancies in each layer. Although the 0.5ML scan could be fitted with any of the models the 1.0ML scan was consistent with a linear model. The fit to the 1.0ML film was considerably improved with an unexpectedly large interface spacing. Specular and non-specular rods of the clean Cu(001) surface were also measured and interpreted in terms of the relaxation of the first two layers.

5.2 Background

In common with the neighbouring 3d transition element iron, chromium can exist in several allotropes. Up to 1850°C the equilibrium phase is body centred cubic (bcc) with a lattice constant at room temperature $a_0=2.8839\text{\AA}$ (Wyckoff 1971). Above 1850°C it undergoes a martensitic transition to the face centred cubic (fcc) phase. Copper, on the other hand, is fcc at all temperatures. The lattice constant of copper $a_0=3.6150\text{\AA}$, however, means that the nearest neighbour separations: 2.4975\AA (bcc Cr)

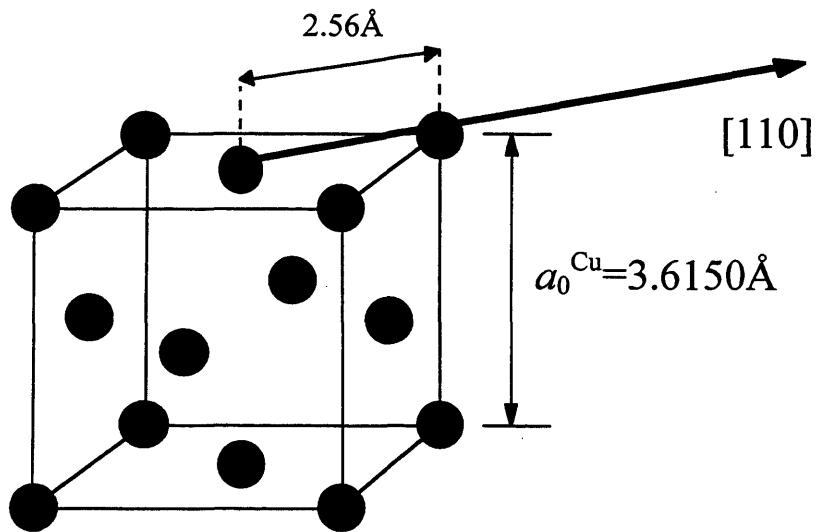
and 2.5562Å (fcc Cu) are nearly identical (figure 5.1). There is, therefore, the interesting possibility of stabilising the metastable fcc phase of chromium at room temperature by epitaxial strain in a thin film grown on a copper substrate. To achieve it, the interfacial energy must overcome the strain induced in the film and the energy increase due to the significantly higher surface free energy of chromium (2.006 Jm^{-2}) compared to that of copper (1.586 Jm^{-2}). It is now well established that iron, which has similar properties to chromium, can be stabilised in the fcc phase by growth on Cu(001) substrate (Prinz 1991). A discussion of the Fe on Cu(001) system is presented in chapter 7.

Since Cr has a half filled d band the valence electrons, and therefore the magnetic properties, will be sensitive to changes in environment and structure. A thin layer of Cr will have reduced symmetry and coordination as compared to the bulk so that the d band overlap will be modified which could lead to enhanced magnetism (see chapter 2).

There have already been several studies of the growth of Cr on Cu(001). Bader *et al* (1987b) observed break points in the Auger signal versus time curves which they interpreted as evidence of layer-by-layer growth. After deposition of 1ML (defined as a flat adsorbate layer with the same atomic density as the underlying Cu substrate i.e. $1.53 \times 10^{15} \text{ atoms cm}^{-2}$) at room temperature the LEED pattern indicated two orthogonal domains with 3×1 symmetry. The spots disappeared into a diffuse background for thicknesses greater than 3ML. Surface magneto-optic Kerr effect (SMOKE) measurements down to 115K showed no hysteresis loops characteristic of ferromagnetism.

Haugan *et al* (1994) confirmed that films initially show a 3×1 LEED pattern with $(1/3, 0)$ and $(2/3, 0)$ and conjugate spots missing. Following a suggestion by Wuttig *et al* (1993) for Fe/Cu(001) they attributed it to a mixture of fcc (001) and bcc (110) structures and the near coincidence of their diffraction patterns. Inverse photoemission measurements were attributed to a small and possibly vanishing magnetic splitting consistent with a paramagnetic state. This is in agreement with the total energy calculations which have predicted an fcc and paramagnetic Cr structure at the lattice constant of copper (Moruzzi and Marcus 1990).

fcc Cu



bcc Cr

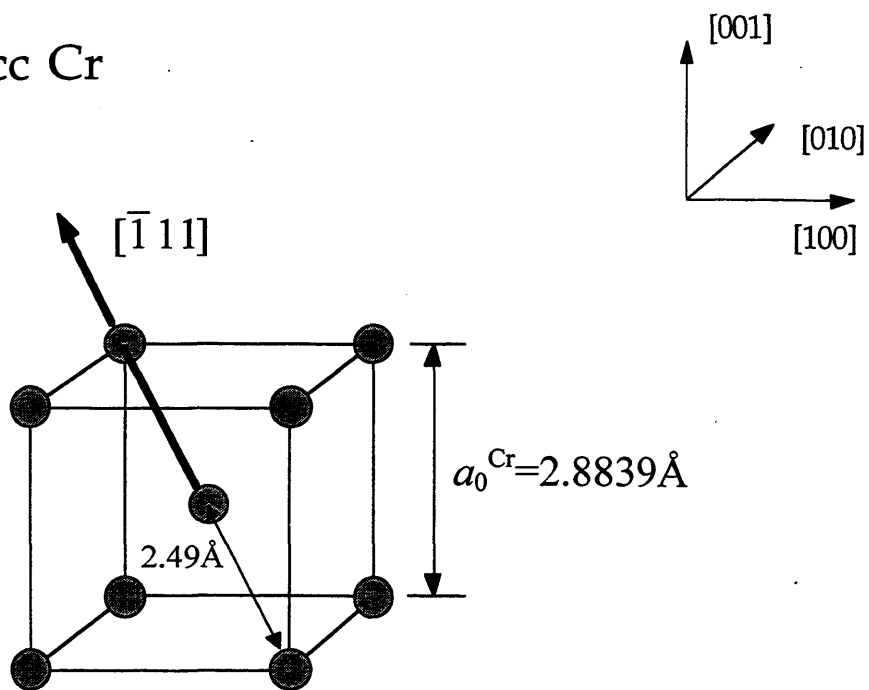


Figure 5.1. The unit cells of fcc Cu and bcc Cr showing the nearest neighbour distances in each case.

Rouyer *et al* (1994) studied the structure of Cr films grown at room temperature with a thickness between 6 and 30ML by LEED, X-ray photoelectron diffraction (XPD) and angle resolved ultraviolet photoelectron spectroscopy (ARUPS). They conclude that Cr forms epitaxial bcc microcrystallites in four equivalent domains each with the bcc(110) plane parallel to the (001) plane of the Cu fcc substrate. A later study (Rouyer *et al* 1995b) revealed a substantial distortion from the relaxed bcc structure in films less than 3ML thick caused by the interaction with the substrate. The strained domains produced a coincidence lattice with 3x1 periodicity. No evidence of surface segregation or intermixing was found.

A full dynamical LEED analysis of an annealed 11Å thick layer has been reported by Jandeleit *et al* (1994). It was shown that Cr retains its bulk bcc structure but that the top atomic layer is almost entirely Cu. Lawler *et al* (1996) studied the formation of Cr films in the temperature range 285-575 K. The growth was found to be three dimensional with irregular multilayer islands. They could not resolve the atomic sites on the islands although it was possible on the clean substrate. At low coverage two distinct island step heights were observed, one corresponding to the bulk Cr bcc (110) plane separation and the other to the fcc Cr(001) steps. At higher temperatures Cr forms more particulate features; annealing causes agglomeration.

While there is strong evidence that the equilibrium bcc phase develops for thicker films, the details of the growth, particularly the morphology of the film and the behaviour at the start or the growth is more controversial.

X-ray diffraction is now a well established tool for the study of surfaces and overlayer structures and has been extended to the study of epitaxial growth in real time (Norris 1993). The penetration of the X-ray beam into the film means that there is scattering from both the surface region and the bulk. The interference of the scattered waves from the surface and the bulk provides a sensitive measure of the atomic structure at the surface in particular the relaxations of layers normal to the surface. The growth of Cr on Cu(001) at several different substrate temperatures is described here. Three different coverages grown at room temperature have also been measured to give detailed information on how the structure of the films changes as a function of coverage.

5.3 Experimental Details

All of the measurements presented in this chapter were made with a wavelength of 0.9\AA . The copper crystal sample measured $8\times 8\times 1.5\text{ mm}^3$. It was cut and polished to within 0.4° of the (001) surface and mounted inside the ultra high vacuum environmental chamber coupled to the six circle diffractometer. The base pressure in the chamber was 8×10^{-11} mbar; it rose to 2×10^{-10} mbar during Cr evaporation. The coverage was subsequently confirmed using Rutherford Back Scattering (RBS). Typical deposition rates were 9 minutes per monolayer. One monolayer is defined as the real density of a single (001) plane of bulk Cu: 1.53×10^{15} atoms cm^{-2} .

The atomic arrangement of the surface and overlayer is described by a tetragonal unit cell defined by three orthogonal base vectors which are discussed in detail in chapter 4.

5.4 Results

5.4.1 Growth

Figure 5.2 shows the variation of the specularly reflected X-ray intensity with deposition time after the shutter on the vapour source was opened, for substrate temperatures between 100K and 473K. The X-ray signal was recorded at a grazing angle of 7.15° which corresponds to a momentum transfer with reciprocal lattice vector (001) of the fcc structure of Cu. With this geometry, which is shown schematically in figure 5.3, scattered waves from adjacent (001) planes are out of phase, which affords maximum sensitivity to the formation of monolayer islands (at the height of the bulk Cu(001) interlayer separation) as described in chapter 4.

All the plots show a rapid fall to a low value; only the plot recorded at 100K shows a slight maxima at a coverage of approximately 2ML. For perfect layer-by-layer growth, irrespective of the precise in-plane crystallographic arrangement, fcc or bcc,

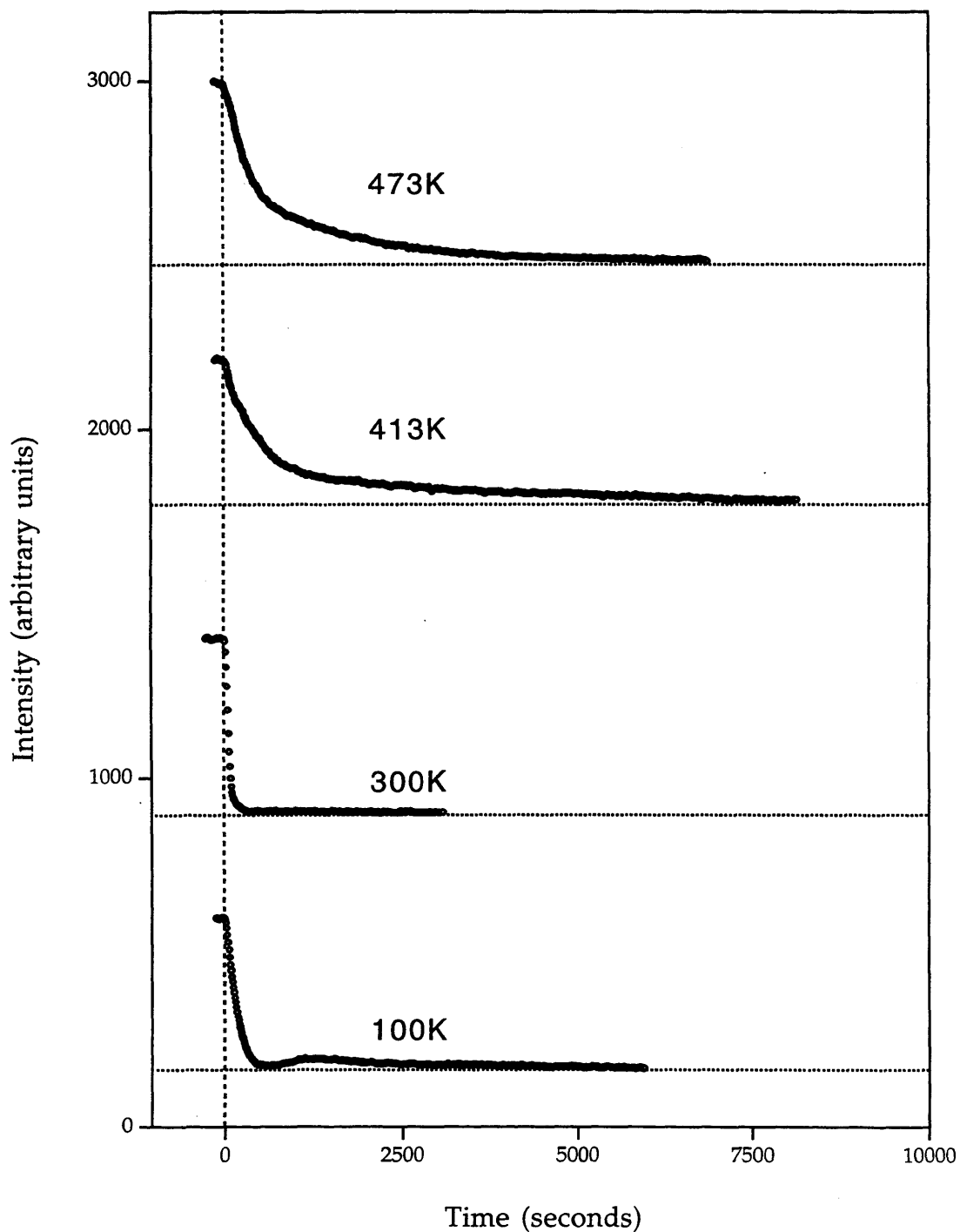


Figure 5.2. The variation of the specularly reflected X-ray intensity with deposition time for four different substrate temperatures. The intensity was recorded at the (001) point in reciprocal space. The plots are offset for clarity. The horizontal dotted lines show the zero intensity positions for each plot.

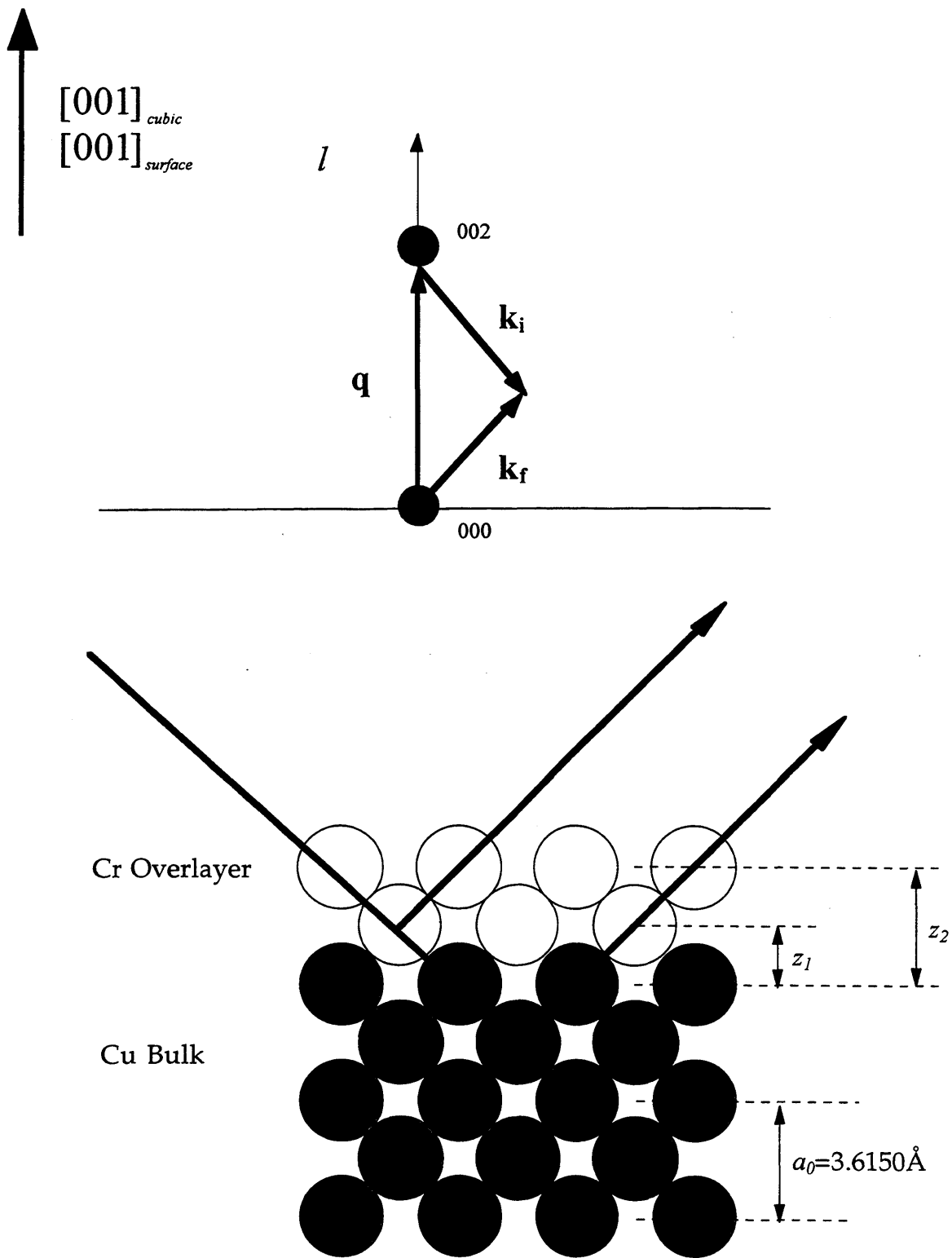


Figure 5.3. Schematic of the geometry used in measuring the (001) intensity during growth of Cr on Cu(001).

we would expect a series of oscillations with sharp cusps at the completion of successive layers (Vlieg et al 1988). The absence of such features indicates that the growth is multilayered, that is, new layers begin before existing ones are completed.

Figure 5.4 compares the measured results with two theoretical predictions: perfect layer-by-layer growth and the opposite extreme of random multilayer growth. The separation of the atoms is defined by the pseudomorphic packing of hard sphere radii. From this assumption the separation of Cr atoms is 1.72Å compared to the Cu separation of 1.81Å (see figure 5.12). In random multilayer growth surface diffusion is absent and the growth of the n^{th} layer is determined solely by the exposure of the preceding layer to incoming Cr atoms. Thus $d\theta_n/d\theta = \theta_{n-1} - \theta_n$ where θ_n is the coverage of the n^{th} layer and $\theta = \sum \theta_n$ is the total coverage. The occupancy of each layer θ_n is plotted in figure 5.5 as a function of total coverage for layer-by-layer and random growth up to a coverage of 2ML.

The variation of the reflected intensity is computed from the kinematic expression:

$$F_{001}^{total} = \frac{f^{Cu}}{1 - \exp(-\pi i l + a_3/2\mu)} + \sum_n \theta_n f^{Cr} \exp[2\pi i l z_n / a_3] \quad (5.1)$$

where f^{Cu} and f^{Cr} are the atomic form factors for Cu and Cr respectively and z_n is the height of the n^{th} layer above the surface ($n=0$) plane.

The first term corresponds to the unreconstructed Cu(001) bulk. Q is the momentum transfer. At $l=1.0$ scattered waves from alternate layers are out of phase and the first term, which is due to the perfectly truncated bulk, reduces to $1/2f^{Cu}$. The characteristic oscillations occur because successive Cr layers contribute alternating positive and negative contributions to the total amplitude. If Cr grows with the same atomic density and the same spacing as Cu(001) the structure factors at the completion of each Cr layer would be given by $1/2f^{Cu}-f^{Cr}$, $1/2f^{Cu}-f^{Cr}+f^{Cr}$, $1/2f^{Cu}-f^{Cr}+f^{Cr}-f^{Cr}$ etc.

If, to a first approximation, we equate the atomic form factor to the atomic number, the ratio of the intensity at the first peak at $n=1$ to the initial intensity (at

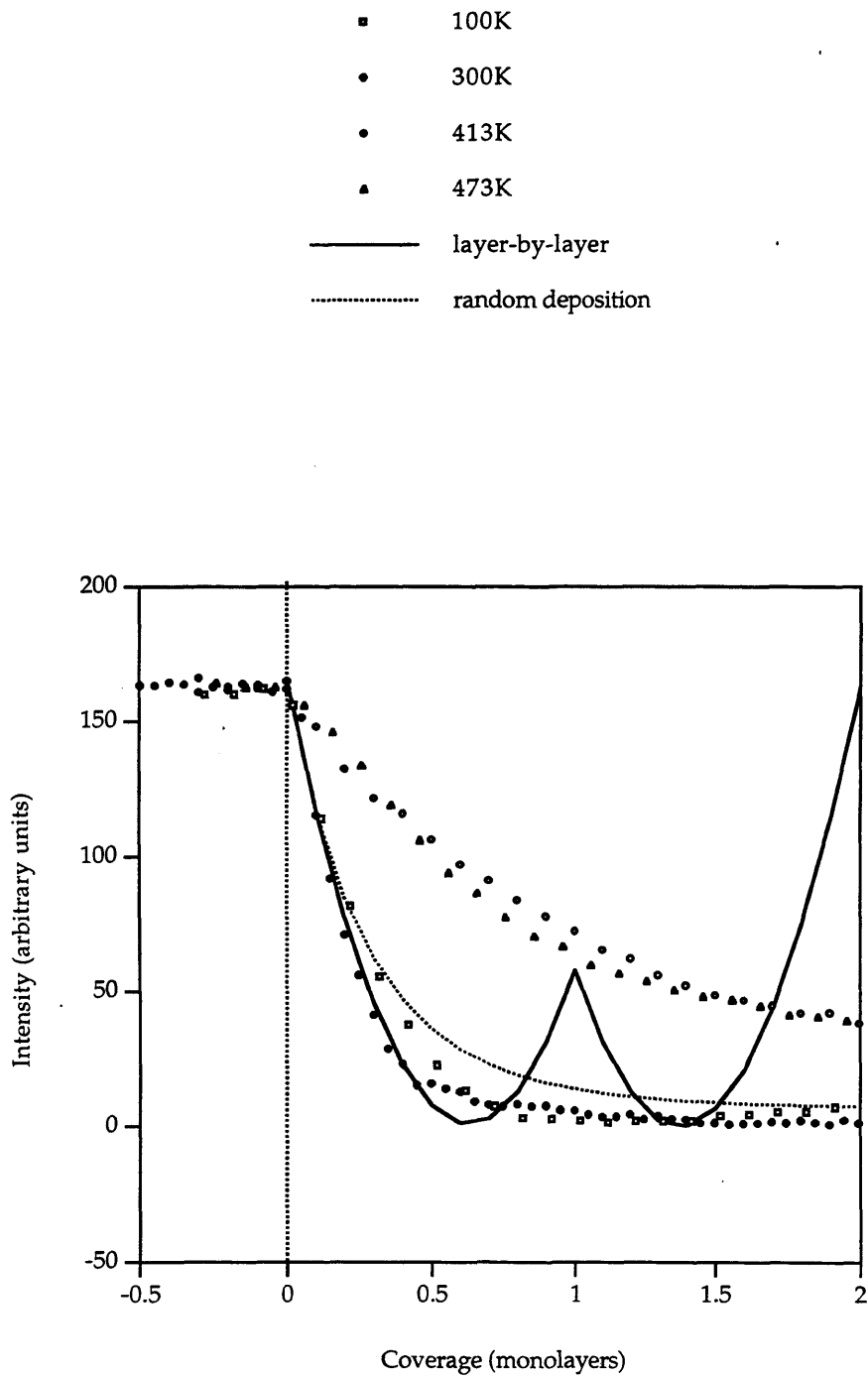


Figure 5.4. Comparison of the growth curves with the predictions for layer-by-layer growth and random deposition.

$n=0$) is expected to be 42%. Varying the atom density of the Cr layers and their separation would modify the precise shape of the intensity plot but a series of sharp cusps would still occur.

For the random growth mode the intensity, for the same assumptions can be expressed again by equation 5.1 but now θ_n is a decaying function, as shown in the lower diagram of figure 5.5, and N , the total number of layers, is a large number. Up to $\theta = 0.5$ $\theta_{n>1} \sim 0$ (see figure 5.5) and the predicted intensity is similar to that expected for the perfect layer-by-layer model. For higher coverages $\theta_{n>1}$ become more significant and the intensity rapidly approaches zero.

We note in figure 5.4 that the measured plots for the substrate temperature at 100K and 300K are well described by the random model to coverages up to (and beyond) 2ML. This indicates that at these temperatures surface diffusion and interlayer mass transport are restricted. By contrast the higher temperature curves are noticeably less steep, though they still fall away to a low value. This behaviour can be explained by an increased surface diffusion and the tendency to create 3D crystallites several layers high from the outset of growth.

It is concluded that, in spite of the good crystallographic matching with the Cu(001) substrate, it is not possible to stabilise the metastable fcc structure beyond perhaps the first layer at low temperature.

5.4.2 In-plane Scans

Specular reflection occurs with a momentum transfer normal to the surface and is therefore insensitive to the atomic arrangement within the surface plane. Figure 5.6a shows a scan along the $(h\ 1\ 0.2)$ axis in reciprocal space for different films grown at 300K. For the lowest coverages a peak corresponding to the $(1\ 0\ 0)$ CTR is evident at $h=0$. With increasing coverage (and roughness as indicated by the growth curve in figure 5.2) this feature weakens and at 7.1ML it is no longer evident. Two new peaks appear at $h=\pm 0.72$ along $(h\ 1\ 0.2)$. Peaks also appear at $k=\pm 0.72$ along the orthogonal $(1\ k\ 0.2)$ axis. The scan along the $(0\ k\ 0.2)$ axis shows only the $(0\ 1\ 0)$ CTR which again weakens with coverage (figure 5.6b).

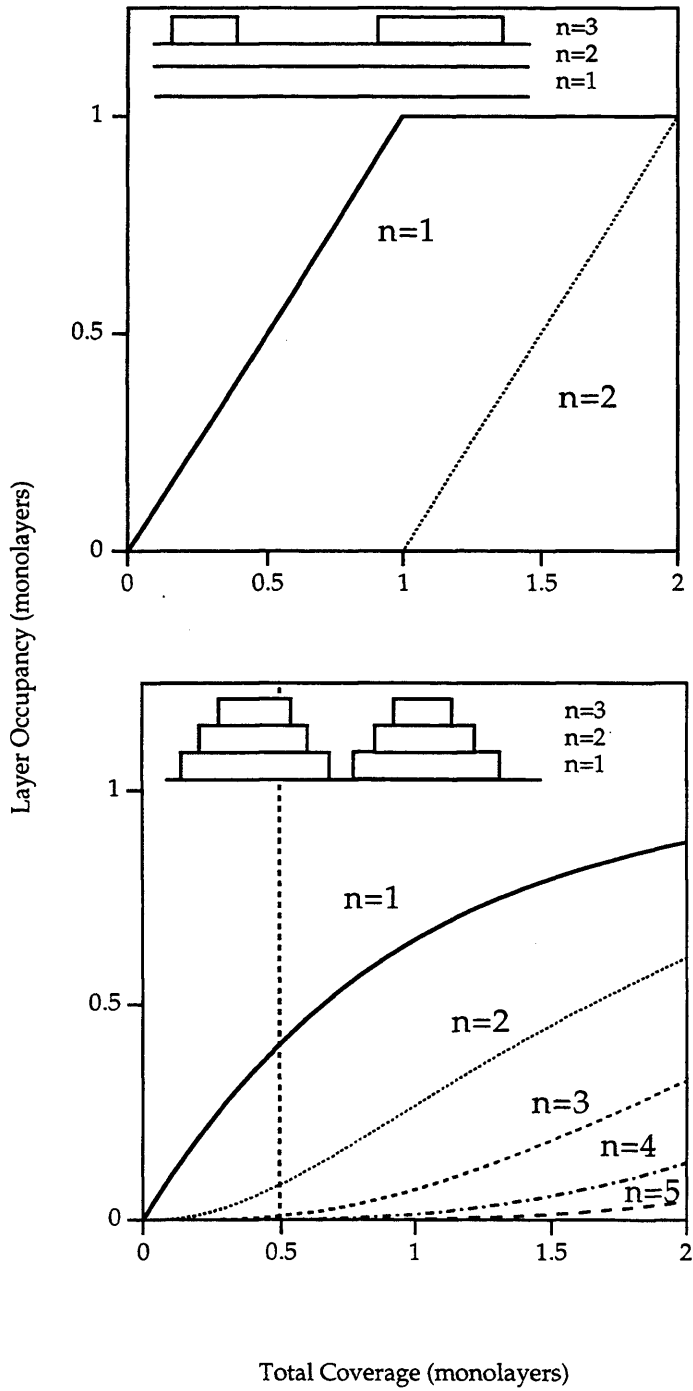


Figure 5.5. The variation of layer occupancies versus coverage for a layer-by-layer model (top) and a random deposition model (bottom).

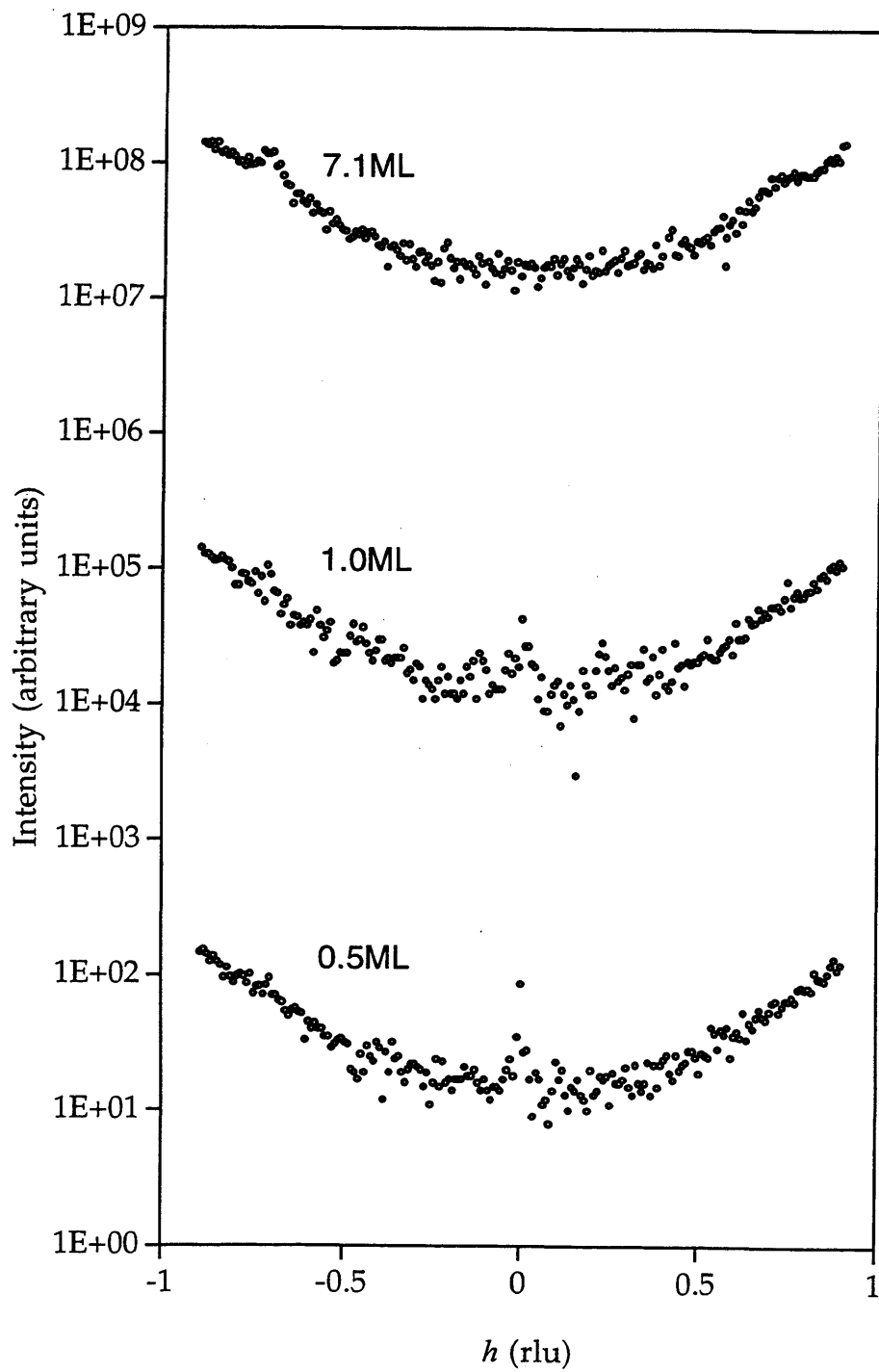


Figure 5.6a. In-plane scans along the h direction with $k=1$. h and k refer to the surface notation. The plots are offset vertically for clarity.

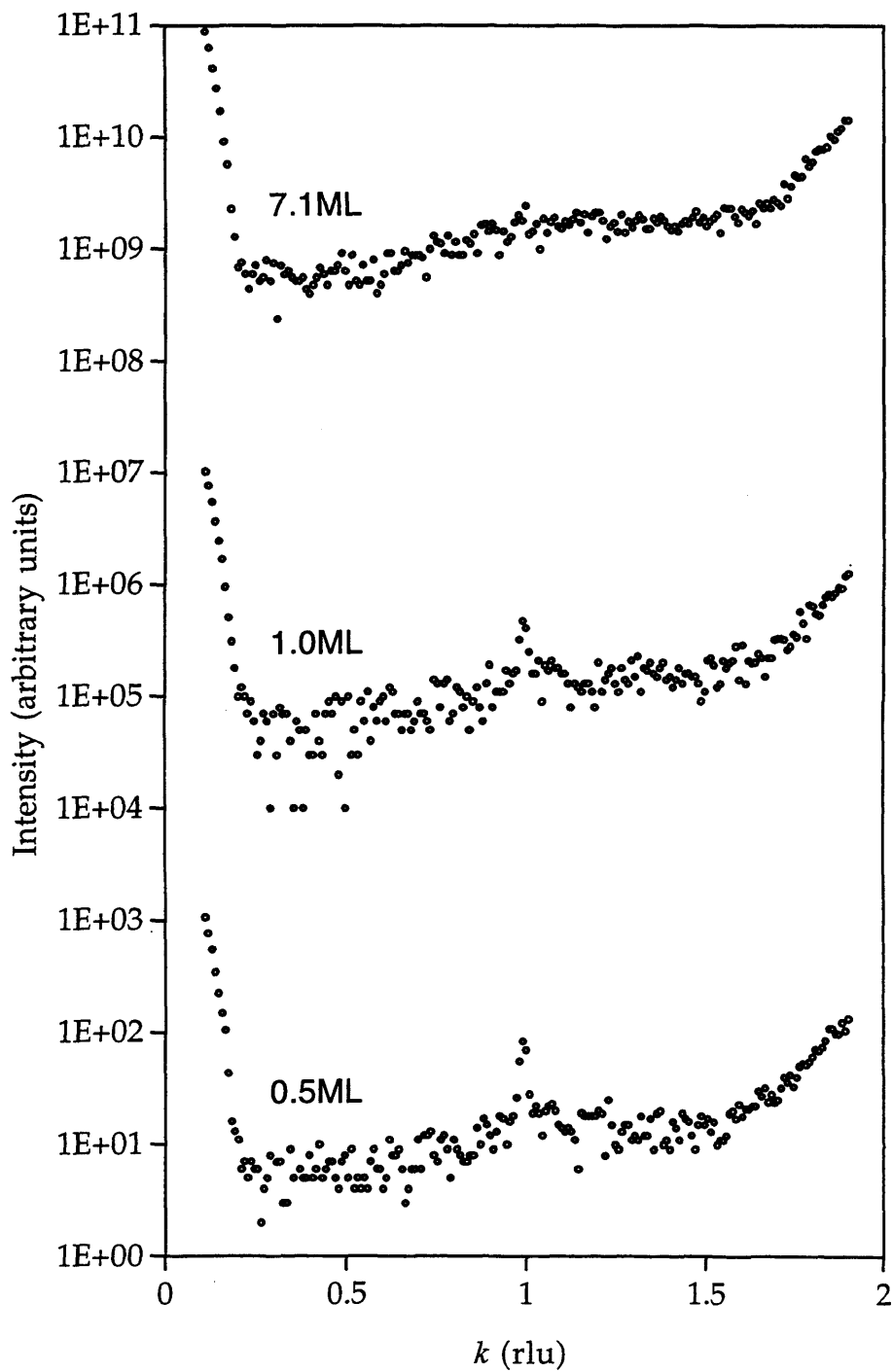


Figure 5.6b. In plane scans along the k direction with $h=0$. h and k refer to the surface notation. The plots are offset vertically for clarity.

A summary of the observed reflections is shown in figure 5.7. They confirm the growth of a bcc phase of Cr with the (110) plane aligned parallel to the (001) plane of the fcc Cu substrate. The (110) orientation of the bcc structure is expected since it is the most densely packed plane and it matches well onto the Cu(001) substrate with one of the $[\bar{1}11]$ axes aligned along the $[\bar{1}10]_{fcc}$ axis (see figure 5.8). The misfit along this axis for the completely relaxed bcc Cr structure is 2.4%. With this arrangement, indicated by II in the figure, the reciprocal lattice coordinated in the bcc geometry $h'k'l'$ convert to the coordinates of those of the surface of the fcc structure by

$$\begin{bmatrix} h \\ k \\ l \end{bmatrix}_{fcc} = \begin{bmatrix} 0.512 & -0.512 & -0.512 \\ -0.362 & 0.362 & -0.724 \\ 0.886 & 0.886 & 0.000 \end{bmatrix} \begin{bmatrix} h' \\ k' \\ l' \end{bmatrix}_{bcc} \quad (5.2)$$

Thus the $(1.02 \quad \bar{0.72} \quad 0.00)$ reflection is the $(1\bar{1}0)$ reflection of the bcc structure. The $(\bar{0.5} \quad 0.5 \quad 1.0)_{bcc}$ reflection would occur at $(1.02 \quad \bar{0.36} \quad 0.00)_{fcc}$ but are forbidden in the kinematical approximation. By contrast these are observed in LEED which is characterised by multiple scattering (Pendry 1974). The surface symmetry of Cu(001), $4mm$, implies there are four equivalent domain orientations I - IV indicated in figure 5.8. Figure 5.8 II shows a (110) layer with the $[\bar{1}11]_{bcc}$ axis of Cr aligned along the $[\bar{1}10]_{fcc}$ axis of Cu. With the Cr in its bcc relaxed phase with $a_0=2.884\text{\AA}$ the mismatch is small, the separation of Cr and Cu atoms (2.498 and 2.556 \AA) gives a misfit of 2.32%. The misfit of the $[\bar{1}1\bar{1}]_{bcc}$ rows with the Cu $[\bar{1}10]$ rows in the orthogonal direction is 8.5%.

Information on the film morphology parallel to the surface can be obtained by analysing one of the Cr in-plane peaks more closely. For an in-plane peak with a full width half maximum (fwhm) of Δq in reciprocal space the correlation length of the surface along the corresponding direction in real space is given by:

$$L = \frac{2}{\Delta q} \quad (5.3)$$

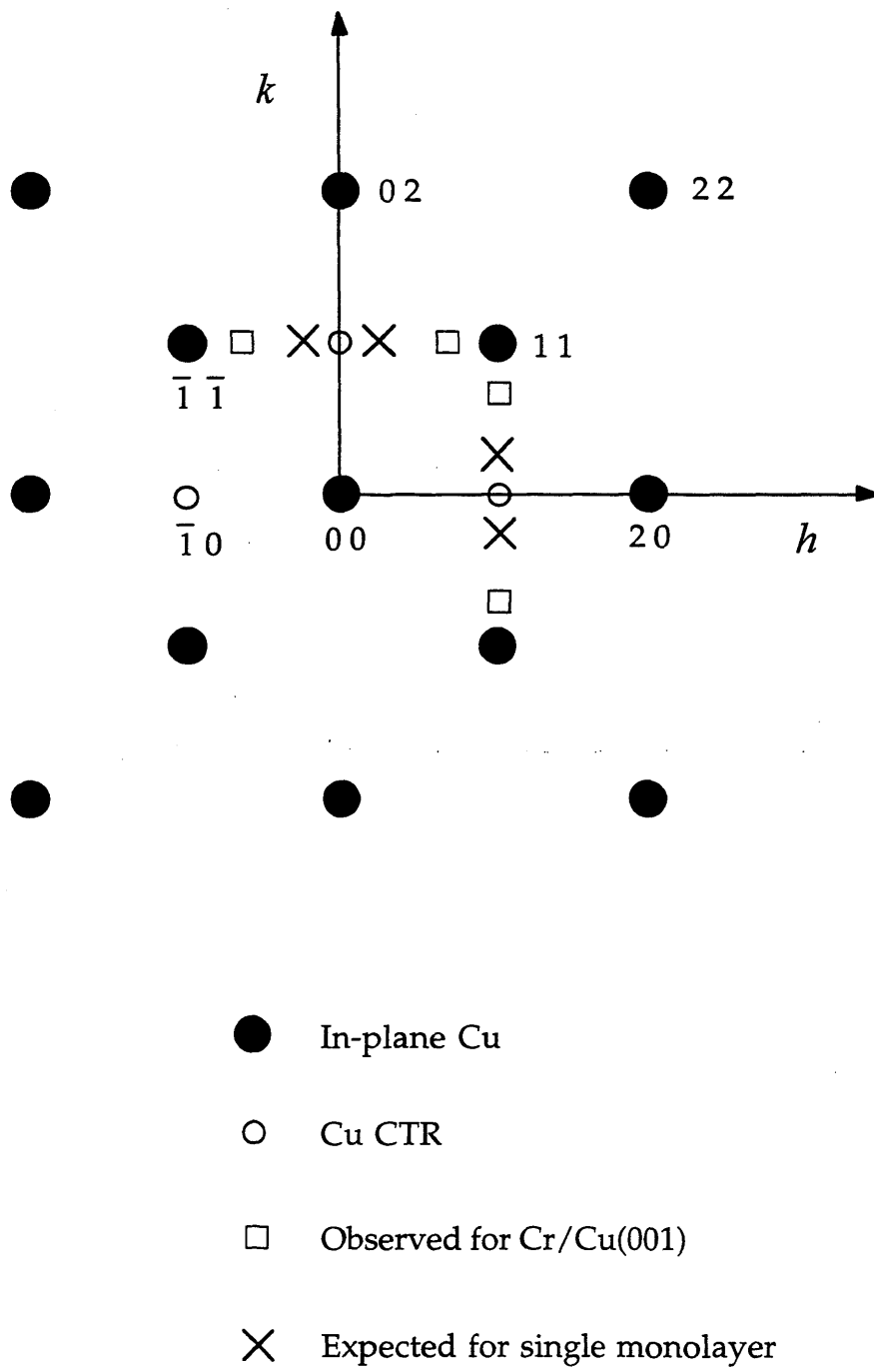


Figure 5.7. A schematic of reciprocal space at $l=0.2$ (in-plane position) showing reflections from bulk Cu and reflections seen for Cr/Cu(001). Also shown are the positions of peaks expected for a monolayer of Cr/Cu(001) with $(110)_{bcc}$ Cr parallel to $(001)_{fcc}$ Cu and $[\bar{1}11]_{bcc}$ Cr parallel to the $[110]_{fcc}$ or $[1\bar{1}0]_{fcc}$ axes of Cu. Miller indices are expressed in terms of the Cu fcc surface notation.

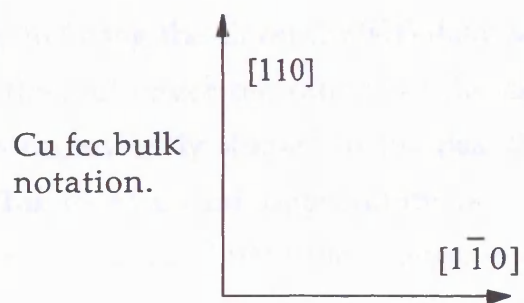
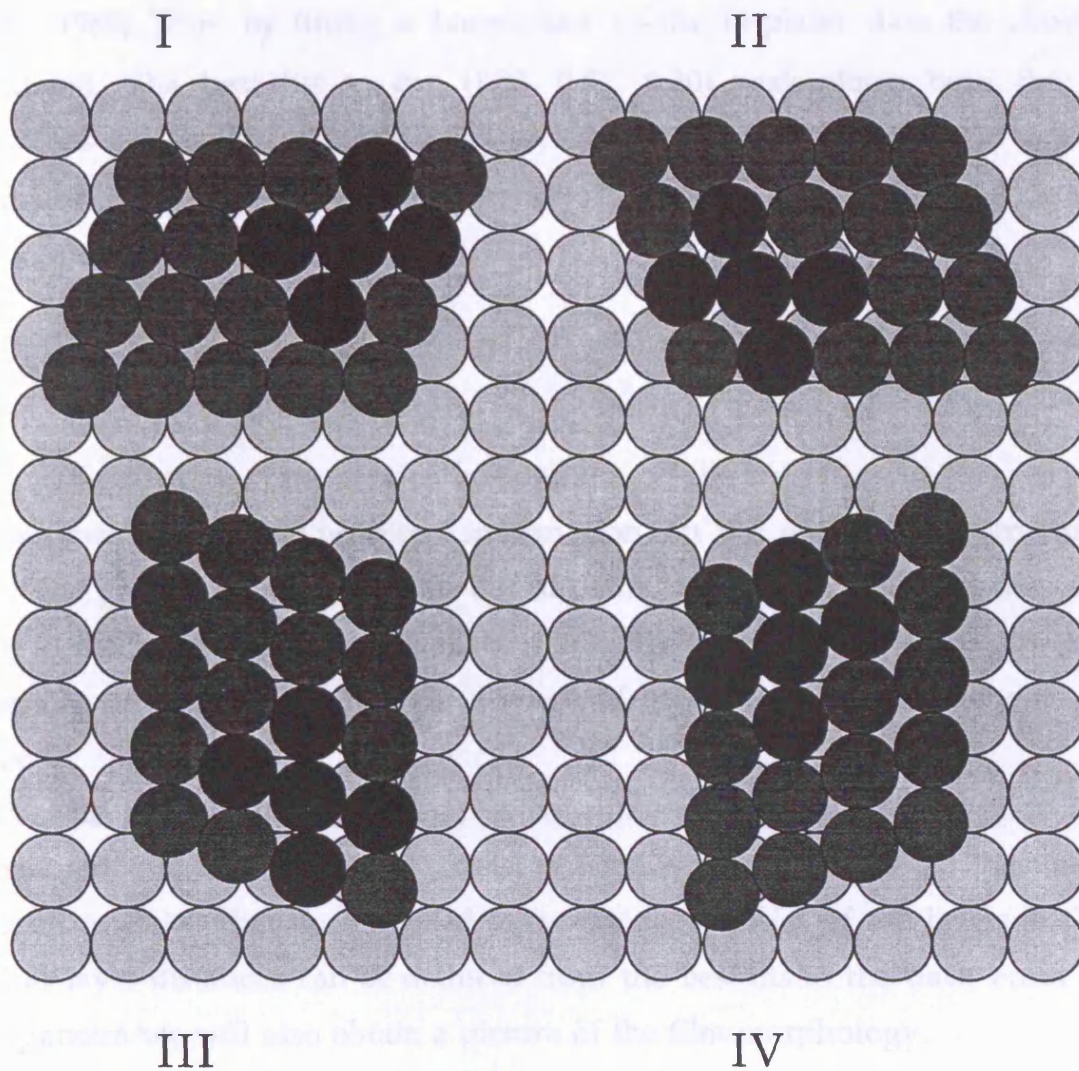


Figure 5.8. The four domains expected for Cr films growing with their *bcc* (110) planes parallel to the Cu(001) surface and with the close packed *bcc* $[\bar{1}11]$ axis aligned along either the close packed fcc $[110]$ or $[1\bar{1}0]$ axes. Domains II, III and IV are generated from I by the symmetry operations of the $4mm$ point group of the Cu(001) surface.

(Vlieg 1989) Thus by fitting a Lorentzian to the in-plane data the above can be calculated. The best fits to the (1.02 0.72 0.20) peak along both the h and k directions are shown in figure 5.9. They give fwhm values of 1.61×10^{-2} and 6.64×10^{-2} reciprocal lattice units which correspond to correlation lengths of 50.5 \AA , along h , and 12.3 \AA , along k , respectively.

5.4.3 Rod Scans

The in-plane scans give us information on the crystallographic axes parallel to the surface and give us no direct information on the out-of-plane structure of the film. The growth scans do give us out-of-plane information but since they were only done at one point in reciprocal space it is limited. Reflectivity scans give us a more complete picture as they include a range of measurements throughout reciprocal space.

The growth of the Cr film, as concluded from the growth scans, is clearly disordered. Since the films will consist of islands we cannot model the film as a flat layer. A model is therefore needed to fix the occupancies of the layers in the model so that layer distances can be deduced from the best fits to the data. From the layer occupancies we will also obtain a picture of the film morphology.

5.4.4 Rod Scans: The Clean Surface

Prior to fitting the Cr on Cu(001) data, scans along crystal truncation rods were used to fit the multilayer relaxations of the clean Cu(001) surface. The clean Cu(001) surface has been widely studied in the past the results of which are summarised in table 5.1. This gives us the opportunity of comparing our results with other work and confirming the validity of the analysis procedure.

When a crystal is cleaved, to form a surface, a charge redistribution and changes in atomic coordination occur. The charge redistribution causes the atoms to relocate themselves to a lower energy configuration. This could result in either a relaxation vertically to the surface plane or a rearrangement (reconstruction) within the plane. The (001) surfaces of fcc metals are close-packed surfaces so the charge

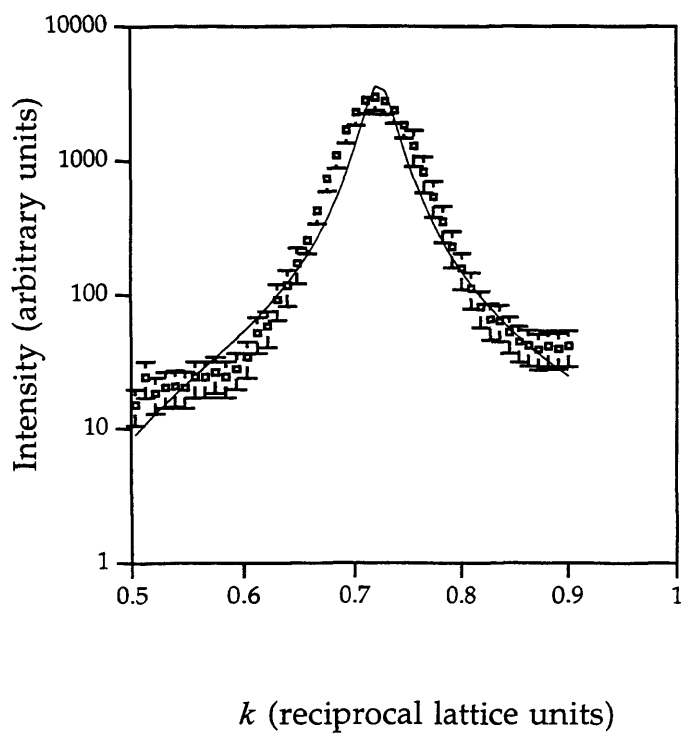
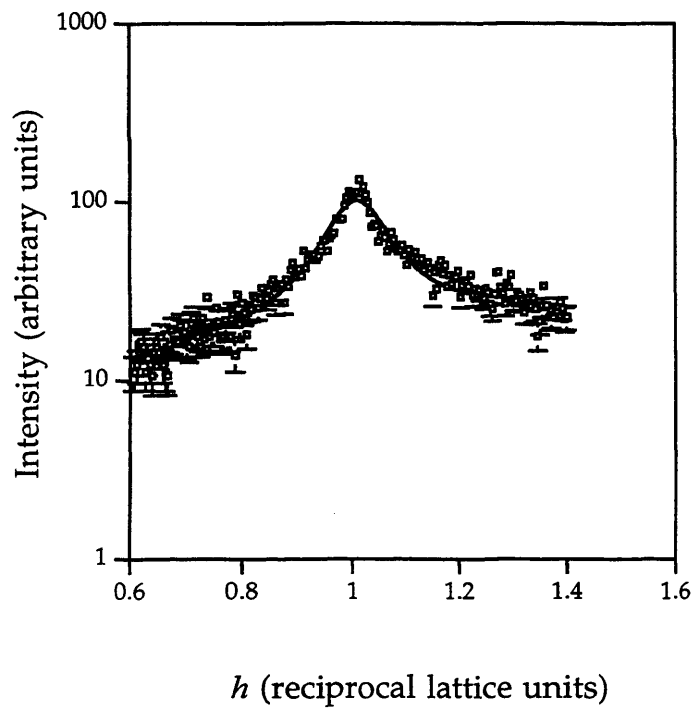


Figure 5.9. The in-plane (1 0.72) reflection shown with Lorentzian fits in both the h and k direction.

redistribution and subsequent atomic rearrangement of these surfaces are expected to be small. Early attempts to calculate the amount of relaxation were based on the change in atomic coordination only. Such attempts predicted that the distance between the two outermost layers d_{12} in a metal surface should be larger than the bulk value (Pendry 1974). This contradicted results from LEED experiments which predicted that d_{12} is usually smaller than in the bulk (Jona 1978). When the modification of the charge distribution was taken into account the above contradiction was, in principle, resolved. Using a model based on that of Smoluchowski (1941) where smoothing the electron density at the surface will lower the kinetic energy, Finnis and Heine (1974) formulated a model for relaxations in metals. They added that such a redistribution will give rise to an inward electrostatic force on the top layer nuclei thus correctly predicting the observed relaxations of the top layer towards the bulk.

Figure 5.10 shows the model used to fit the clean Cu(001) surface. The free parameters used in the fitting procedure were the displacements of the top two layers. These are shown in figure 5.10 in Å and as a percentage of the bulk Cu(001) interlayer spacing of 3.615Å. Figure 5.11 shows the (00 l), (11 l) and (10 l) crystal truncation rods plotted in the form of the structure factor versus perpendicular momentum transfer. The solid lines show the results of the best fit. Also shown are dotted lines which represent the theoretical results from a perfectly truncated Cu(001) surface. The difference between this and the best fits serves to highlight the sensitivity of the technique to small changes in displacement.

The best fit is consistent with a top layer relaxation towards the bulk of 1.25% accompanied by a relaxation of the next deepest layer outwards by 0.19%. Including any other layers as fit parameters did not significantly improve the quality of the fit. These results give justification for allowing the top two layers to be varied in the analysis. This represents oscillatory multilayer relaxations that decay rapidly with the depth below the surface. Oscillatory behaviour is favoured by all but one of the results shown in table 5.1 but only work by Lind *et al* (1987) and James *et al* (1995) compare with the magnitudes obtained from our analysis. Robinson's beta model (Robinson 1986) was used to model the roughness. The best fit yielded a χ^2 of 1.42 and a β value of 0.05 corresponding to a root mean square roughness of 0.43Å.

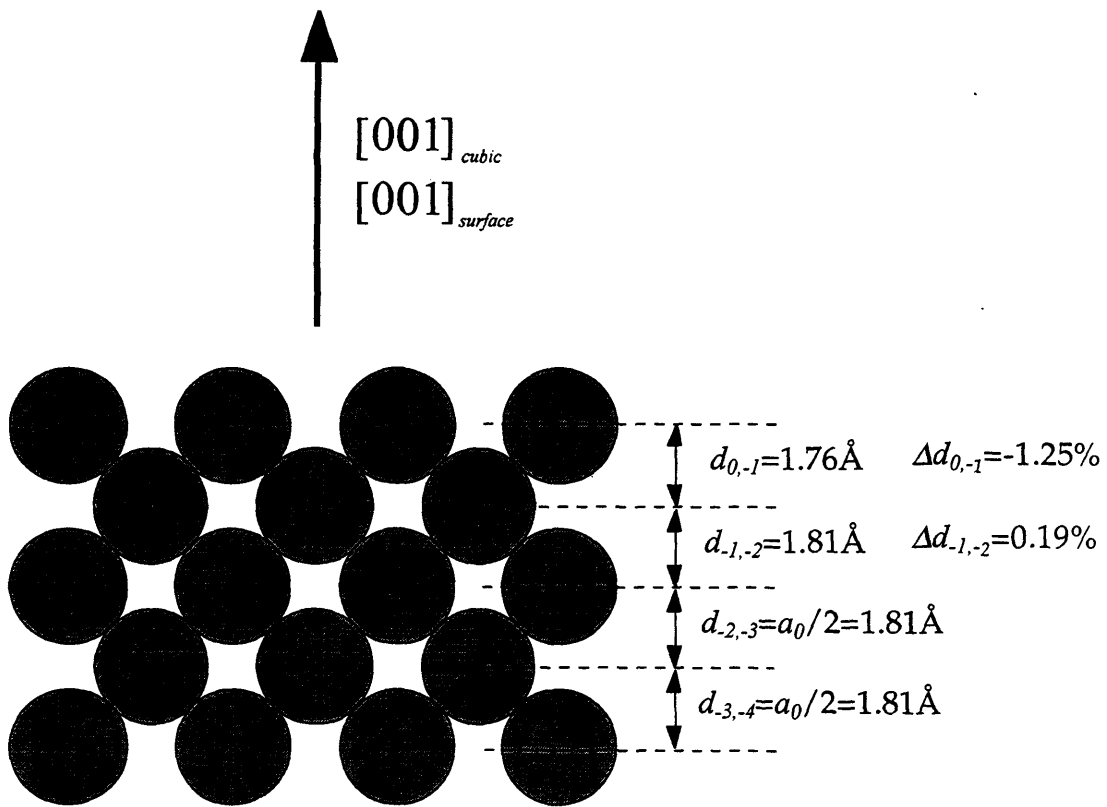


Figure 5.10. Schematic of the model used to fit the clean Cu(001) surface.

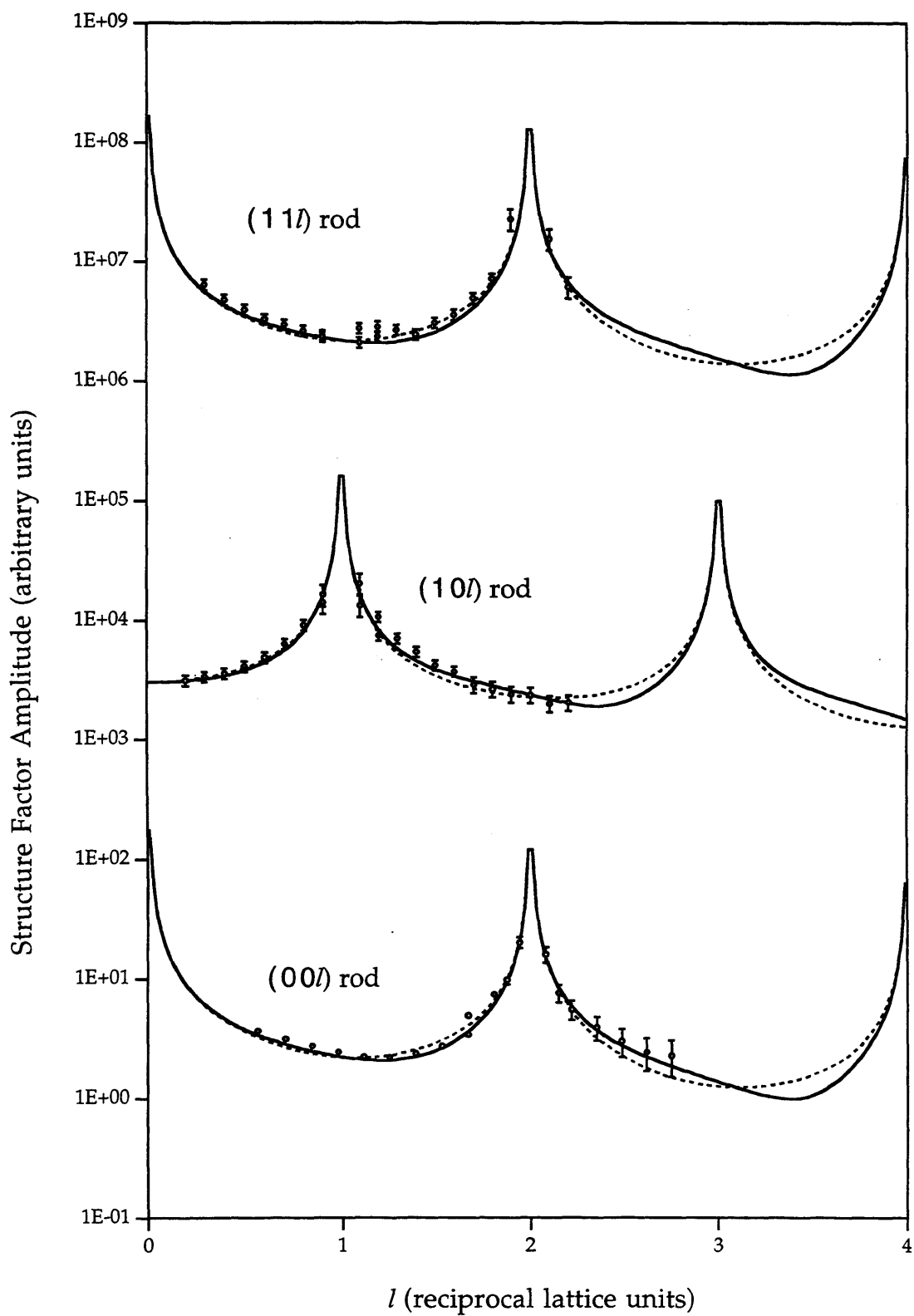


Figure 5.11. The (00l), (11l) and (10l) rods for the clean Cu(001) surface. Also shown are the results of the best fits (solid lines) and the predictions of a non relaxed surface (dashed lines).

Authors	Technique	Δd_{12} (%)	Δd_{23} (%)	Δd_{34} (%)
Noonan and Davis (1982,1983)	LEED I-V	-1.1±0.4	+1.7±0.6	+1±2
Abu-Joudeh <i>et al</i> (1986)	LEED	-2	+1.5	
Alkemade <i>et al</i> (1986)	MEIS	-2±2		
Lind <i>et al</i> (1987)	SPLEED	-1.2	+0.9	
Jiang <i>et al</i> (1991)	MEIS	-2.4±0.8	+1.0±1.0	
Mizuno <i>et al</i> (1993)	LEED	-0.2	-0.2	
Folies <i>et al</i> (1986)	Theory	-1.4	-0.3	
James <i>et al</i> (1995)	SXRD	-1.55±0.5	+0.13±0.4	
Steadman <i>et al</i> (1997)	SXRD	-1.25±0.4	+0.19±0.4	

Table 5.1. Summary of previous studies of Cu(001) relaxations. The values are given as percentages of the bulk lattice parameter of 3.615Å.

5.4.5 Rod Scans: Cr on Cu(001)

Since we know that the overlayers are rough, from the growth curves, we have a multilayer system that cannot be modelled as a flat layer. Even in the case of a submonolayer coverage a model used to fit this will have several layers where interlayer distances and occupancies can vary. This may mean that we have a system with too many fit parameters. To reduce the number of parameters, a suitable model is needed to fix the layer occupancies. This enables us to find interlayer distances from the best fits.

Two different coverages were grown with the substrate held at room temperature. From Rutherford Back Scattering analysis they were found to correspond to 0.5±0.05 and 1.0±0.05 monolayer equivalents of Cu(001).

Figure 5.12 shows the model used for fitting the films. This consists of several Cr layers on top of a Cu(001) substrate. The displacements of all the Cr layers and the

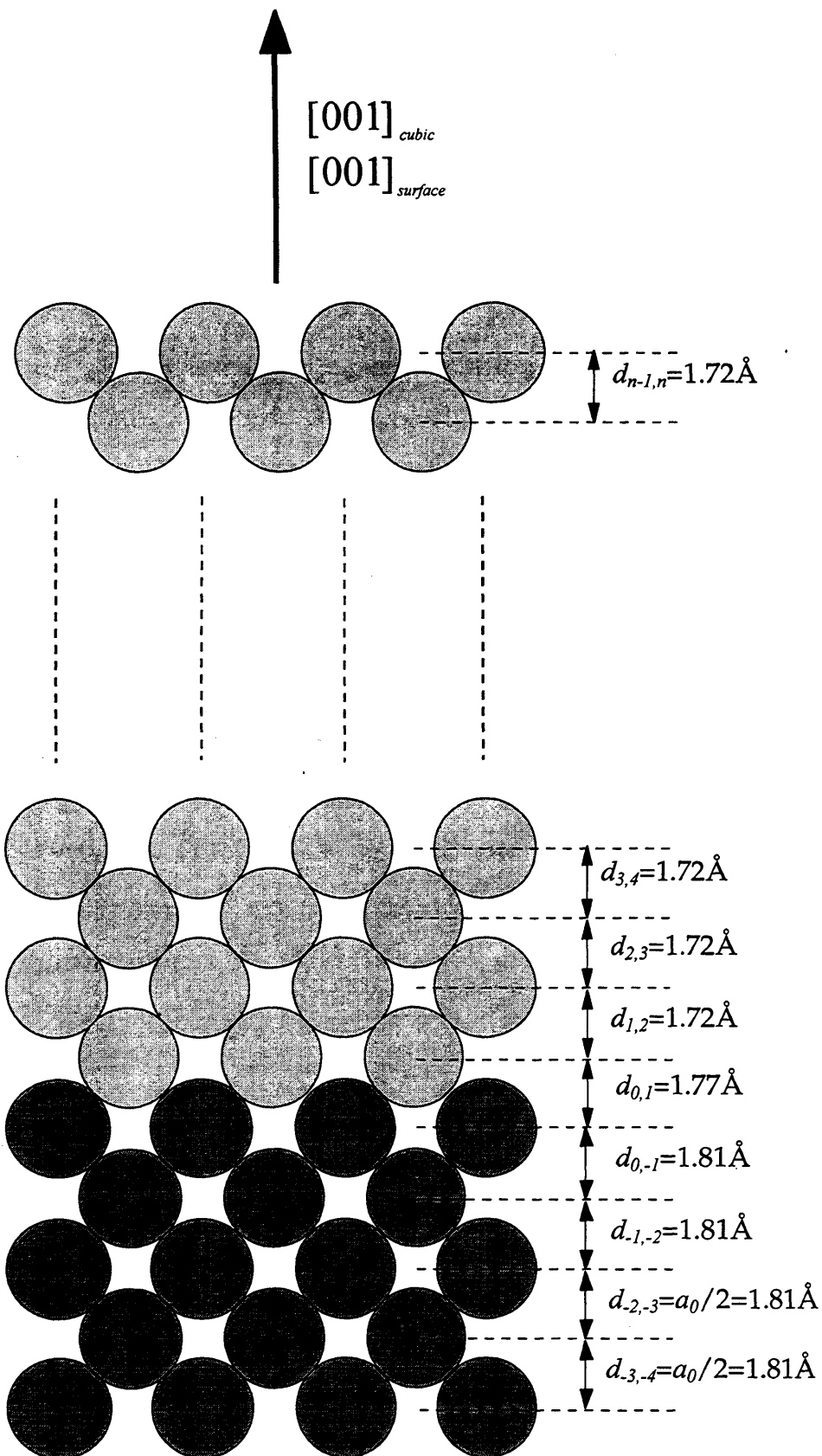


Figure 5.12. Schematic of the model used to fit Cr on Cu(001). The interlayer distances shown correspond to those calculated from the hard sphere radii of the two atomic species (1.25\AA and 1.28\AA for Cr and Cu respectively).

top two Cu layers can be allowed to vary. The occupancies of the Cr(001) layers were also allowed to vary so that the islanding of the Cr overlayer could be simulated.

Four standard models, used for describing interface structures, have been used to model the layer occupancies of the film: Robinson's beta roughness model (Robinson 1986), a Poisson model, a linear model and a sinusoidal model. In Robinson's model layer j has an occupancy of α^j . In the continuous model of Stearns (1989), where the average position of the interface is $z=0$, the width of the interface σ is calculated by taking the second moment of the differential of the profile function $p(z)$ describing the occupation of layers.

$$\sigma^2 = \int z^2 \frac{dp(z)}{dz} dz \quad (5.4)$$

This model, however, is not satisfactory for describing our data since we are only dealing with a few atomic layers. Instead we use a discrete version of the above which has previously been used by Lohmeier *et al* (1994) to describe the interface between an amorphous Si layer and Si(001). Here the average position of the interface $\langle z \rangle$ and rms roughness σ , for a profile function $\theta_j(\alpha)$, where j is the layer number and z_j is the height of layer j , are defined by:

$$\langle z \rangle = \sum_{j=1}^{\infty} z_j (\theta_j(\alpha) - \theta_{j+1}(\alpha)) \quad (5.5)$$

$$\sigma = \left(\sum_{j=1}^{\infty} (z_j - \langle z \rangle)^2 (\theta_j(\alpha) - \theta_{j+1}(\alpha)) \right)^{1/2} \quad (5.6)$$

Simplified versions of equations (5.5) and (5.6) are listed in table 5.2 next to their corresponding profile functions for overlayers that have identical interlayer spacings d between all of the layers. If the spacings are not identical then the formulae given above for $\langle z \rangle$ and σ have to be worked out explicitly. The fitting parameter used in

each model is also given in the table. The value of the width is used directly as a fitting parameter in the linear and sinusoidal profiles.

Description	θ_j	$\langle z \rangle$	σ
Robinson's	α^j	$\frac{\alpha}{1-\alpha}d$	$\frac{\sqrt{\alpha}}{1-\alpha}d$
Poisson	$1 - \sum_{j=0}^{j-1} \frac{\alpha^j}{j!} \exp(-\alpha)$	αd	$\sqrt{\alpha}d$
Linear	$1 - \frac{j}{2\sqrt{3}\alpha}$ $j \leq 2\sqrt{3}\alpha$ 0 $j > 2\sqrt{3}\alpha$	$\sqrt{3}\alpha d$	αd
Sinusoidal	$1 - \frac{1}{2} \cos\left(\frac{\pi j}{2a\alpha}\right)$ $j \leq 2a\alpha$ 0 $j > 2a\alpha$	$a\alpha d$	αd

Table 5.2. Useful profile functions with their corresponding average interface positions $\langle j \rangle$ and roughnesses σ . The constant $a = \pi/\sqrt{\pi^2 - 8}$.

The four profiles were used to calculate the occupancy of each layer. Since the Robinson beta and Poisson model occupancies continue to infinity with j the number of layers used in the model was carefully chosen so that using any more would have a negligible effect on the quality of the fits. Following this the occupancies were all normalised, i.e. all multiplied by the same factor, so that the total occupancy accorded with the coverage found from RBS.

Several different fitting procedures were tried for both coverages. Initially, only the parameter α was used. Following this the displacements of the Cr layers which had a high enough occupancy to have an effect on the quality of the fit were allowed to vary. Finally the top two copper layer displacements were also used as

free parameters. Before fitting commenced the displacements were set at values corresponding to Cr atoms fitting into the four fold hollow sites of the Cu(001) surface assuming the hard sphere radii of both atomic species (1.278Å and 1.248Å for Cu and Cr respectively). Putting the Cr atoms into these sites is justified because the reflectivity is only sensitive to the out-of-plane structure of the film. To allow for the fact that the Cr film may modify the underlying Cu surface the procedure involving only α as a parameter and that involving both α and the layer displacements two models were fitted: one with no Cu multilayer relaxations and another with the Cu multilayer relaxations found from the fits to the clean surface data. Another procedure allowed the Cu displacements to vary in addition to the above.

The results for the best fits to the (00l) rod are summarised in tables 5.3 and 5.4. The best fits are also shown with their corresponding rod data in figures 5.13 and 5.14. Also shown is the prediction for a flat 0.5ML film and a flat 1.0ML film. For the 1.0ML data the prediction for an overlayer with the same α value as the best fit but with interlayer spacings determined by the hard sphere radii of the atoms is also shown.

Variable Parameters	Beta Model		Poisson Model		Linear Model		Sinusoidal Model	
	σ (Å)	χ^2	σ (Å)	χ^2	σ (Å)	χ^2	σ (Å)	χ^2
α	1.8±0.4	2.55	1.7±0.5	2.41	1.2±0.7	3.16	1.2±0.5	3.16
α^*	2.4±0.5	7.82	1.4±0.6	7.91	1.4±0.7	8.07	1.4±0.5	8.12
$\alpha, \Delta d_{Cr}$	1.4±0.2	2.34	1.6±0.3	1.81	1.2±0.5	2.94	1.0±1.2	2.82
$\alpha, \Delta d_{Cr}^*$	1.4±0.3	1.86	1.4±0.3	1.84	3.1±0.3	2.64	2.9±1.2	2.86
$\alpha, \Delta d_{Cr}, \Delta d_{Cu}$	1.4±0.3	1.88	1.3±0.7	1.78	1.0±1.0	2.42	0.9±1.0	2.43

Table 5.3. Best fit results to the (00l) rod for the 0.5 ML film. . The * indicates that the Cu distances were fixed at the values found from the fit to the clean data.

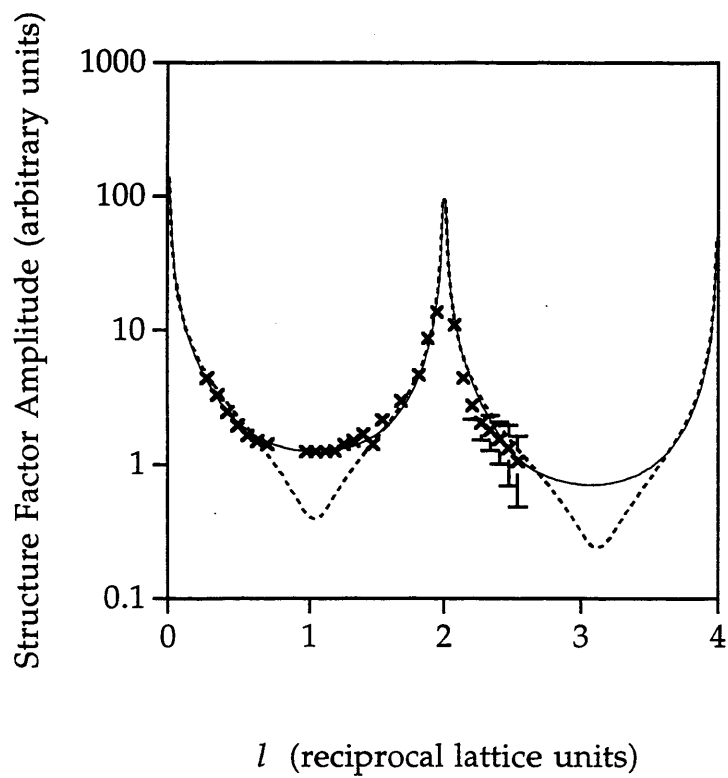


Figure 5.13. The (00 l) rod for 0.5 monolayers of Cr on Cu(001). Also shown are the best fit (solid line) and the prediction for a flat 0.5 monolayer film (dashed line).

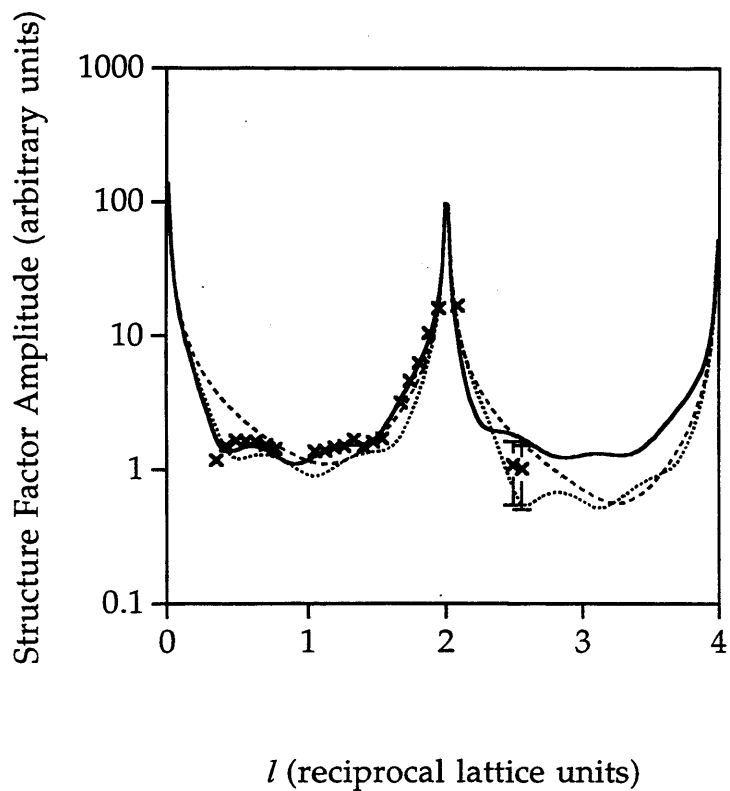


Figure 5.14. The (001) rod for 1.0 monolayer of Cr on Cu (001). Also shown are the best fit (solid line) and two predictions: one for a film with the same layer occupancies as the best fit but with layers displacements determined from hard sphere radii (dotted line) and another for a flat Cr monolayer (dashed line).

It is clear, by looking at the best fit results for the 0.5ML coverage in table 5.3, that the χ^2 is not improved significantly by including any more fit parameters than α . If α is the only parameter used the best fits are obtained if the substrate is bulk terminated rather than using the relaxations found for the clean surface. All four models are equal in describing the morphology of the films.

Variable Parameters	Beta Model		Poisson Model		Linear Model		Sinusoidal Model	
	σ (Å)	χ^2	σ (Å)	χ^2	σ (Å)	χ^2	σ (Å)	χ^2
α	4.8±1.0	7.98	2.7±0.3	5.86	2.1±0.3	5.09	1.5±0.5	3.27
α^*	7.7±1.8	10.20	2.8±0.3	8.49	2.1±0.3	7.91	1.5±0.5	5.77
$\alpha, \Delta d_{Cr}$	2.4±0.5	6.77	2.3±0.2	3.88	1.9±0.5	2.06	1.5±0.3	2.65
$\alpha, \Delta d_{Cr}^*$	3.3±0.6	5.26	2.3±0.2	3.87	1.9±0.5	2.32	1.5±0.3	3.17
$\alpha, \Delta d_{Cr}, \Delta d_{Cu}$	2.4±0.5	5.46	2.7±0.2	3.01	2.1±0.5	1.58	1.5±0.3	2.05

Table 5.4. Best fit results to the (00l) rod for the 1.0 ML film. The * indicates that the Cu distances were fixed at the values found from the fit to the clean data.

The 1.0 monolayer coverage is different. To begin with there is now a large decrease in the χ^2 of the fit when the interlayer displacements of the Cr layers are included as a fit parameter with the roughness parameter. However, including the Cu layers as additional parameters does not have a large enough effect. For Robinson's model the agreement is greatly improved with the Cu relaxations; for the other models there is no improvement if we include the Cu multilayer relaxations. The best fit is obtained using the linear model. The results for this best fit are shown in table 5.5. The displacements shown in this table represent the departure of the interlayer spacings from the ideal packing of hard sphere radii. The corresponding root mean square value of the roughness calculated from the formula above is 2.1Å.

Layer	Occupancy	$\Delta d(\text{\AA})$	$\Delta z(\text{\AA})$
1	0.51	0.35 ± 0.09	0.35 ± 0.09
2	0.33	0.07 ± 0.16	0.42 ± 0.16
3	0.16	0.10 ± 0.29	0.52 ± 0.29

Table 5.5. Best fit result to the (00l) rod for the 1.0 ML film.

5.5 Discussion

The results of scanning the growth *in-situ* offer convincing evidence for a disordered three dimensional growth mode. There is no evidence of the metastable fcc phase that might be expected from consideration of the atomic diameters and high temperature phase diagram of Cr. Such disorder may be due to the difference in surface free energies of the substrate and adsorbate atoms (1.556 and 2.006 mJ/m² respectively). As a result, in favour of energy considerations, the growth may proceed by keeping much of the substrate surface uncovered. This is in agreement with most of the previous work but contrasts with the work by Bader *et al* (1987b) where a layer-by-layer model was determined. Covering of Cr structures by Cu substrate atoms cannot be ruled out since this would also be energetically favourable.

The in-plane scans of the 0.5, 1.0 and 7.1ML films show a clear change in the structure of the films as a function of coverage. Only the CTRs are noticeable at 0.5 ML. No 3x1 peaks seen by Rouyer *et al* (1995b) for coverages of less than 2ML are visible. A possible explanation is that Cr atoms are primarily resting in four fold hollow sites on the Cu surface. At 1.0ML the CTRs have visibly attenuated and peaks at $(1 \pm 0.72 \ 0.2)$ and $(\pm 0.72 \ 1 \ 0.2)$ may be starting to form. By 7.1ML the CTRs have disappeared almost totally. This effect will be due to the roughness since a rough surface will cause a greater fall off of intensity along the rods away from the Bragg peaks. In contrast to this the peaks at $(1 \pm 0.72 \ 0.2)$ and $(\pm 0.72 \ 1 \ 0.2)$ are becoming stronger. If a Cr film is growing in its bcc phase with its (110) axis parallel to the (001)

axis of the substrate and its $[\bar{1}11]$ axis parallel to the in-plane $[\bar{1}10]$ axis of the substrate then peaks will occur at in-plane positions of $(1 \pm 0.72 \ 0)$ and $(\pm 0.72 \ 1 \ 0)$.

The correlation lengths of 50.5 and 12.3Å along h and k respectively compare well with the island sizes of 150 to 20Å found by Lawler *et al* (1996). The anisotropy in the correlation length may be due to the step density on the surface. Islands may preferentially line up with the edges of each terrace. A problem with the calculated correlation lengths is that the $(1 \ 0.72)$ reflection in the k direction resembles a gaussian rather than a lorentzian curve. There may, therefore, be a significant error in the length calculated in this direction.

All of the roughness models provide adequate fits to the 0.5ML coverage. The rms values corresponding to the fit parameters for the best fits for each model i.e. α equal to 0.4 ± 0.2 , 1.0 ± 0.6 , 0.7 ± 0.4 and 0.8 ± 0.3 , are 1.8 ± 0.8 , 1.7 ± 0.8 , 1.2 ± 0.7 and 1.4 ± 0.5 Å respectively. These values are quite close to each other. At this low coverage we may only be sensitive to the spread of the atomic positions in the overlayer rather than the particular model describing the roughness.

For the 1.0ML coverage the linear model gives the best fit if the displacements in the film are allowed to vary. However, if α is the only parameter allowed to vary the sinusoidal model gives a better fit. Whatever fitting procedure we adopt the linear and sinusoidal models always give a better fit than the beta and Poisson models. In the case of the beta and Poisson models more layers will contribute to the roughness. Both are described by mathematical functions which tail off to infinity. In contrast to this the sinusoidal and linear models have an abrupt cut off which depends on their rms roughness values. The fit to the 1.0ML data therefore indicates that only a few layers are dominant i.e. only a few layers contribute to the roughness of the overlayer. It is possible that the roughness of the Cu(001) surface will contribute to the roughness of the overlayer. The fits to the clean data, however, indicate that the Cu surface is quite flat. Most of the roughness we are modelling will, therefore, only be due to the overlayer structure.

Since the $(00l)$ rod is only sensitive to the out-of-plane structure the in-plane structure we assume is not important. From the in-plane data for the lower coverages we have assumed that the Cr atoms sit in four fold hollow sites on the

Cu(001) surface. The best fit to the 1.0ML data is consistent with a large interface expansion compared to that calculated from the packing of hard spheres. There may be expansions in the interlayer spacings of the film although the errors here are quite large. The comparison of this best fit model to the predicted fcc phase of Cr on Cu(001) gives similar results. By using the hard sphere radius of a Cr atom (1.30\AA) in its fcc form ($a_0=3.68\text{\AA}$) the interlayer spacings can be predicted. Comparing the best fit results with the fcc model still yields an expansion at the interface. The other displacements are the same within the range of the errors. From the best fit, therefore, we cannot distinguish between the two models. The only difference between them is the assumed hard sphere radius which is either calculated from the bcc or fcc phase of Cr. However, we do have a definite expansion at the interface whichever case we assume. If the overlayer is ferromagnetic, which is predicted for an fcc lattice, the majority Cr d bands will be completely occupied whilst the minority d bands will be nearly empty. As a result there will be as many d bonding states occupied as d antibonding states so that d cohesion becomes less important. The atoms in the first layer will therefore not be that tightly bound to the Cu surface resulting in a large distance at the interface. However, such a structure would be expected to have an increased magnetic moment compared to that of the bulk (see chapter 2). The inverse photoemission results of Haugan *et al* (1994), however, failed to find any significant magnetic splitting for their monolayer structure of Cr on Cu(001) which would be expected for a film with increased magnetic moments. Moreover, Bader *et al* (1987) found no evidence for ferromagnetism in their Cr films and although ferromagnetism is predicted for the high temperature fcc phase of Cr paramagnetism is predicted for an fcc phase of Cr at the lattice parameter of Cu.

It has been hitherto assumed that the atoms are sitting in four fold hollow positions. This may not be the case. If the atoms were sitting in other sites then the interface spacing would be larger. The peaks which are starting to emerge at $(\pm 0.72 \ 1 \ 0.2)$ and $(1 \ \pm 0.72 \ 0.2)$ are an indication that the bcc phase of Cr is already forming. Such a structure will not sit commensurately on the Cu surface. The interface spacing will, therefore, be larger than that predicted for the packing of hard spheres into the four fold hollows.

It was mentioned earlier that, in order to lower the surface free energy, Cr islands could be covered with Cu atoms. This is a mechanism that cannot be ruled out. Unfortunately, due to the similarity of the Cr and Cu scattering factors and the lack of features in the data we cannot justify using such a model to describe our results.

5.6 Conclusion

This experiment has shown that the growth mode of Cr on Cu(001) is of a disordered nature. Only the growth done at low temperature has a feature which may be indicative of a poorly defined layer-by-layer growth mode. Both the growth at 100K and 300K follow the random deposition model closely. By 1ML the CTRs have already started to decay due to the islanding of Cr. This structure grows with its (110) surface parallel to the (001) surface of the Cu and with its $[\bar{1}11]$ axis parallel to the in-plane Cu $[\bar{1}10]$ axis in agreement with previous work.

The correlation lengths of 50.5 and 12.3Å along h and k respectively compares well with island sizes from previous work.

Four different models were used to fit the (00 l) rods for a 0.5 and a 1.0ML coverage. For the 0.5ML coverage all the models were found to describe the data adequately using only the roughness as a fitting parameter. Having any additional parameters does not significantly improve the χ^2 . For the 1.0ML coverage the sinusoidal and linear models gave the best agreement to the data showing that only a few layers contribute to the roughness of the film. Including the relaxations of the Cr overlayer considerably improved the fit showing that the Cr grows with an expanded interface spacing compared to a hard sphere radius model. Including the Cu relaxations in the fit, for either coverage, did not significantly improve the χ^2 .

Chapter 6

The Epitaxial Growth of Chromium on Silver (001)

6.1 Summary

The growth morphology and structure of ultrathin films of chromium deposited on silver (001) have been studied *in situ* by surface X-ray diffraction. The reflected X-ray intensity at the anti-Bragg position along the (00 l) rod was monitored during growth at temperatures between 100K and 473K. At room temperature there is a steady decay of the intensity indicative of disordered growth. At higher temperatures the variation of the intensity with time is consistent with coating of monolayer platelets of Cr with Ag. At 100K weak oscillations were observed which decayed relatively quickly. Scans along the reciprocal lattice vectors perpendicular to the surface were recorded for three different coverages. Expanded interfacial spacings were found in all of the films. For the two films grown at 100K analysis of the scans indicated that a fraction of the films were disordered. The film grown at a temperature of 440K is consistent with a model involving a layer of 78% Cr and 22% Ag sandwiched between a layer of 78% Ag and 22% Cr and the undisturbed substrate.

6.2 Background

There has been considerable interest in the properties of ultrathin metallic films supported on oriented single crystal surfaces. The reduced symmetry and atomic coordination will have a significant impact on the overlap of the atomic orbitals and in consequence on properties such as magnetism. Giant moments, perpendicular magnetic anisotropy and giant magneto resistance are some of the effects which have been attributed to reduced dimension (Fu *et al* 1985, Gradmann *et al* 1991).

Chromium on silver (001) is an interesting system to study for several reasons. The overlap of the Ag 4d and the Cr 3d bands is small and the Cr-Ag binary system exhibits a large miscibility gap above the melting point

(Venkatraman and Neumann 1990). The nearest neighbour separation in fcc Ag (2.89Å), along the vector \mathbf{a}_1 in figure 6.1, is 0.2% greater than the lattice parameter of bcc Cr (2.88Å) which would indicate that the bulk bcc Cr phase should develop on the (001) face of fcc Ag(001), with the bcc (001) plane parallel to the surface, but with the [100] axis rotated by 45° to that of the underlying substrate as shown in figure 6.1. On the other hand, the surface free energy of Cr (2400mJ/m²) is significantly greater than that of Ag (1250mJ/m²) suggesting that a flat Cr layer on top of an undisturbed silver substrate is energetically unfavourable.

There have been several studies of the growth of Cr on Ag(001). Newstead *et al* (1987) proposed from Auger electron spectroscopy that at room temperature the growth initially proceeds by the formation of monolayer islands with perfect epitaxy until approximately 1/3 of a monolayer and then by bilayers until two monolayers are completed. Further growth is disordered. The decay of the Ag surface state (Rouyer *et al* 1995, Krembel *et al* 1991b, 1992b), during room temperature deposition, suggests that multilayer or bilayer positions must be occupied before the completion of a monolayer. However, the linear decrease in the intensity of the same state, during deposition temperatures between 430K and 450K (Rouyer *et al* 1995, Krembel *et al* 1991a, Krembel *et al* 1991b, 1992b), is consistent with the growth of a flat monolayer. The weak second order spots found in the LEED pattern and the symmetry in the band structure measurements (Krembel *et al* 1991a, 1991c) found for this coverage, have been ascribed to a c(2x2) antiferromagnetic superstructure. It has been pointed out, however, that this flat layer could actually be a Cr-Ag alloy (Ortega and Himpsel 1993). In a room temperature study Krembel *et al* (1992a) claim that, to explain the features in their photoemission data, bilayers and multilayers of Cr must be coated by Ag which segregates from the bulk. They found no evidence, though, for coating of monolayer platelets an effect they attribute to the stabilisation of monolayer structures by antiferromagnetism. An angle resolved Auger measurement by Johnson *et al* (1988) at room temperature and a photoelectron diffraction measurement by Krembel *et al* (1991b) have both confirmed that the structure of the Cr overlayer was a rotated bcc structure as expected.

A recent study of Fe on Cu (001) (James *et al* 1995) has demonstrated that the stoichiometry of the outermost layers can be determined by surface X-ray diffraction.

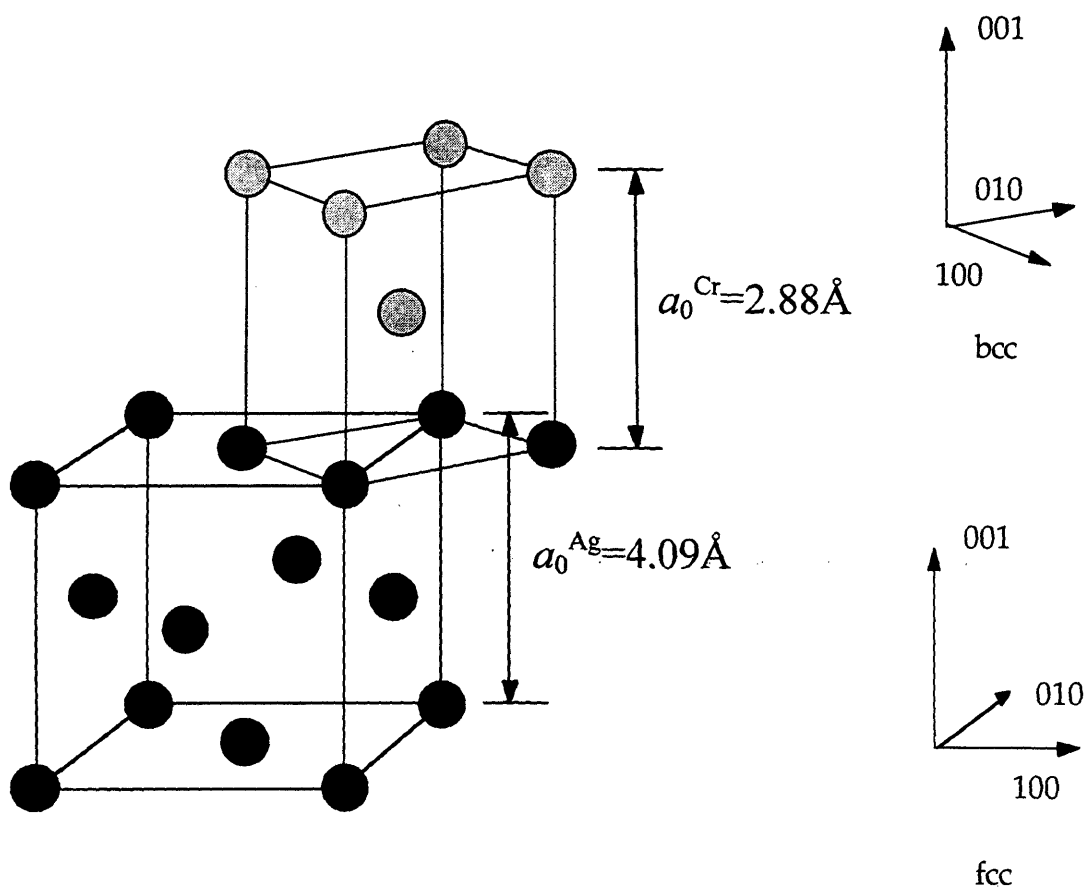


Figure 6.1. Diagram showing the matching of bcc Cr(001) on Ag(001).

We report here a study of the growth and atomic structure of Cr/Ag(001) from 100K to 473K. The results show clearly the change in the mode of growth and provide detailed information on the atomic structure, the ordering and the degree of intermixing.

6.3 Experimental Details

The Ag crystal sample, $8 \times 8 \times 1.5 \text{ mm}^3$, was cut and polished to within 0.4° of the (001) surface. Cleaning was done in vacuum by repeated cycles of argon ion bombardment and annealing to 600°C until no contamination could be detected by AES. The pressure in the chamber was 8×10^{-11} mbar; it rose to 2×10^{-10} mbar during evaporation. The coverage was confirmed using RBS. Typical deposition rates were 21 minutes per monolayer where one monolayer is defined as the real density of a single (001) plane of bulk silver, that is, 12.0×10^{14} atoms cm^{-2} .

The X-ray measurements were made on station 9.4 at Daresbury laboratory as described in chapter 4.

6.4 Results

6.4.1 Growth

Figure 6.2 shows the variation of the specularly reflected X-ray intensity with deposition time after the shutter on the vapour source was opened, for substrate temperatures between 100K and 473K. The X-ray signal was recorded at a grazing angle of 6.32° which corresponds to a scattering vector position at the (001) point in the reciprocal lattice of the fcc structure of Ag.

The plots show a distinct change with temperature. At 100K the intensity initially falls rapidly and then shows oscillations which decay. Such behaviour is typical of a poorly defined layer-by-layer growth mode. The peaks mark the completion of different layers; the rapid decay in their height is an indication of increased roughening in consequence of the low surface mobility. At room temperature the intensity again initially falls but, in spite of the increased mobility of the adatoms, there is no evidence of any maxima.

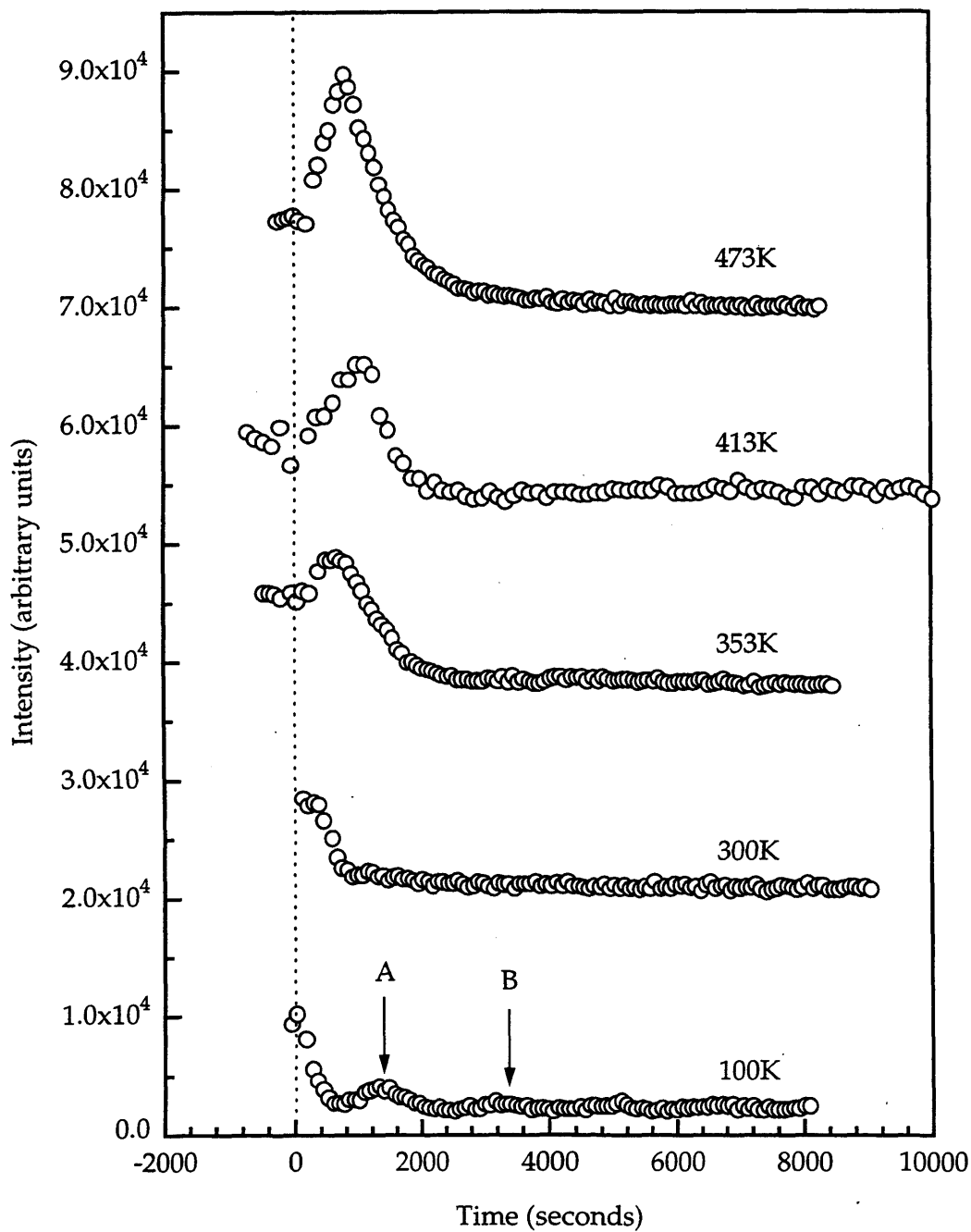


Figure 6.2. The intensity of the (001) position of reciprocal space versus time for different substrate temperatures. A and B denote the first and second maximum in the low temperature growth curve which correspond to 2 and 5 monolayers respectively.

At substrate temperatures above room temperature the intensity shows a noticeably different signature. The signal initially rises to a peak and then falls to a low value. The peak increases in strength and sharpness with increasing temperature. Since this maximum occurs at the time that the trough occurs in the low temperature data would correspond to a coverage of 1 monolayer (ML). Subsequent RBS analysis showed that the Cr deposition at the peak at 473K is 0.98 ± 0.05 ML. The initial rise is inconsistent with the growth of Cr on top of an undisturbed substrate and is attributed to a more complex growth mode. The difference in surface free energies of Ag and Cr would suggest that a structure with Cr as the top layer is energetically unstable and, if there is enough energy to initiate the process, will be replaced by Ag.

For growth of Cr on bulk terminated Ag (001), the total amplitude of the specular scattering can be expressed using equation 5.1

$$F_{001}^{total} = F_{001}^{bulk} + \sum_n \theta_n f^{Cr} \exp[2\pi i l z_n / a_0] \quad (6.1)$$

where

$$F_{001}^{bulk} = \frac{f^{Ag}}{1 - \exp[2\pi i l - a_0 / 2\mu]} \quad (6.2)$$

The meaning of the terms is described in chapter 5.

Figure 2.1 shows three simple models which have been considered for the initial stages of growth: (a) perfect layer by layer, (b) intermixing between the top layer of the substrate and the absorbate and (c) where Cr platelets are coated by Ag during growth. (a) can be described by equation (6.1) using appropriate values of θ_n and Z_n determined by the pseudomorphic assembly of Cr atoms on the Ag (001) substrate and using the bulk atomic radii for Ag (1.445 Å) and Cr (1.249 Å). The result for this model is shown in figure 6.3a. Since the initial growth is determined by the formation of monolayer islands, the curve predicts an initial fall in intensity. This is followed by a series of maxima which occur at the completion of several layers. The intensity of each break varies in consequence of the different scattering strengths of the two elements and the smaller interlayer spacing in the Cr overlayer. The model does not allow the roughness to increase

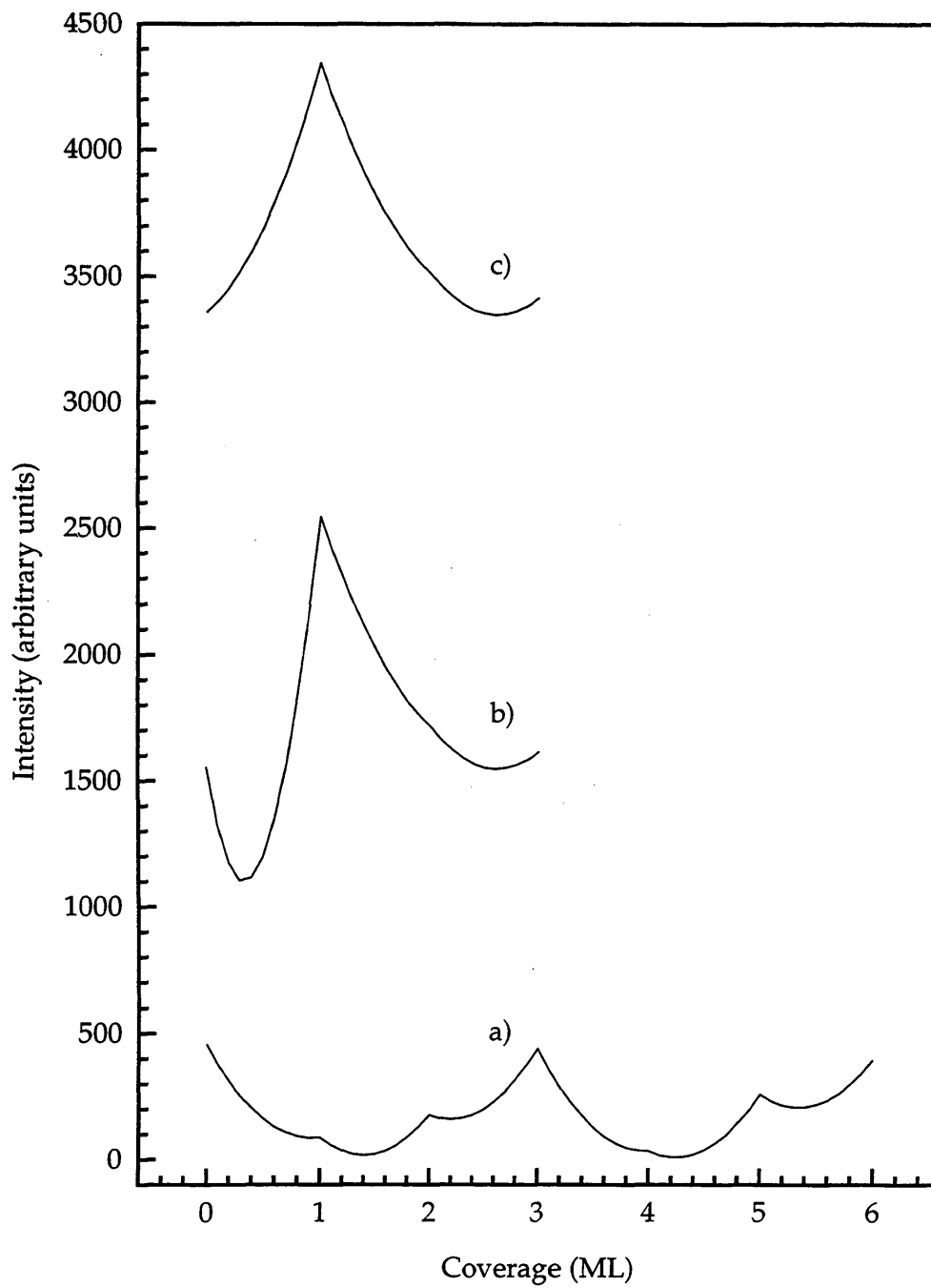


Figure 6.3. The predictions for the three models for growth shown in figure 2.1. a) Layer-by-layer b) 100% Intermixing c) Coating of adsorbate layer by substrate atoms.

but this would cause the intensity to decay and would obscure further maxima at higher coverages.

The intermixing shown in figure 2.1b can be described if we allow a degree of interchange between the first layer of Cr and the top layer of the Ag bulk. Measurements of Fe on Cu (001) (James *et al* 1995) confirm that there is significant intermixing even at room temperature. Accordingly we have tried to model the high temperature growth mode. As in Fe on Cu (001) we limit the intermixing to the topmost layer of the silver substrate. For the deposition up to the first ML of Cr the equation becomes:

$$F_{001}^{total} = F_{001}^{bulk} + [x\theta_1 f^{Cr} + (1-x)\theta_1 f^{Ag}] \exp[2\pi i l z_0 / a_0] \\ + [(1-x)\theta_1 f^{Cr} + x\theta_1 f^{Ag}] \exp[2\pi i l z_1 / a_0] \quad (6.3)$$

We have redefined the top layer of the substrate ($n=-1$) as the topmost undisturbed Ag layer; the sum extends over the two intermixed layers above. For simplicity we assume that all the atoms in a given layer are at the same height determined from weighted averages of the atomic radii.

Figure 6.3b is the prediction of this simple model with 100% intermixing. Figure 6.4 shows the prediction with varying degrees of intermixing x . After a coverage of 1ML, growth proceeds with complete Cr layers deposited onto the intermixed interface. As x increases the height of the peak at 1 monolayer also increases. For the higher values of x this maximum has a higher intensity than that from the clean substrate. The minimum which precedes the peak does not describe the shape of the high temperature data. This leads us to believe that although the coverage at 1ML has a certain amount of Ag in the top layer, depending on the temperature, the mechanism by which the growth evolves is different.

A better agreement is achieved if we allow the monolayer platelets of Cr to sit on the surface and be overcoated with Ag. This is illustrated in figure 2.1c. Equation (6.1) can be modified to account for this by:

$$F_{001}^{total} = F_{001}^{bulk} + \theta_1 f^{Cr} \exp[2\pi i l z_1 / a_0] + \theta_1 f^{Ag} \exp[2\pi i l z_2 / a_0] \quad (6.4)$$

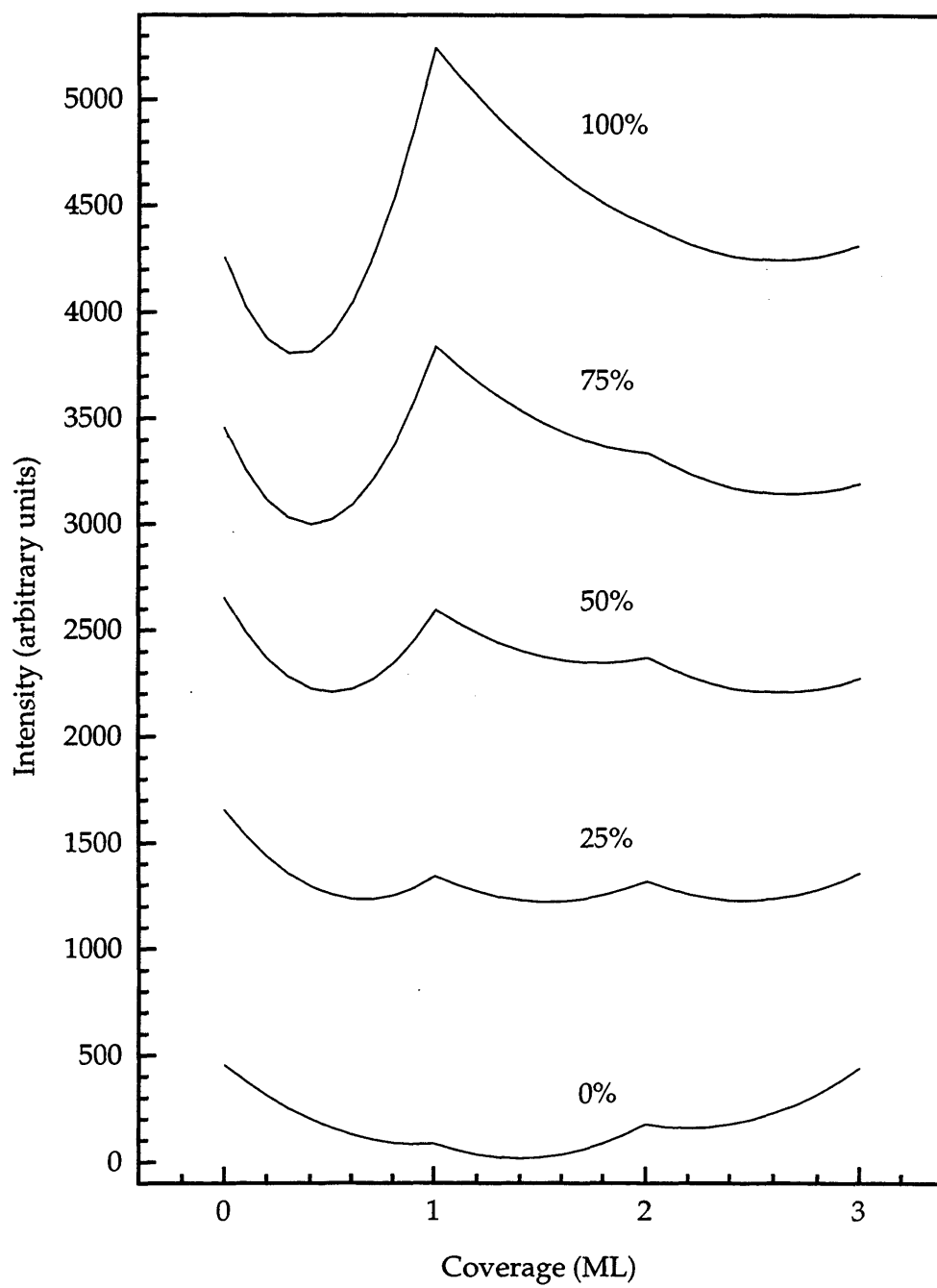


Figure 6.4. Predictions of the (001) intensity versus coverage for different degrees of intermixing of Cr on Ag(001).

The distances Z_1 and Z_2 corresponds to the height of the Cr platelets and the covering layer of Ag respectively.

Figure 6.3c is the prediction of this simple model. In agreement with the data taken with the substrate above room temperature, the intensity increases to the maximum at 1ML, without going through the minimum that is observed for intermixing. Following the coverage of a monolayer equivalent of Cr completely covered by a Ag layer the model proceeds as Cr layer by layer growth.

The perfect layer by layer model in figure 6.3 is clearly unable to explain the features in the high temperature data. It also fails to explain the low temperature data which shows a ratio of 2:5 between the time of the first and second maxima. Figure 6.5 shows the variation of intensity predicted for a perfect layer-by-layer model (equation 6.1) but with the interface spacings adjusted by an amount shown next to each curve. As the spacing is varied, the relative strengths of the maxima vary. At 0.20\AA expansion the strongest maximum are predicted at 2 and 5 monolayers in agreement with experiment. The weak peaks at 1, 3 and 4 monolayers were not observed due to the weakness of the measured signal.

6.4.2 Rod Scans

Measurements at one value of momentum transfer q only provide a limited picture of the surface structure. More detailed information was obtained by interrupting the growth and scanning along the $(00l)$, $(11l)$ and $(10l)$ crystal truncation rods (CTRs). The specular $(00l)$ rod is sensitive to the distribution of all the atoms in the overlayer but only along the surface normal. By contrast, the non-specular $(11l)$ and $(10l)$ rods contain information on the atoms in the overlayer in registry with the substrate.

Three different coverages were measured. Two were grown with the sample held at liquid nitrogen temperature. They were grown to the first and second maximum in the growth curve. Another coverage was grown with the sample held at 440K to the maximum in the intensity curve.

The low temperature growth curve decays rapidly indicating a poorly defined layer by layer by mode with significant roughness. The films were modelled by choosing a suitable function that would fix the occupancies of each layer of the film depending on the value of a single parameter. Some of the

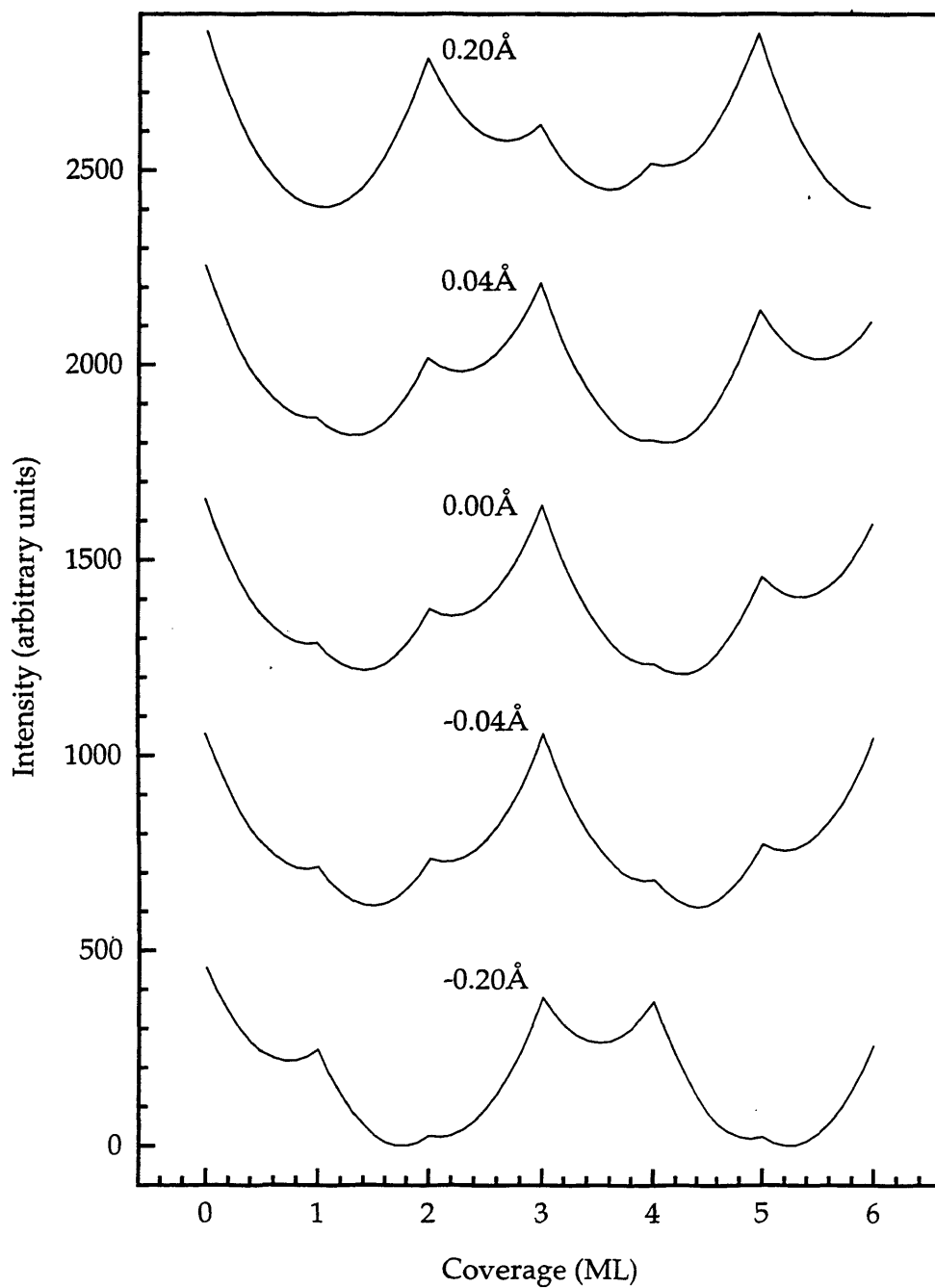


Figure 6.5. Predictions of the (001) intensity versus coverage for layer-by-layer growth of Cr on Ag(001) with the interface spacings adjusted by the amount shown.

models used to date are the Robinson Beta Roughness model, the Poisson model, the linear model and the sinusoidal model (see table 5.2). All these models involve all of the layers. Since the low temperature growth is poorly defined layer-by-layer mode some of the lower layers will already be completed. It is therefore necessary to choose another function that only involves the top few layers of the film since it will only be these that will contribute to the roughness. A suitable function that will fix the occupancies in this way is the Fermi function written below

$$\theta(N, N_0, \alpha) = \left(1 + \exp \left[\frac{N - N_x}{\alpha} \right] \right)^{-1} \quad (6.5)$$

where $N_x = N_0 + 0.5$

where N_0 is the coverage in monolayers, N is the layer number, α is a roughness parameter and θ is the occupancy of layer N . The value varied during fitting was the roughness parameter α of which a value of zero indicated a perfectly smooth surface. As the roughness parameter increases from zero the highest layers on a perfectly smooth film start to decrease in occupancy whilst higher layers, previously unoccupied, start to become populated.

The starting point for the displacements in the models was that calculated assuming a hard sphere radius for both atomic species.

The coverage grown to the first maximum with the sample held at liquid nitrogen temperatures was modelled with a total occupancy equivalent to 2ML. This coverage is consistent with RBS results. The (00 l), (10 l) and (11 l) rods with their best fits are illustrated in figure 6.6. Only six layers were used in the model because the occupancy determined from the equation for any higher layers would be negligible and would not influence the fit. However, out of these only the displacements of the most occupied i.e. the lowest three were allowed to vary in the fit. Including any more layers does not change the fit noticeably and the corresponding displacement values would have very large errors. The (00 l) rod best fit results are shown in table 6.1a. The lowest χ^2 of 1.85 was achieved with $\alpha = 0.3 \pm 0.1$. The corresponding layer occupancies are also shown. The errors in the

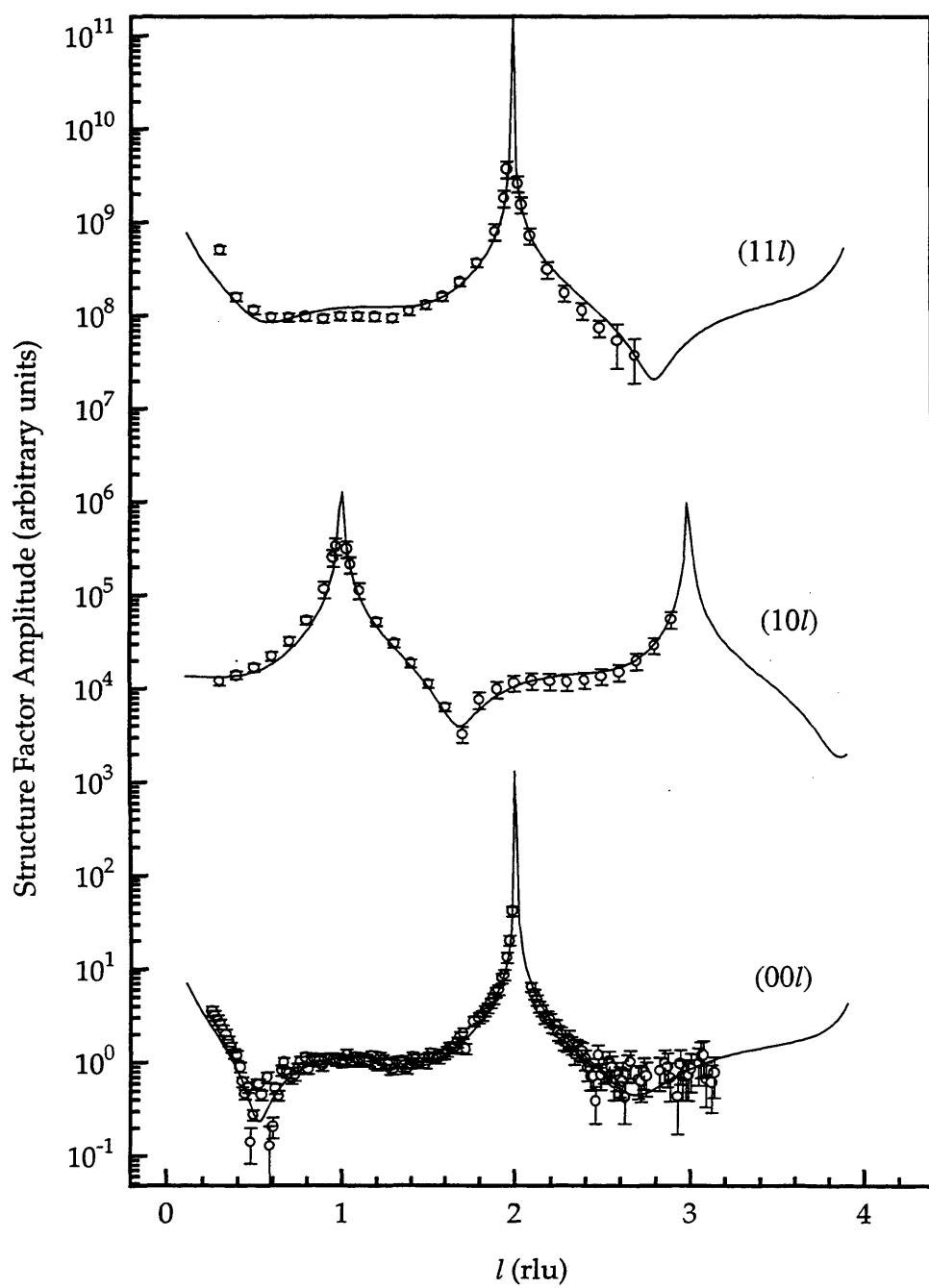


Figure 6.6. CTRs of the 2 monolayer coverage of Cr grown with the Ag(001) substrate at 100K.

three displacements are very large and very little can be determined from them. However there is a definite expansion in the lowest layer of $0.41 \pm 0.10 \text{ \AA}$.

If all the atoms in the resulting film were in epitaxial positions then the (00 l) rod would look very similar to the (11 l) rod and the same fit results should be satisfactory for all three rods. However, this is not the case, as can be seen from figure 6.6, indicating that there is substantial disorder in the films. To fit the (11 l) and the (10 l) rods it was assumed that a certain fraction of the film consisted of atoms in epitaxial positions i.e. that these two rods were only sensitive to this fraction. The resulting occupancies found in the fit to the (00 l) rod were multiplied by the same factor and then the lowest two displacements were allowed to vary. The resulting best fit has a multiplication factor of 0.5 ± 0.2 and a χ^2 of 2.75. The displacements are shown in table 6.1b. Again, the errors are quite large with the first displacement consisting of a noticeably large expansion similar to that found using the (00 l) rod.

Layer	Occupancy	Δd (Å)	Δz (Å)
1	0.993	0.41 ± 0.10	0.41 ± 0.10
2	0.841	0.05 ± 0.16	0.46 ± 0.16
3	0.159	-0.43 ± 0.78	0.02 ± 0.78
4	0.007		

Table 6.1a. Results for the (00 l) rod for the coverage grown to the first maximum in the growth curve with the sample held at liquid nitrogen temperature.

Layer	Occupancy	Δd (Å)	Δz (Å)
1	0.497	0.31 ± 0.16	0.31 ± 0.10
2	0.421	0.19 ± 0.25	0.50 ± 0.16
3	0.079		
4	0.003		

Table 6.1b. Results for the (10 l) and (11 l) rods.

The same fitting procedure was adopted for the second coverage which was attributed to a coverage of 5ML. The (00 l), (10 l) and (11 l) rods with their best fits are illustrated in figure 6.7. The total number of layers used was 10. The

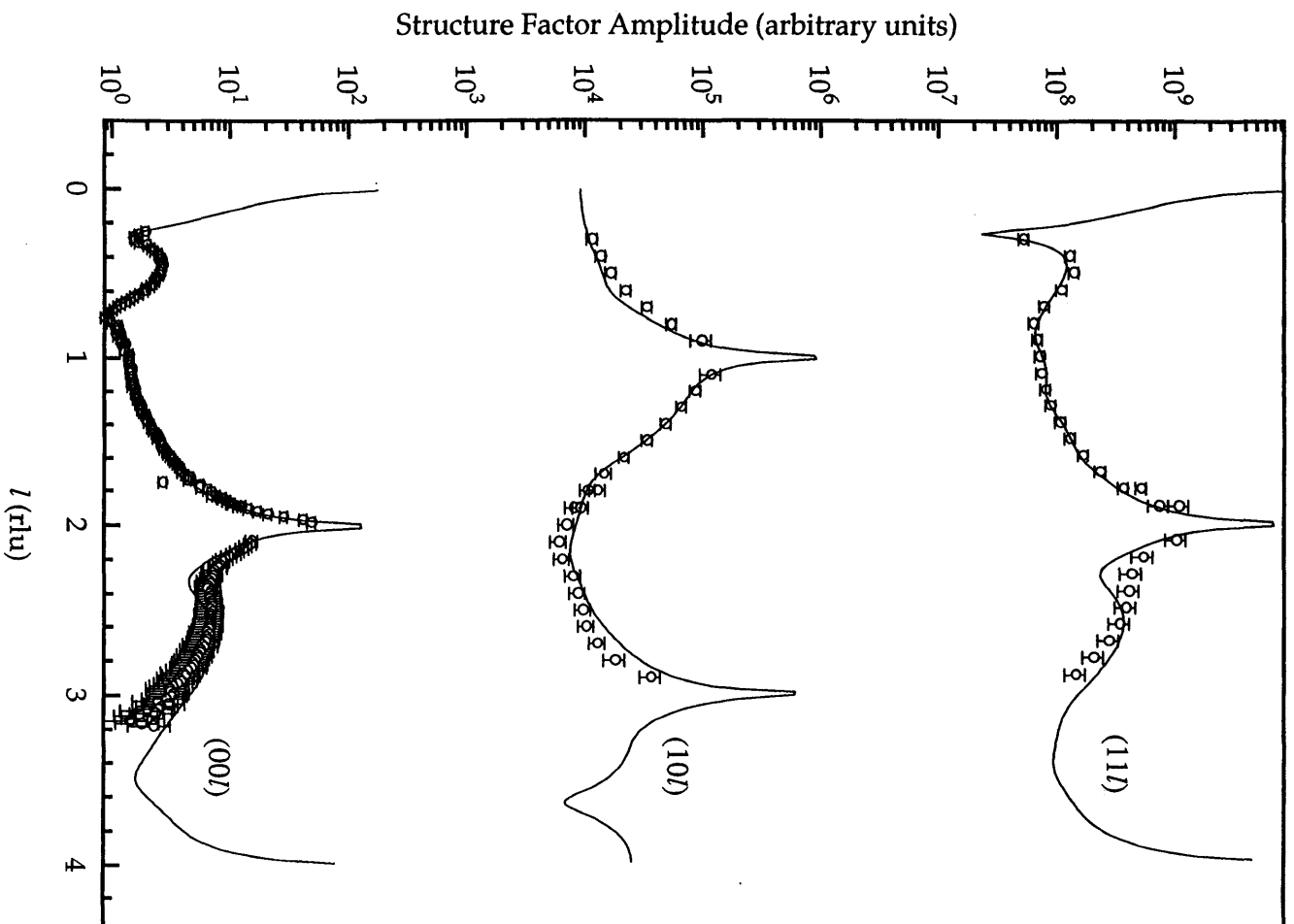


Figure 6.7. CTRs of the 5 monolayer coverage Cr grown with the Ag(001) substrate at 100K.

displacements between layers 2, 3 and 4 were kept at values determined from their hard sphere radii. Since these layers are in the middle of the film they will be less likely to succumb to low dimensional effects and therefore be more bulk like. The layers allowed to vary were 1, 5, 6 and 7. Since the layers 8, 9, 10 will have very small occupancy values their distances were kept constant. The best fit results, which yielded a $\alpha=0.7\pm0.1$ and a χ^2 of 1.73, are shown in table 6.2a. Yet again we get an expansion for the displacements. However, taking into account the size of the errors we can only be certain about the first layer expansion of $0.20\pm0.12\text{\AA}$. This expansion is not quite as large as the 2ML film as would be expected for a thicker film which would be expected to be more bulk like.

Layer	Occupancy	Δd (Å)	Δz (Å)
1	0.998	0.20 ± 0.12	0.20 ± 0.12
2	0.993	0.00	0.20
3	0.973	0.00	0.20
4	0.895	0.00	0.20
5	0.671	0.03 ± 0.10	0.23 ± 0.10
6	0.329	0.04 ± 0.20	0.27 ± 0.20
7	0.105	0.29 ± 0.65	0.56 ± 0.65
8	0.027		
9	0.007		
10	0.001		

Table 6.2a. Results for the (00l) rod for the coverage grown to the second maximum in the growth curve with the sample held at liquid nitrogen temperature.

Layer	Occupancy	Δd (Å)	Δz (Å)
1	0.799	0.16 ± 0.16	0.16 ± 0.16
2	0.795	0.00	0.16
3	0.778	0.00	0.16
4	0.716	0.00	0.16
5	0.537	0.08 ± 0.14	0.24 ± 0.14
6	0.263	0.19 ± 0.37	0.43 ± 0.37
7	0.084		
8	0.022		
9	0.005		
10	0.001		

Table 6.2b. Results for the (10l) and (11l) rods.

Although the (11 l) and (00 l) rods are very similar for this coverage, unlike the previous overlayer, the χ^2 was improved significantly by multiplying the occupancies by 0.8 ± 0.1 indicating that part of the film has atoms in non epitaxial positions. The layers 1, 5 and 6 were allowed to vary and gave values very similar to the (00 l) rod best fit result yielding a χ^2 of 2.58. The results of this fit are shown in table 6.2b.

The high temperature coverage consists of a monolayer. The (00 l) rod and the best fit result is shown in figure 6.8. To start the fitting procedure it was assumed that a monolayer of Cr atoms was sandwiched between the substrate and a complete monolayer of Ag atoms. The displacements between the Cr monolayer and the substrate and that between the outer Ag layer and the Cr layer were varied. However, the fit showed considerable improvement if a degree of interchange was allowed between these two layers. The lowest χ^2 of 2.36 was achieved with a degree of interchange of $78\pm 13\%$ with the displacements shown in table 6.3. The displacements shown are the deviations from a model that uses the average radii of each layer to determine the height.

Layer	Occupancy	Δd (Å)	Δz (Å)
1 Chromium	0.78 ± 0.13	0.12 ± 0.12	0.12 ± 0.12
1 Silver	0.22 ± 0.13	0.12 ± 0.12	0.12 ± 0.12
2 Chromium	0.22 ± 0.13	0.42 ± 0.10	0.54 ± 0.10
2 Silver	0.78 ± 0.13	0.42 ± 0.10	0.54 ± 0.10

Table 6.3. Results for the (00 l) rod for the coverage grown to the first maximum in the growth curve with the sample held at 440K. The distances shown are the departures from the calculated distances assuming hard sphere radii.

6.5 Discussion

The derived structure of all the films have expanded interlayer separations compared to a model that uses the hard sphere radii of the two atomic species. What is, however, more surprising is the size of the expansions. For the films grown at liquid nitrogen temperature the expansions in the first layer are 23%

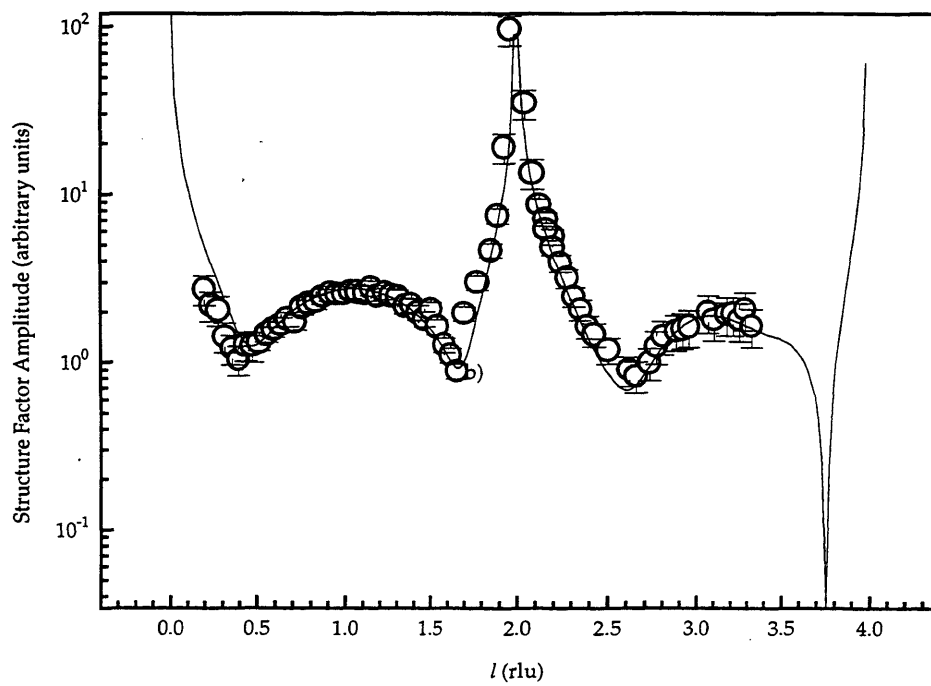


Figure 6.8. The (00l) rod for the one monolayer Cr coverage grown with the Ag(001) substrate at 430K.

and 12% for the 2ML and 5ML coverages respectively when measured with the specular rod. However, the size of the errors may mean that the expansions are not that large. This compares with the expansions found in Ag Cr superlattices found by Kyuno *et al* (1992). This large interlayer expansion is a possible contribution to the giant magnetic moment that is observed for thin Cr films supported on noble metal substrates. A larger separation would cause a decrease in the width of the d band density of states due to the lower overlap of the orbitals. As a result of this the electron spins would approach a parallel configuration thus increasing the net moment of the Cr atom. The reduced dimensionality and coordination of the film, alone, would also contribute to a more atomic like and therefore large magnetic moment. The model with expanded interlayer spacings is also in accord with the growth analysis. It has been shown that expanding the interface spacings causes the maxima at 2 and 5 ML to become relatively large compared to those that would occur at 1, 3 and 4 ML. This will, therefore, explain the observed ratio of 2:5 between the times of the first and second maximum in the low temperature growth curve.

The expansions deduced from the (11 l) and (10 l) rods are within error the same as that for the (00 l) rod for both of the low temperature coverages. However, the optimum values for the displacements obtained from the fit are also slightly smaller. If this is a true effect rather than a result of the errors it may be due to the disorder. A disordered film would not have the close packing of a regular crystal structure.

The surface alloy that is formed at 440K is surprising since no bulk analogue of Cr and Ag exists. However, the driving force of the overlayer structure may be the difference in the surface free energies. A Cr layer supported on an undisturbed Ag substrate is energetically unfavourable and the energy of the system could be lowered if an almost complete Ag layer covers the Cr layer. Surface alloys have been reported before for systems such as Au on Cu(001) (Wang *et al* 1987), Pd on Cu(001) (Wu *et al* 1988) and Mn on Cu(001) (Flores *et al* 1992, Wuttig *et al* 1993) which all form c(2x2) ordered alloy structures. What is more surprising is the discovery of surface alloys in systems such as Fe on Cu(001) (James *et al* 1995) and Au on Ni(110) (Pleth Nielson *et al* 1993) where the metals are mutually immiscible in the bulk. In all of these systems the intermixing of the two metals is limited to the top layer of the substrate. The idea

that Cr on Ag (001) may form a surface alloy is not new and has been mentioned before as a possibility (Ortega *et al* 1993).

From the growth analysis it has been concluded that intermixing does not describe the profile of the (001) intensity versus coverage/time. Instead a better agreement is obtained if we allow Ag to diffuse from the bulk to the top of the Cr monolayer platelets. This growth mode has been reported before for Rh on Ag(001) (Schmitz *et al* 1989) , Ag on Pb(111) (Chen *et al* 1985 , Rawlings *et al* 1980), Cu on Pb(111) (Rawlings *et al* 1980) and Fe on Au(100) (Bader and Moog 1987). In all of these cases the mechanism of the growth is thought to be driven by the difference in the surface free energies. They all result in sandwich type structures and likewise the result of the growth in this experiment should be a Ag/Cr/Ag(001) sandwich structure with no intralayer mixing. However, the vast improvement in the fit of the (00 l) rod, caused by allowing a degree of interchange between the two outer layers, cannot be ignored. A possibility is that only the initial part of the growth proceeds with Ag atoms migrating from step edges onto Cr platelets. After a certain amount of time, before the completion of the monolayer, this process may cease. The resulting overlayer may, as a result, give the same signature as an intermixed overlayer. An alternative model could involve some intermixing but with a dominant contribution from coating or segregation.

This is in contradiction to the model proposed by Krembel *et al* (1992a) and Rouyer *et al* (1993). They propose that coating or segregation does occur but only on bilayer and multilayer structures of Cr. They also found that a perfect monolayer of Cr can be formed if the Ag substrate is held at temperatures between 430K and 450K. The resulting structure resulted in weak second order spots on their LEED screen indicative of a c(2x2) super structure. They attributed the superstructure to 2D antiferromagnetic order which stabilises the Cr monolayer against coating by Ag and contamination. If intermixing does occur, however, it may offer an alternative explanation of the observed c(2x2) symmetry i.e. it may be a direct result of the atomic structure rather than the magnetic ordering. It would be possible to form a c(2x2) structure similar to Mn on Cu(001), shown in figure 2.2, if half of the top layer consisted of Cr atoms. However, the fit was consistent with $78 \pm 13\%$ of the top layer consisting of Ag which is a long way from 50% even if the errors are taken into account. We suggest that during the

growth process, which may be quite complex, some domains may develop where the top layer consists of 50% of each atomic species. Moreover, if the domains were small it may also explain why the LEED pattern observed by Krembel *et al* was so weak.

As shown in the section on growth the height of the maximum in the high temperature growth curves are sensitive to the stoichiometry of the overlayer (figure 6.4). The increase in the height with increasing substrate temperature is likely to be due to an increasing percentage of Ag forming the top layer with higher temperatures. This, itself would be a result of the increased mobility of the Ag atoms on or near the surface as the temperature of the sample is increased.

6.6 Conclusion

This experiment has shown the sensitivity of the growth of Cr on Ag (001) with the temperature of the substrate. With the sample at room temperature a disordered growth mode is found whilst at low temperatures a poorly defined layer by layer growth is favoured. This contrasts with growth at a higher substrate where a model involving coating of platelets of Cr with Ag atoms adequately describes the variation in the (001) intensity. Some intermixing may also contribute to the growth process.

Three coverages were measured. Two were grown with the temperature of the substrate held at liquid nitrogen temperatures and one at 440K. Expanded interlayer spacings, compared to values calculated assuming a hard sphere radius, were found in all of the films. This result is also supported by the analysis of the growth curves. The dominance of the peaks at 2 and 5 ML in the (001) intensity has been described by a simple layer by layer growth model with expanded interface spacings. The 2ML coverage was found to have only 50% of the Cr atoms in epitaxial positions compared to 80% for the 5ML coverage. The 1 ML coverage grown at 440K was described by allowing an interchange of $78 \pm 13\%$ between the Cr layer and the top of the substrate. However, it as been discussed that intermixing alone cannot describe the variation of the (001) intensity and the structure may be formed by coating of the Cr film with Ag probably migrating

from step edges. The fact that the top layer is not completely Ag indicates, however, that the growth process is more involved than this simple model.

Chapter 7

The Growth and Structure of Iron on Copper (001)

7.1 Summary

Fe on Cu(001) is a model heteroepitaxial system. In the next section previous work is reviewed highlighting the conflicting results which have been obtained so far. The growth at 300K is found to be consistent with a layer-by-layer growth mode. The growth of each layer begins with some lateral disorder which becomes more ordered as the occupancy of that layer increases reaching a maximum at the completion of the layer. Growth begins with significant intermixing at the substrate-overlayer interface but somewhere between the two coverages of 4 and 6.2ML the interface becomes sharp. No relaxation of the tetragonally distorted fcc structure (face centred tetragonal or fct) to the fcc or bcc structure is observed. Expansions at the top layer of the coverages have been attributed to magnetic effects. Expansions in the interface region have been attributed to either magnetism or the mutual immiscibility of the two atomic species. Finally a 4ML coverage grown at 100K is found to be stable against annealing up to a temperature of 400K.

7.2 Background

Fe exists in several different allotropes. At ambient pressure and temperatures up to 910°C Fe exists in the familiar bcc ferromagnetic phase with $a_0 = 2.867\text{\AA}$ with a nearest neighbour distance of 2.482Å (Wyckoff 1971). From temperatures of 910°C up to 1390°C Fe exists as an antiferromagnetic fcc (γ Fe) phase with a lattice constant equal to 3.647Å (Pearson 1958). From 1390°C to 1534°C a non-magnetic bcc phase exists (α Fe). If the lattice constant of fcc Fe is extrapolated down to 20°C, using the thermal expansion coefficient of the γ Fe, it becomes 3.59Å with a corresponding nearest neighbour distance of 2.54Å (Glatzel *et al* 1991) this is only 0.7% smaller than the lattice constant of fcc Cu. The fcc

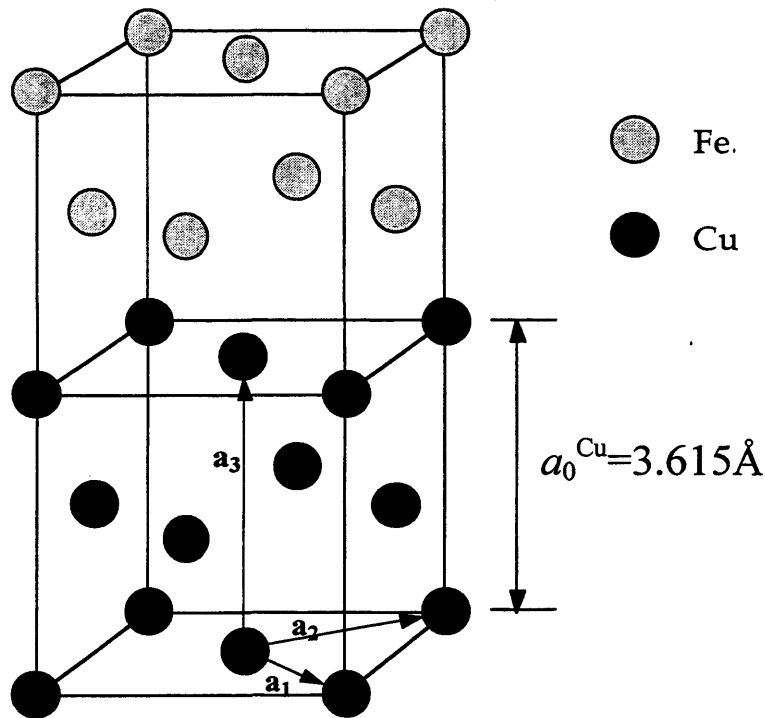
phase would, therefore, be expected to grow on Cu(001) with a slight tetragonal distortion to preserve the atomic volume (see figures 7.1 and 7.2). In favour of this is the mutual immiscibility of Fe and Cu in the bulk (Hansen 1953). However, the higher surface free energy of Fe ($2150\text{mJ}/\text{m}^2$) as compared to Cu ($1850\text{mJ}/\text{m}^2$) (Miedema 1978) would suggest that a layer of Fe supported by Cu(001) is energetically unfavourable. For successful layer-by-layer growth the sum of the adsorbate energy and the interface energy must be less than the surface free energy of the substrate.

Fe on Cu(001) was thought to be an ideal prototypical system for studying overlayer growth but the controversial results from experiments have highlighted the complexity of the system. Although it is generally accepted that Fe does form a strained fcc structure on the Cu(001) surface the growth up to 5ML and the point where the overlayer relaxes to the bcc phase are controversial.

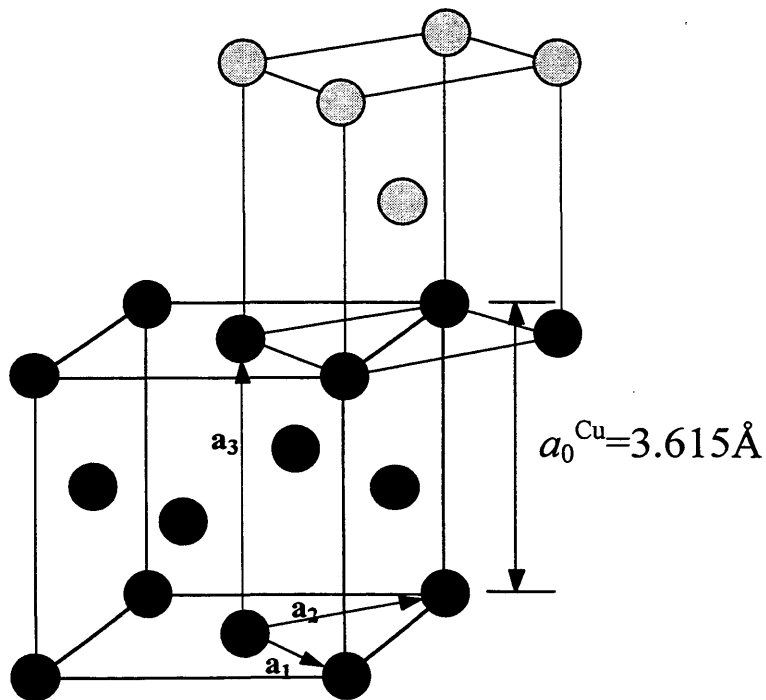
The first studies of Fe on Cu(001) go back to Haase (1956) but the first reliable UHV results were acquired by Jesser and Matthews (1967,1968) where a stabilisation of a pseudomorphic uniaxially strained Fe fcc structure was formed. Chambers *et al* (1987) have grown good quality fcc films at room temperature up to a coverage of 5ML. Growth begins by the formation of 2 layer deep clusters. After 3ML growth proceeds as well ordered flat layers. Above 5ML the quality of the film diminishes. At elevated substrate temperatures (398K) interdiffusion of Fe atoms into the Cu substrate occurs which displaces the Cu atoms into the overlayer structure.

From break points in their Auger signal versus time plots Newstead *et al* (1987) found that up to a coverage of 4ML growth proceeded by a layer-by-layer mode. These results were confirmed by Germar *et al* (1988) again by monitoring the Auger amplitude as a function of time. Using Auger Glatzel *et al* (1991) found that growth proceeded by bilayer growth for the first 2 bilayers. These results were confirmed by Rutherford Back Scattering analysis (RBS). Their LEED patterns were 1×1 and indistinguishable from that from the clean substrate.

RHEED and XPS (Steigerwald *et al* 1987,1988) results suggest that significant Fe agglomeration occurs with double layer high islands for the first monolayer. A gradual burying of the substrate surface occurs by 5ML. After 5ML the growth mode is layer-by-layer. Some intermixing occurs at room temperature which becomes severe at 673K. It was concluded that 3ML films were the lowest

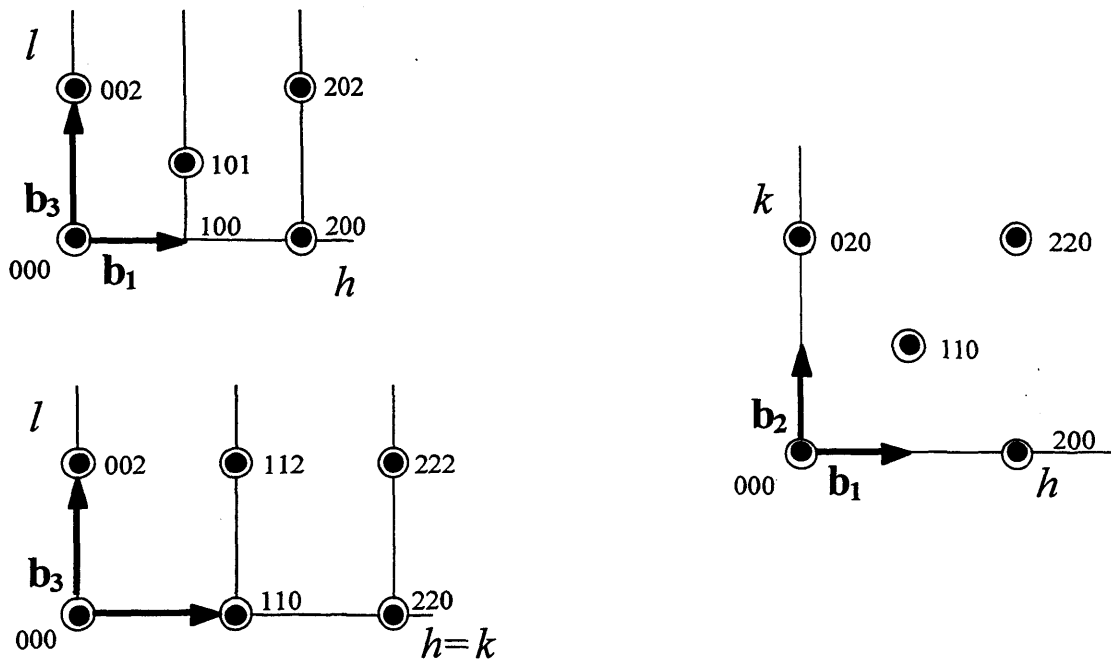


a) Lattice matching of fcc Fe(001)/Cu(001)

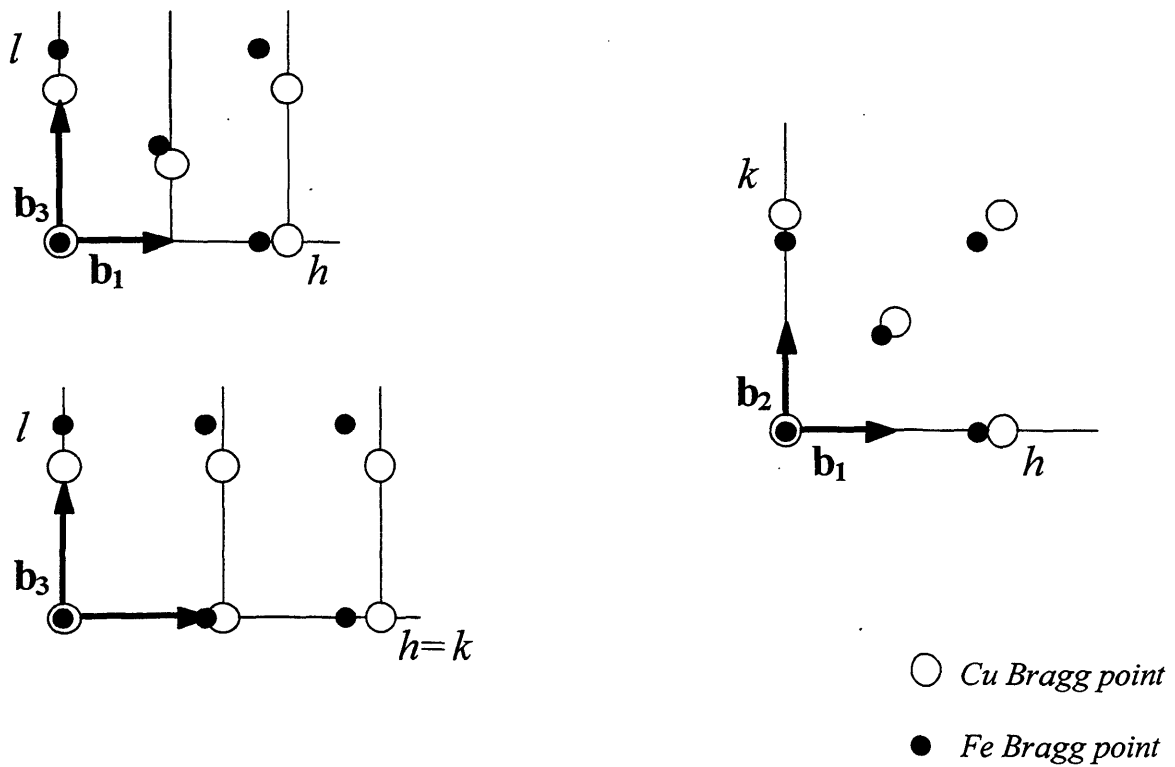


b) Lattice matching of bcc Fe(001)/Cu(001)

Figure 7.1. Diagram showing the matching of a) fcc Fe(001) on Cu(001) and b) bcc Fe(001) on Cu(001). Also shown are the real space vectors \mathbf{a}_1 , \mathbf{a}_2 and \mathbf{a}_3 used in describing the Cu(001) surface.



a) fcc Fe(001)/fcc Cu(001). Perfect lattice matching, i.e. $a_0^{Cu} = a_0^{Fe} = 3.615 \text{ \AA}$.



b) bcc Fe(001)/fcc Cu(001). Fe relaxed and rotated 45° with respect to Cu(001)
 $a_0^{Cu} = 3.615 \text{ \AA}$ and $a_0^{Fe} = 2.8665 \text{ \AA}$.

Figure 7.2. Diagram of reciprocal space for fcc Fe(001) and bcc Fe(001) grown on fcc Cu(001)

coverage that could be prepared with structural integrity. This growth behaviour is supported by the LEED I-V, Medium energy electron diffraction (MEED) and AES data of Thomassen *et al* (1992).

Helium atom scattering (HAS) has been used by Arnott *et al* (1992) and Dastoor *et al* (1992) to monitor growth at 220K, 298K and 420K. At 220K growth is diffusion limited and manifests itself as a simultaneous multilayer mode. At 298K growth is more organised with deterioration in the quality of the film occurring at 7ML possibly due to misfit dislocations. At 420K growth is layer-by-layer, however, Auger measurements suggest that intermixing occurs at the interface, that is an epitaxial surface alloy is formed.

RHEED results (Wuttig *et al* 1993) show irregular intensity oscillations below 5ML due to Fe agglomeration. After 5ML the oscillations become regular with a monolayer period but gradually decay as epitaxial growth breaks down. Interdiffusion of Fe and Cu was reported for films deposited at a substrate temperature of 370K. Johnson *et al* (1993) reported significant intermixing in the early stages of growth with the formation of Fe inclusions in the top substrate layer. Above 2.8ML the growth mode was layer-by-layer. Detzel *et al* (1993) have interpreted their results in the formation of bilayer growth up to 2ML with 50% Fe inclusion in the top substrate layer. In contrast to this STM measurements by Giergiel *et al* (1994) show no evidence for intermixing and a layer-by-layer growth mode begins at a coverage of 4ML.

Using RHEED Schatz *et al* (1994) established that growth at room temperature began with bilayer formation for the first 2 layers which was followed by layer-by-layer growth. Between substrate temperatures of 333-370K good regular intensity oscillations were observed indicating that layer-by-layer growth takes place through the whole coverage regime. Further STM work by Johnson *et al* (1994) showed that Fe incorporation into the substrate occurred below a coverage of 0.2ML. After this a simultaneous multilayer growth mode ensued. By comparing MEED diffraction intensities with scanning tunnelling microscopy (STM) results (after Thomassen *et al* 1992) Chambliss *et al* (1993) have applied kinematic analysis to deduce that growth is initially poorly ordered layer-by-layer but improves with coverage until the structure relaxes to the bcc phase. James *et al* (1995) has found that intermixing occurs between the top layer of the substrate and first adsorbate layer. From the intensity oscillations layer-by-

layer growth is found through the whole coverage range until the relaxation to the bcc structure. No evidence for bilayer growth is found.

The exact coverage where the film relaxes to the bcc phase is controversial. Using LEED, MEED and AES Thomassen *et al* (1992) and Wuttig *et al* (1993) observed the relaxation at 14ML. Using SXRD James *et al* (1995) has found a similar value of 13ML for the bcc relaxation. However, Giergel *et al* (1994) have found that the fcc films show a structural instability as low as 4.6ML. This is attributed to a dislocation network which is the precursor to Fe formation.

Clark *et al* (1987) has used LEED I-V to examine the changes in the structure of a film grown at 300K up to 7ML. These changes are thought to correlate with the magnetic state of the films. The expansions of the interlayer spacings are thought to be responsible for the onset of ferromagnetism in the films (Pescia *et al* 1987). Expansions were also found by James *et al* (1995) in coverages as below 4ML. These were also attributed to the magnetism of the films. The extended X-ray absorption fine structure (EXAFS) measurements of Magnan *et al* (1991a, b) have also established a coverage dependent overlayer structure. Antiferromagnetism is attributed to the fcc structure of Fe whilst ferromagnetism is ascribed to that of the distorted fcc structure.

Contradictory magnetic behaviour has been reported. The Fe overlayer has been observed to be antiferromagnetic (Macedo *et al* 1991), ferromagnetic (Allenspach and Bischof 1992) and non-magnetic (Bader and Moog 1987). Perpendicular surface anisotropy has been observed in ferromagnetic films (liu *et al* 1988) using the polar Kerr effect. This anisotropy reverts to an in-plane magnetisation for films thicker than 6ML. The magnetic phase diagram of Fe on Cu(001) has been measured by Dongqi *et al* (1994). Three distinct magnetic phases have been identified as a function of Fe coverage and substrate temperature during growth.

There is obviously considerable disagreement between different experiments even where the same technique is employed. It is generally agreed, however, that layer-by-layer growth occurs between 5 and 10ML and that there is a relaxation to the bcc phase. The coverage that relaxation occurs may depend critically on growth conditions, the UHV environment and sample preparation.

In this chapter *in-situ* SXRD data is shown along with scans on films grown to various coverages with the substrate held at room temperature. A 4ML

film grown at low temperature is scanned and then annealed and rescanned to see if any reordering takes place.

7.3 Experimental Details

The preparation of the Cu sample was the same as described in chapter 5 but the experiment was conducted at the ESRF on ID3. The high intensity of the beam on ID3 enabled us to monitor the in-plane diffuse scattering, which is very weak, and to obtain more data. Fe, of purity 99.999%, was deposited from a water cooled Knudsen cell. During deposition the base pressure in the chamber increased from 1×10^{-10} mbar to 5×10^{-10} mbar.

One monolayer is defined as the density of a single (001) layer of bulk Cu, i.e. 1.53×10^{15} atoms cm^{-2} . The momentum transfer is expressed by Miller indices h , k and l , referred to the tetragonal Cu(001) unit cell as defined in chapter 4.

7.4 Results

7.4.1 Growth

Figure 7.3 shows the variation of the specularly reflected intensity, at the (001) point of reciprocal space, as a function of time during deposition for a substrate temperature of 300K. The X-ray signal was recorded at a grazing angle of 7.15° which corresponds to a scattering vector position at the (001) anti-phase position in the reciprocal lattice structure of the fcc structure of Cu.

In contrast to the growth of Cr on Cu(001) well defined oscillations are seen indicative of a layer-by-layer growth mode with each peak corresponding to the completion of a layer. The damping of the intensity occurs as a result of increased surface roughness.

Also shown in figure 7.3 is the intensity of the (1 0 0.085) position of reciprocal space as a function of deposition time with the substrate at 300K. This position is close to the (100) point which is also an antiphase position. This position is sensitive to the (1 $\bar{1}$ 0) planes of the bulk and is therefore sensitive to the growth of epitaxial islands. This is in contrast to the (001) position which is

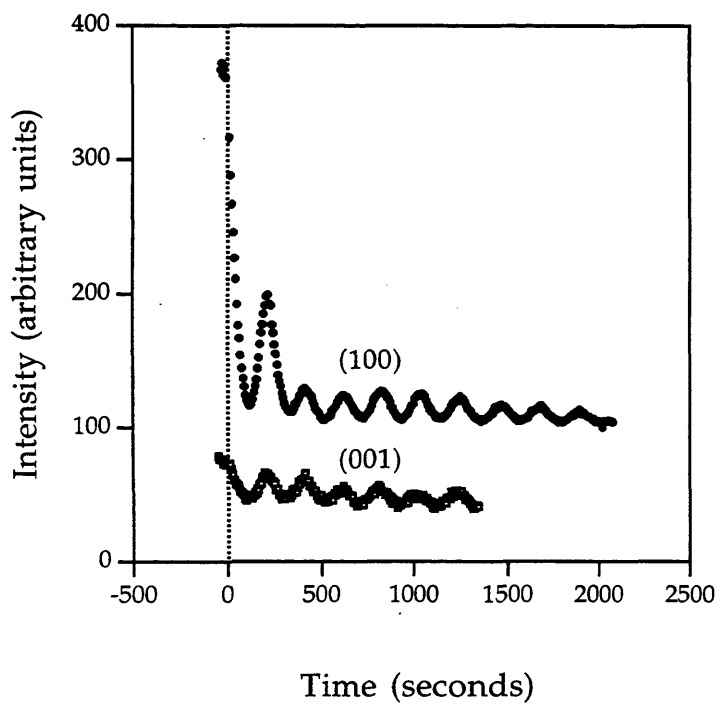


Figure 7.3. The intensities of X-rays scattered at the (001) and (100) reciprocal lattice points recorded during growth with the substrate at 300K

sensitive to all of the atoms sitting on the surface. The $(100)_{\text{surface}}$ point of reciprocal space has both the incoming and outgoing wave vectors in the plane of the surface so that the beam does not penetrate the bulk. The beam is, therefore, not sensitive to thermal disorder. Here oscillations also occur which are in phase with the (001) intensity oscillations. However, the sharp initial decrease of the oscillations and the contrast to the (001) intensity means that some of the atoms are not sitting in epitaxial positions.

By measuring the diffuse scattering around the (1 0 0) peak the correlation length can be calculated. If the peak has a profile that can be described by a Lorentzian then the correlation length L is related to the resolution in reciprocal space Δq given by equation 5.2. i.e. $L=2/\Delta q$. Another film was grown with the temperature of the substrate at 300K but the growth was interrupted at successive intervals so a full scan of the (1 0 0.085) peak could be achieved. This procedure was done up to a coverage of 6ML. No diffuse scattering around the peak could be seen so the full width half maximum (FWHM) and the height of each (1 0 0.085) reflection were measured. The FWHM was measured by fitting a Lorentzian peak to the data. From knowing the width Δq can be found and the correlation length can be calculated. The height of the peak and the correlation length are shown in figure 7.4. Both oscillate in phase with each other, the peaks coinciding with the completion of each layer.

Selected (1 0 0.085) scans are shown in figure 7.5. The absence of well defined wings as seen for Ag grown on Ag(100) (van der Vegt 1995) implies that there is not a well defined characteristic length on the surface i.e. there are islands of a range of sizes.

7.4.2 Relaxation of the Pseudomorphic fct Structure.

The energy of the strained fcc structure, or fct structure, increases with coverage. Eventually the energy will exceed that which is needed to form the relaxed bcc structure. To observe this relaxation the in-plane peaks can be scanned. If the pseudomorphic Fe phase exists then the scattering from the overlayer will coincide with that from the bulk Cu. However, relaxation of the Fe overlayer will manifest itself as satellite peaks around the (2 0 0.085) peak. Up to a

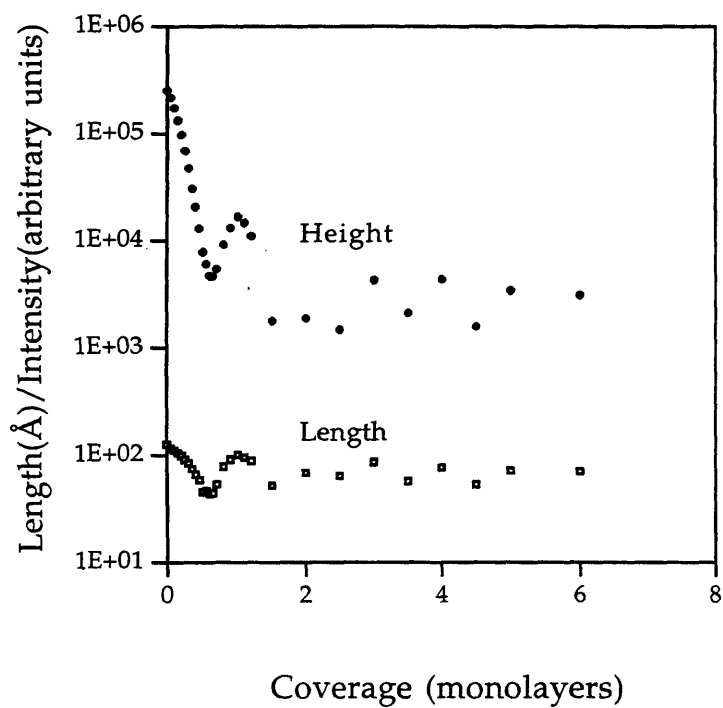


Figure 7.4. The correlation length and intensity of the (100) intensity versus coverage.

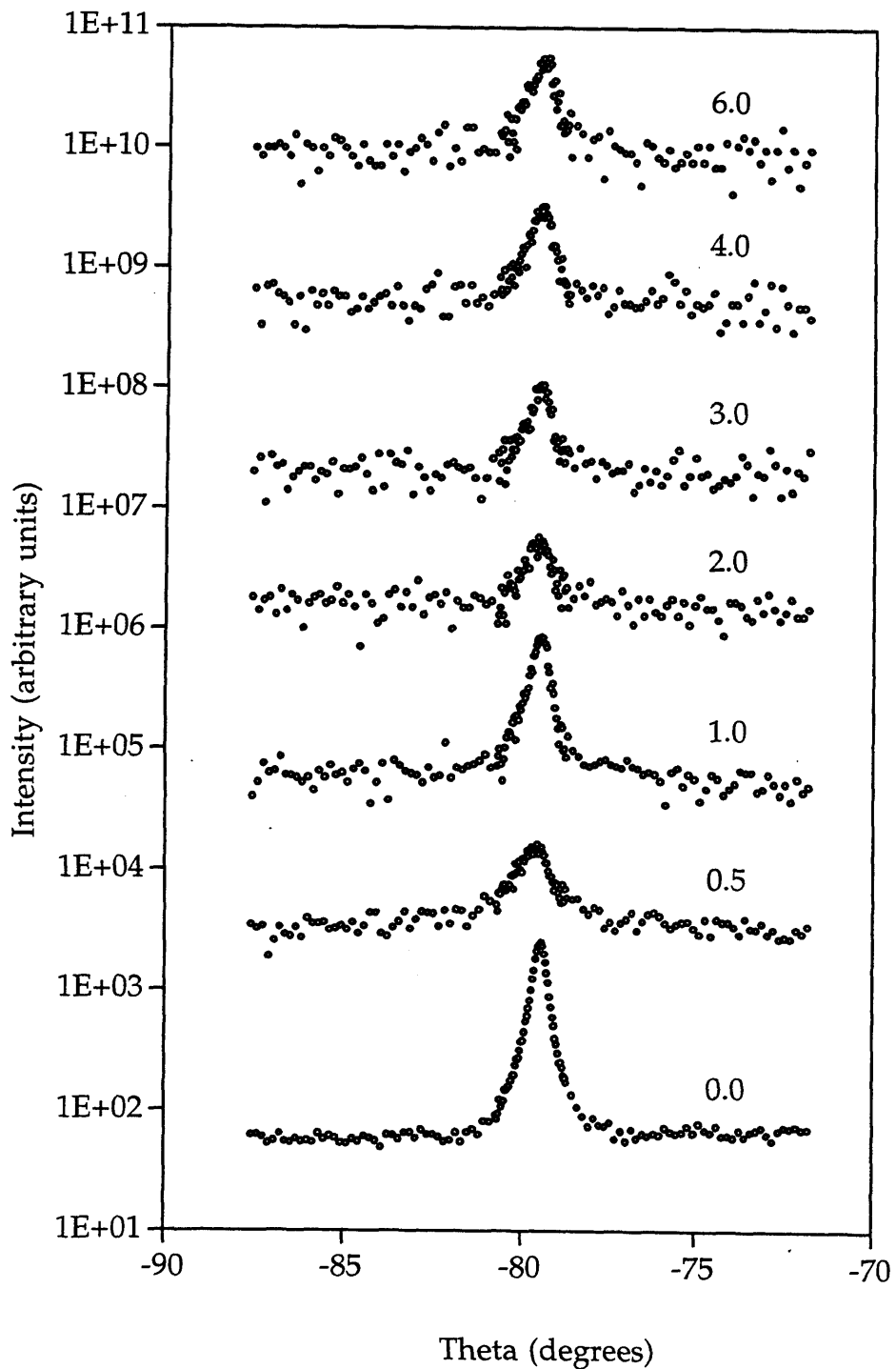


Figure 7.5. Scans of the (1 0 0.085) reflection for various stages of growth. The total coverage in monolayers is shown next to the curves. The intensities are offset for clarity.

coverage of 6ML no extra peaks were seen. Scans of the (2 0 0.085) peak for several coverages up to 6.0ML are shown in figure 7.6.

Since the pseudomorphic Fe layer is tetragonally strained it may relax back to its unstrained fcc structure. By scanning close to the (2 0 0.15) peak this would be seen as an asymmetry in the reflection. Scans around this reflection, for several coverages (see figure 7.7) have shown some asymmetry, however, this is due to the rod profile and the fact that the Ewald Sphere cuts the rod at an angle as even the clean surface scan shows some asymmetry.

7.4.3 Rod Scans

Since intermixing has been mentioned in the literature for this system (James *et al* 1995, Detzelet *et al* 1993, Johnson *et al* 1994) it has been included in the analysis. In accordance with previous work intermixing was assumed to take place between the top layer of the substrate and the first layer of the adsorbate only. The growth mode therefore proceeds by Fe adatoms incorporating themselves into the Cu(001) surface and ejecting Cu atoms becoming part of the first adsorbate layer. Following this growth was assumed to proceed by layer-by-layer growth. When fitting the data the parameter allowed to vary was the intermixing degree x . This is defined as the percentage of atoms in the top layer of the substrate that are Fe. The software did not allow a sophisticated fitting of the intermixing degree x so instead it was varied from 0 to 100% in steps of 5% whilst other parameters were allowed to vary. The Fe and Cu atoms in the intermixed region were assumed to randomly occupy fcc positions. Depending on the coverage suitable interlayer spacings were allowed to vary. The starting positions for the distances were calculated from the perfect pseudomorphic packing of the hard spheres of Fe (1.27Å) and Cu (1.28Å). The Fe radius is calculated by extrapolating from the high temperature Fe fcc γ phase using the thermal expansion coefficient. At the intermixed region distances were calculated using an average atom model to determine the average radius of the atoms in that layer. In all of the films analysis began by losing the heights of the two intermixed layers and the topmost layer of the overlayer. These layers were allowed to vary because the corresponding atoms will be in different environments from their bulk and are therefore more likely to differ from

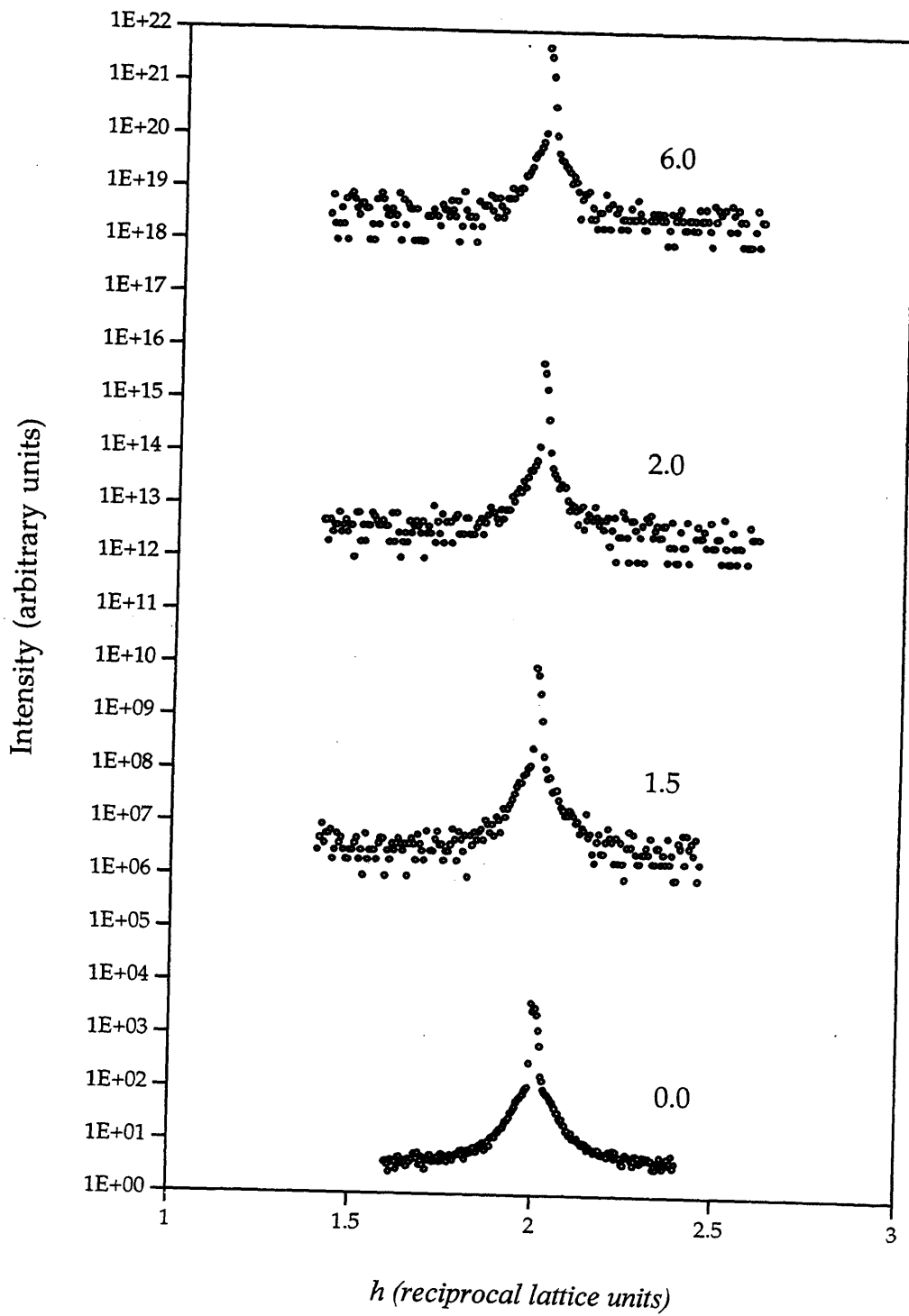


Figure 7.6. Scans of the (2 0 0.085) reflection for different coverages. The coverage in monolayers is shown next to each curve. The intensities are offset for clarity.

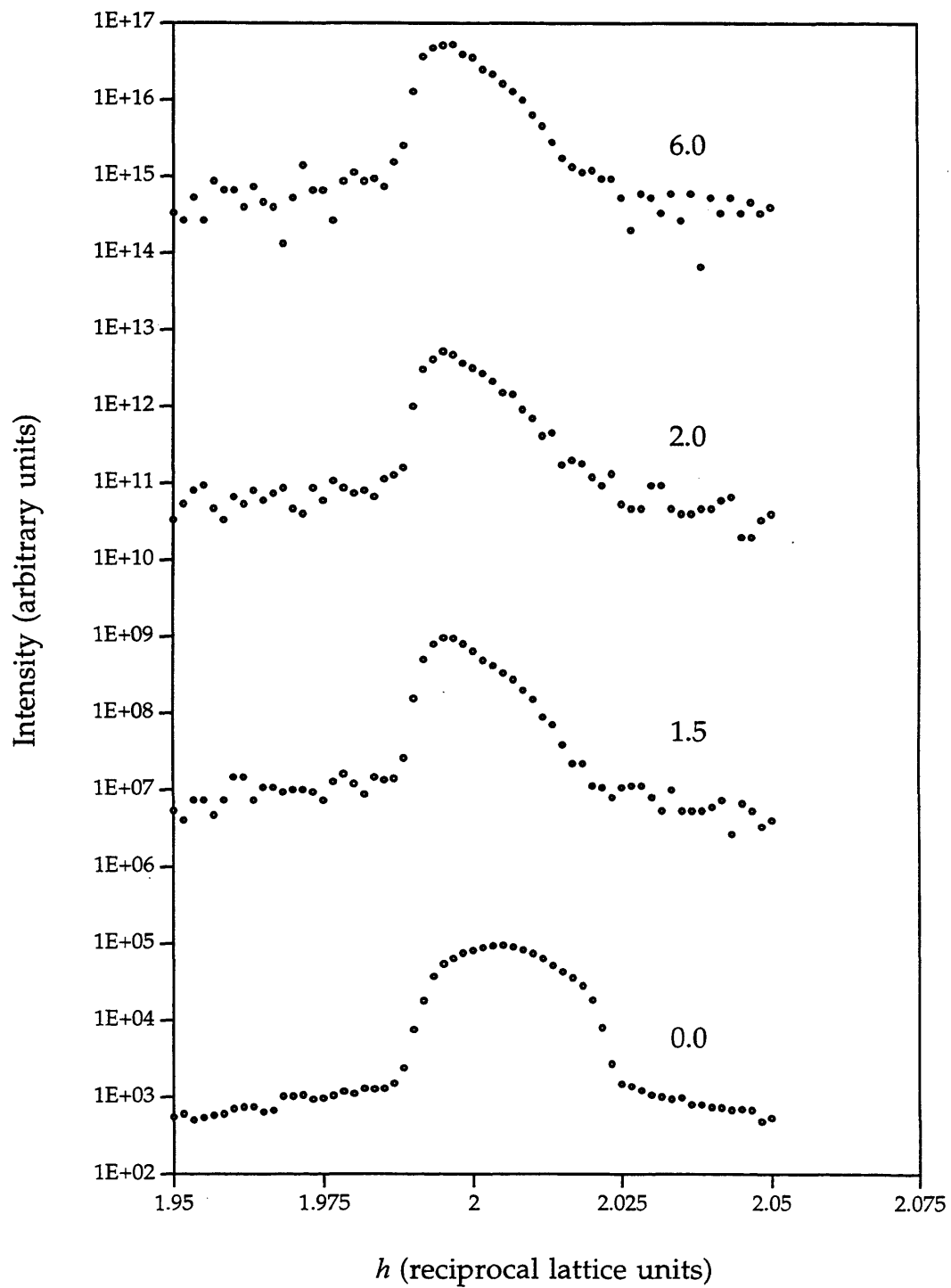


Figure 7.7. Scans of the (2 0 0.085) reflection for different coverages. The coverage in monolayers is shown next to the each curve. The intensities are offset for clarity.

positions calculated from their bulk radii. Furthermore the layers were varied as a single integral unit. The in-plane lattice parameter of the Fe overlayer (2.55Å) was kept constant during the analysis. Müller *et al* (1995) varied the in-plane parameter in their LEED analysis and although the fits were improved the results were ultimately dominated by the vertical spacings. The model used in the analysis is shown in figure 7.8.

Three different coverages were grown and measured at 300K: a 4ML coverage, since a change in the growth and structure of the film occurs at this point, an 8ML coverage, which is a fairly high coverage but is still below the point where relaxation to the bcc phase occurs, and a 6.2ML coverage which is approximately between the two. The rod data with their corresponding best fits are shown in figures 7.9-7.11. The best fit results are presented in table 7.1 in the form of changes in interlayer distances Δd rather than in height Δz .

For all of the coverages the heights of the top intermixed layer ($\Delta z_{-1,1}$) and the height of the outermost layer ($\Delta z_{-1,4}$, $\Delta z_{-1,6}$, $\Delta z_{-1,8}$ for the 4, 6.2 and 8ML coverages respectively) were allowed to vary. The 4 and 6.2ML fits were improved by including the bottom intermixed layer ($\Delta z_{-1,0}$). The 4ML coverage fit was significantly improved by including the height of the first complete Fe layer above the intermixed region ($\Delta z_{-1,2}$). Intermixing did not improve the fits to the rod data for the 6.2ML and 8ML coverages. In contrast to this the fit to the 4ML coverage data was improved greatly by including intermixing resulting in a value of 75%.

Coverage ML	x	$\Delta d_{-1,0}$ (Å)	$\Delta d_{0,1}$ (Å)	$\Delta d_{1,2}$ (Å)	Δd_{outer} (Å)	χ^2
4.0	0.75	0.050±0.03	0.020±0.03	0.050±0.03	0.082±0.03	3.63
6.2	0.00	0.007±0.03	0.061±0.03	0.000	0.103±0.03	3.18
8.0	0.00	0.000	0.064±0.03	0.000	0.035±0.03	3.50

Table 7.1. Best fit results to the rod data.

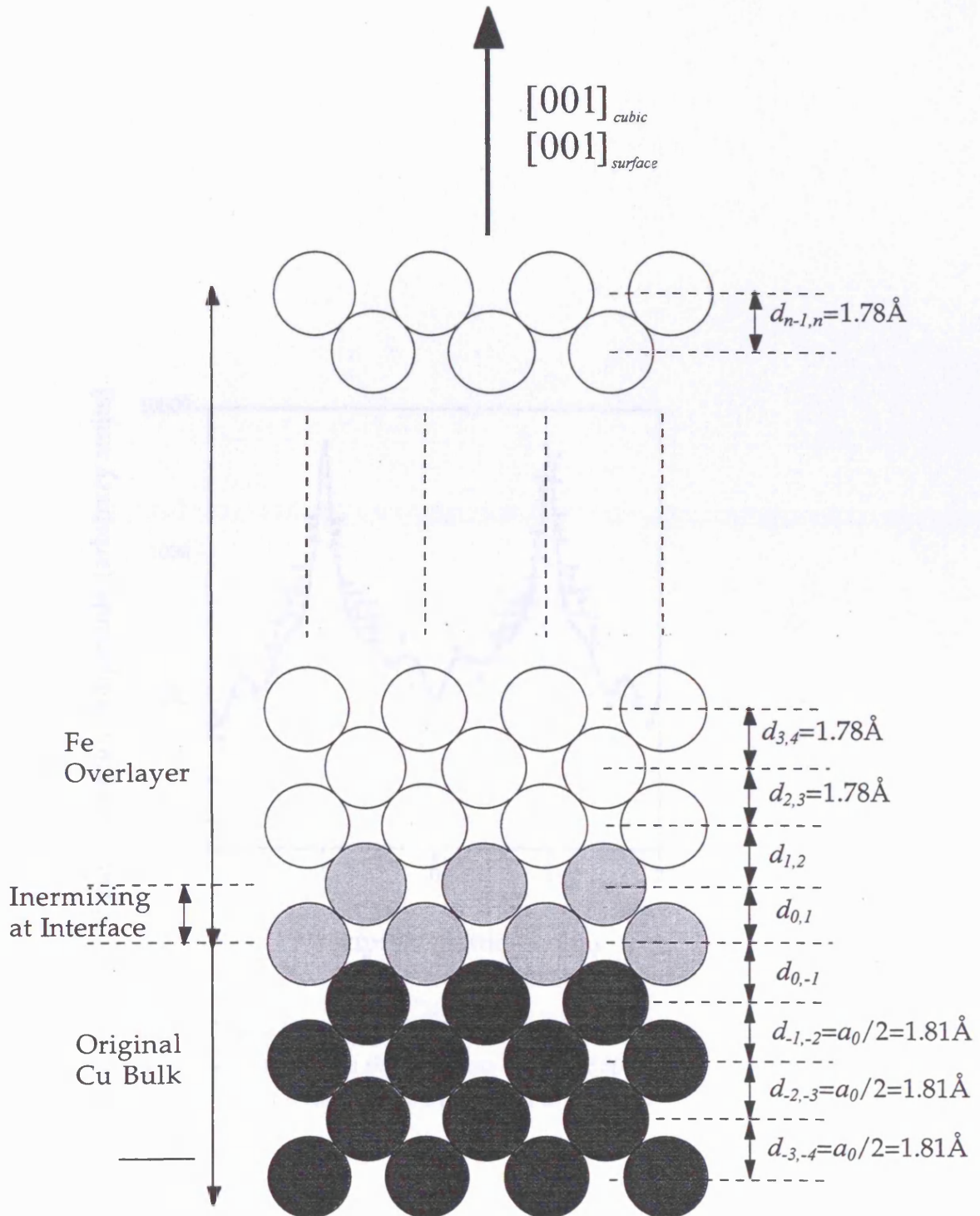


Figure 7.8. Schematic of the model used to fit Fe on Cu(001). The interlayer distances shown correspond to those calculated from the hard sphere radii of the two atomic species (1.27 \AA and 1.28 \AA for Fe and Cu respectively). The distances $d_{0,-1}$, $d_{0,1}$ and $d_{1,2}$ were calculated using an average atom model. The distances therefore depend on the degree of intermixing at the interface.

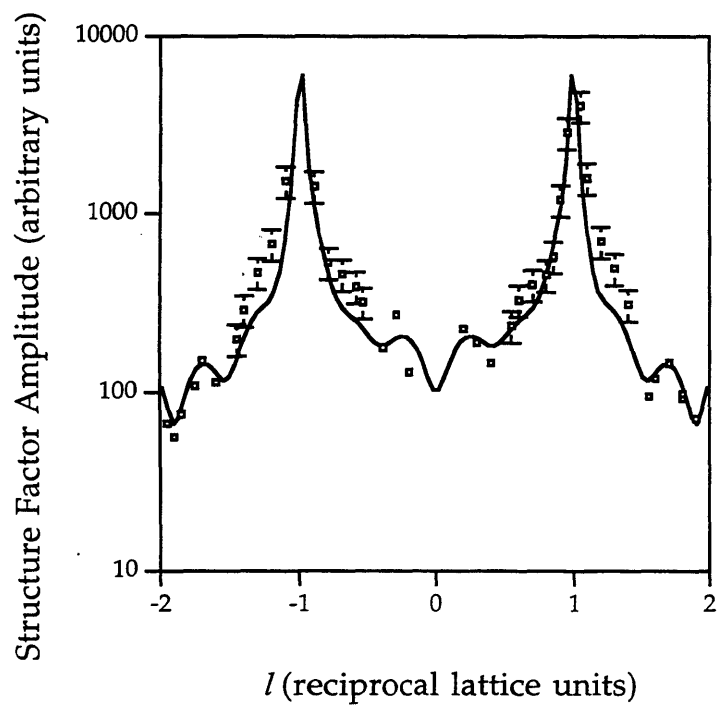


Figure 7.9. (10l) rod for the 4ML coverage deposited with the substrate held at 300K. The solid line shows the best fit to the data.

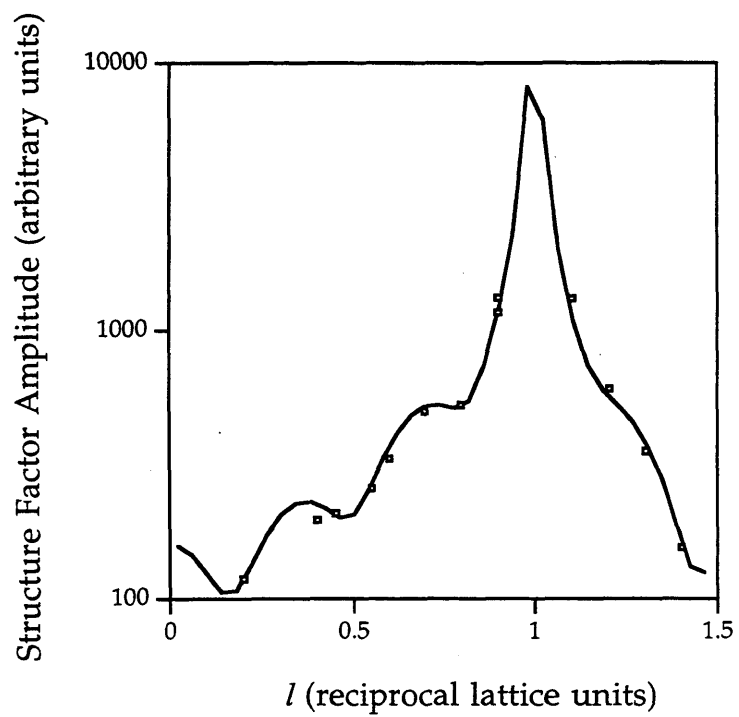


Figure 7.10. (10l) rod for the 6.2ML coverage deposited with the substrate held at 300K. The solid line shows the best fit to the data.

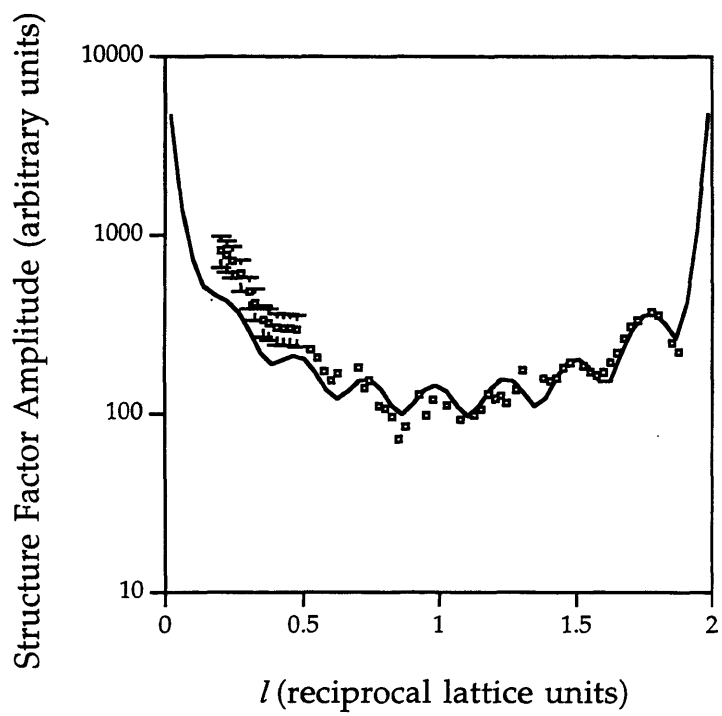


Figure 7.11. (111) rod for the 8ML coverage deposited with the substrate held at 300K. The solid line shows the best fit to the data.

7.4.4 The Stability of the 4ML Structure Grown at 100K

The room temperature growth curves show that the growth proceeds in a layer-by-layer mode. Previous work has shown that when Fe is grown at low temperature significant islanding of Fe is observed (James *et al* 1995). It would be interesting to see how stable a film grown at low temperature is with temperature.

A 4ML coverage was grown with the substrate held at 100K. Following this the (11 $\bar{1}$) rod was measured whilst the sample was still at a temperature of 100K. The sample was then annealed to 300K and the (11 $\bar{1}$) rod was measured again. Since no real change occurred in the measured rod a further anneal to 400K was done. The sample was then cooled down to 300K and the (11 $\bar{1}$) rod was measured. All of these rods are shown in figure 7.12 along with the equivalent rod taken after growth of a 4ML coverage with the substrate held at 300K.

7.5 Discussion

The *in-situ* growth scans show that growth proceeds as a layer-by-layer mode. No evidence of bilayer growth is seen. The difference in the (100) and (001) intensities show that not all of the atoms sit in epitaxial positions on the Cu(001) surface. Analysis of the (1 0 0.085) peak shows that the correlation length as well as the peak height oscillate. They both oscillate in-phase with each other and the maxima coincide with the completion of successive layers. The fact that the correlation length reaches a maximum at layer completion shows that the layers may grow initially with some lateral disorder but as more atoms are deposited they become more ordered. However, since no diffuse scattering around the peaks could be seen the changes in the width of the (1 0 0.085) peak may just reflect changes in its height.

No bcc relaxation was seen up to coverages of 6ML disagreeing with the results of Thomassen *et al* (1992) and Wuttig *et al* (1993) who saw a structural stability as low as 4.6ML. No fcc relaxation was seen either, indicating that the tetragonally distorted fcc structure is stable up to 6ML.

Only the fit to the rod scan for the lowest coverage of 4ML was improved significantly by introducing intermixing as an extra parameter. The high value of

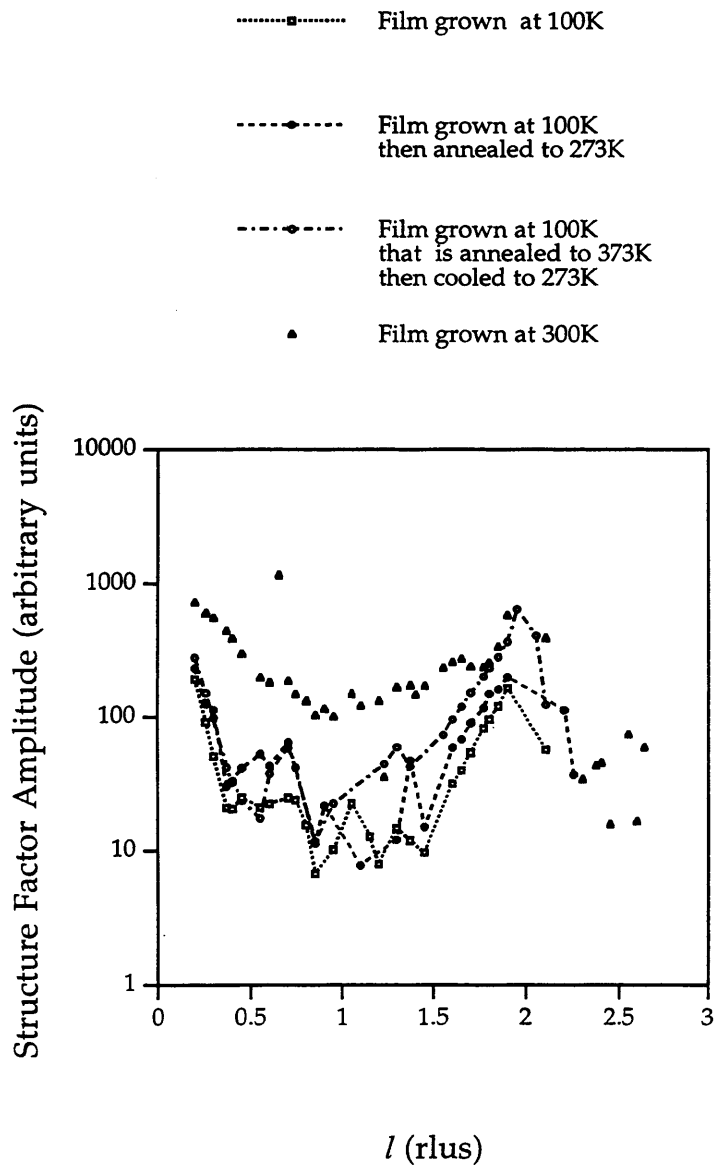


Figure 7.12. (111) rods for four different coverages.

75% indicates the importance of including this. This implies that at a further coverage of an extra 2.2ML making a coverage of 6.2ML the interface region is no longer intermixed or at least the intermixing as been significantly reduced so that it is undetectable. The structure, therefore, reorders itself between 4ML and 6.2ML resulting in a sharp interface.

The expansion of the top interlayer spacings could be due to the fcc relaxation. Since the nearest neighbour distance of fcc Fe (2.54\AA) is lower than that of Cu (2.56\AA) the in-plane lattice spacing of the fcc Fe is stretched and the out-of-plane spacing correspondingly contracts to preserve the atomic volume and producing an fct structure. However, relaxation to the fcc phase will result in an expansion of 0.02\AA . The only comparable expansion is that for the 8ML coverage. Magnetic effects may also play a role in expanding the layers further. An increase in the magnetic moment, for instance, is associated with an increase in the atomic volume. The expansion at the interface may also be due to magnetic effects but could also be due to the mutual immiscibility of the Fe and Cu atoms. Since they are sharing the same surface they may maximise the distance between them by increasing the spread of heights in the layer and thus increasing the average height of the layer.

Since there were no significant changes in the (11 $\bar{1}$) rod for 4ML film grown at low temperature when it was annealed to 300 and 400K this coverage must be remarkably stable. No expected reordering of the film occurs and none of the rods compare very well to the (11 $\bar{1}$) rod of the 4ML film grown at 300K.

7.6 Conclusion

The growth mode of Fe on Cu(001) is layer-by-layer with intermixing at the interface which is reduced with coverage. By a coverage of 6.2ML the intermixing is no longer detectable. No bilayer growth was detected.

No relaxation of the tetragonally strained fcc structure to the fcc or bcc phases was found up to a coverage of 6ML.

The calculated correlation length oscillates such that the maxima coincide with the completion of each layer indicating that growth of each layer begins fairly disordered but gradually becomes more ordered as more atoms occupy the layer. However, since no scattering could be seen around the (1 0 0.085) reflection

the correlation length was calculated from the width of this peak and not the diffuse scattering. The change in width and, therefore, the change in the correlation length could be due to changes in the height of the peak.

Out-of-plane expansions have been found in the top layers of all of the coverages. Only the 8ML expansion could possibly be due to the fcc relaxation alone. The magnetism of the layers could therefore play an important role in the structure of the films. Expansions at the interface could also be due to magnetic effects although the immiscibility of the two atomic species may also expand the layer spacings in this intermixed region.

A 4ML coverage grown at low temperature has been found to be very stable when annealed to 300 and 400K. This structure is very different to that of the 4ML coverage grown with the substrate held at 300K.

Chapter 8

Summary and Suggestions for Future Work

8.1 Introduction

Surface X-ray Diffraction has been used throughout this thesis to study the systems Cr on Cu(001), Cr on Ag(001) and Fe on Cu(001). Auger electron spectroscopy (AES) was also used to monitor the substrate surfaces for contamination. In this way the cleanliness of the substrates could be checked before deposition of the adsorbate material as the growth mode may depend heavily on the impurity level. Rutherford Back Scattering (RBS) was employed *ex-situ* for coverage calibration. Sections 8.2, 8.3 and 8.4 summarise the important results from the Cr on Cu(001), Cr on Ag(001) and Fe on Cu(001) systems respectively. Finally section 8.5 presents some suggestions for future work.

8.2 The Growth and Structure of Cr on Cu(001)

Previous work on Cr on Cu(001) is controversial. The possibility of stabilising the high temperature fcc phase of Cr on Cu(001) is one reason why there is an interest in the system. The majority of previous work has however shown that a highly disordered bcc phase is supported on Cu(001) with the Cr(110) planes parallel to the Cu(001) surface. The experimental results, presented in chapter 5, demonstrate the power of SXRD for determining growth modes and structures even when an overlayer consists of disordered islands.

The antiphase (001) point of reciprocal space was monitored during growth. The featureless decay, exhibited at all substrate temperatures, is ascribed to a disordered growth mode. The growth performed at 100K and 300K gave a rapid decay of the (001) intensity. At higher temperatures the decay rate was found to decrease. By using kinematical theory it was found that the growths at 100 and 300K follow a random deposition model where there is no surface diffusion and the atoms just stick to the closest epitaxial position on the surface. The growth is therefore diffusion limited. The decreased fall off of the intensity at higher

temperatures is due to an increase in surface diffusion allowing interlayer mass transport.

By measuring the in-plane reflections along chosen direction in reciprocal space the growth of a thick film was found to grow with Cr(110) parallel to Cu(001) and Cr[1 $\bar{1}$ 1] parallel to Cu[$\bar{1}$ 10] along with the other orientations predicted from the 4mm symmetry operations. This agrees well with previous work. By fitting a Lorentzian curve to the (1 0.72) peak the correlation lengths were found to be 50.5Å, along h , and 12.3Å, along k , respectively. This is comparable with island sizes found by Lawler *et al* (1996). The anisotropy of the island size could be due to the terrace size on a stepped surface.

The specular reflectivities from a 0.5 and 1.0ML film, grown at room temperature, were measured. Four different models were used to fit the data: Robinson's beta roughness model (Robinson 1986), a Poisson model, a linear model and a sinusoidal model. For the 0.5ML coverage only the roughness parameter significantly decreased the χ^2 . All of the models described the data equally well giving similar rms roughness values. For the 1.0ML coverage the linear and sinusoidal models give the best results. The fits are significantly improved if the interlayer distances are used as fit parameters. Such a procedure yields a large interface spacing which could be magnetically driven or maybe simply due to the different electronic environment at the interface.

8.3 The Epitaxial Growth of Cr on Ag(001)

It has previously been shown for Fe on Cu(001) that SXRD is a powerful technique for measuring the exact stoichiometry of the surface (James 1995) as well as determining interatomic distances and growth modes. Although the bcc Cr lattice is well matched to the fcc Ag(001) surface if it is rotated by 45° the surface free energies of the substrate and adsorbate make it unlikely that a flat Cr layer will form on the Ag(001) surface.

The evolution of the (001) intensity during growth is very sensitive to temperature. At 100K rapidly decaying oscillations are indicative of a poorly defined layer-by-layer growth mode whereas at 300K a featureless decay is attributed to a disordered growth mode. At higher temperatures there is an initial

rise in intensity the maximum increasing with increasing temperature. Using kinematical theory, it has been demonstrated that the maximum occurs because the overlayer film has Ag mixed with it. The exact height of the initial maximum has been shown to be very sensitive to the amount of Ag in the top layer of an intermixed layer. Since intermixing predicts an initial decay before the maximum it does not describe the initial rise seen in the data. It has been shown that coating of Cr layers by Ag, which predicts an initial rise, is a more likely scenario.

Three coverages were measured being chosen due to the features that occur in the growth curves. The first and second maximum in the low temperature curve and the maximum at 440K were chosen as stopping points for the growth.

The ratio of the times that the first and second maxima occur at 100K is 2:5 suggesting that they correspond to 2 and 5ML. The prediction for the (001) intensity for layer-by-layer growth with an expanded interface spacing gives very low maxima at 1, 3 and 4ML implying that they would not be seen in a real experiment. Since the growth at 100K is not perfect layer-by-layer a sensible function needed to be chosen that fixed the occupancies in each layer of the model. The Fermi function was found to be suitable. Using this function and then fitting to the specular rod data large interface spacings were found as predicted by the growth analysis. The best fits to the (110) and (100) rods were different. To fit these the layer occupancies were multiplied by a constant factor: 0.5 for the 2ML coverage and 0.8 for the 5ML coverage thus indicating that only 50 and 80% of the atoms are in epitaxial positions in the 2 and 5ML coverages respectively.

Growth to the maximum at a substrate temperature was found, by Rutherford Back Scattering (RBS) analysis, to correspond to 1.0 ML. The best fit to the specular rod data corresponded to a Cr film which had intermixed with the top layer of the Ag substrate. The best fit was achieved with a percentage of Ag in the top layer and therefore percentage of Cr in the original top layer of the substrate of 78 ± 13 . The atoms in these two layers were found to have an expanded volume possibly linked to giant magnetic moments. The fact that the adsorbate atoms mix with the substrate tells us that the growth mode must be quite complex. Whereas the (001) intensity during growth is described well by a model involving coating of Cr layers by Ag intermixing is also taking place.

8.4 The Growth and Structure of Fe on Cu(001)

From the evolution of the (001) intensity, which exhibits parabolic oscillations, it can be concluded that Fe grows on Cu(001) in a layer-by-layer fashion. The (100) intensity also oscillates in phase with the (001) but it decays much faster initially. This is due to some of the atoms in the film occupying non-epitaxial positions. No growth mode that begins with the formation of a bilayer was found.

The diffuse scattering around the in-plane (1 0) position of reciprocal space gives information on the correlation length of the overlayer. No diffuse scattering could be seen in this experiment so the width of the (1 0) peak was used to calculate the correlation length. The resulting correlation length oscillated in phase with the height of the (1 0 0.085) peak. This could be due to the Fe islands ordering at the completion of each layer but it could reflect changes in the height of the peak.

By scanning close to the in-plane (2 0) position it is possible to determine if the Fe film has relaxed from a tetragonally distorted fcc structure to its fcc structure or even to its more commonly known bcc structure. No relaxation to the fcc or bcc structure of Fe was found.

From scanning crystal truncation rods for a 4, 6.2 and 8ML film it has been found that the top interlayer distance is expanded compared to a model that uses the fcc Fe atomic radius. This expansion could be due to enhanced magnetism. Expansions have also been found at the interface. For the 4ML film intermixing between the bottom layer of the film and the top layer of the substrate was found to be 75%. No intermixing was found for the 6.2 and 8ML films suggesting that the interface becomes sharper during growth from 4 to 6.2 ML.

By comparing crystal truncation rods it has been found that a 4ML coverage grown at 100K is remarkably stable to annealing up to 300 and 400K. The structure of the film differs from that of a 4ML coverage grown at 300K.

8.5 Suggestions for Future Work

Previous work using SXRD, including the work in this thesis, shows that it is a powerful technique in studying surface and interface structures. The

sensitivity of the X-ray intensity to the growth mode has been demonstrated in the systems studied in this thesis which include layer-by-layer, islanding and alloying of the substrate and adsorbate atomic species. The sensitivity of the X-ray scattering to stoichiometry is most noticeable in systems where there is a large difference in the atomic number of the elements e.g. in Cr and Ag which have atomic numbers of 24 and 47 respectively.

The high intensity and high brilliance of the ESRF and other new synchrotron radiation sources enable additional work to be done in this field. Typical growth rates in an experiment involve growing a monolayer every 10 minutes. With higher intensity growth rates could be increased so that the growth mode could be measured as a function of deposition rate. The results from such an experiment could explain why there are so many contradictory results for the same system. In addition systems could be measured whilst being grown at the fast rates used in fabricating electronic devices. Another possibility is the measurement of the weak diffuse scattering which provides information about island size and distribution.

Currently beamtime at the ESRF is limited. To further work in this field a UK facility is needed with higher intensity than can be provided by the existing source at Daresbury. One possibility is for a grazing incidence diffractometer station to be added to the planned multipole wiggler on line 6 at Daresbury. Another option involves the proposed storage ring Diamond.

Since X-rays are not limited to the solid vacuum interface the change in structure of a surface could be measured as a function of gas pressure. Such an experiment would, however, need a high pressure vacuum chamber. This would not be possible for techniques which employ low energy electrons since they need a high vacuum environment.

The work in this thesis has shown the existence of two surface alloy systems: high temperature growth of Cr on Ag(001) and room temperature growth of Fe on Cu(001). Other possibilities involve the ordered alloy systems Mn on Cu(001), Pd on Cu(001) and Au on Cu(001). A full out-of-plane analysis could accurately measure the outward relaxation of the corrugations in the alloy layer. The latter two are particularly attractive due to the difference in the atomic numbers of the two atomic species. Au grown on Ni(110) is also a possibility where the difference in atomic number is advantageous. There is no evidence of any ordering of the alloy structure but measurements of reflectivity and crystal

truncation rods would allow an accurate determination of the degree of intermixing and the relaxations of the layers perpendicular to the surface.

Appendix A

The Simplification of Equation 3.17.

It was mentioned in chapter 3 that equation 3.17 i.e.

$$E_i(\mathbf{r}) + E_s(\mathbf{r}) = E_0 e^{-ik_i \cdot \mathbf{r}} - r_e E_0 \int \frac{e^{-ik|\mathbf{r}-\mathbf{r}'|}}{|\mathbf{r}-\mathbf{r}'|} \rho(\mathbf{r}') e^{-ik_i \cdot \mathbf{r}'} d\mathbf{r}' \quad (\text{A1})$$

could be simplified. To do this we make use of the experimental situation where the point of observation will be at a distance large compared with the dimensions of the sample. The experimental geometry is shown in figure A1. We can approximate the Green's function exponential since we know r' is small.

$$|\mathbf{r}-\mathbf{r}'| = (r^2 + r'^2 - 2\mathbf{r} \cdot \mathbf{r}')^{1/2} = (r^2 - 2\mathbf{r} \cdot \mathbf{r}')^{1/2} \quad (\text{A2})$$

and then use the binomial expansion

$$|\mathbf{r}-\mathbf{r}'| = r \left(1 - \frac{2\mathbf{r} \cdot \mathbf{r}'}{r^2}\right)^{1/2} = r \left(1 - \frac{2r' \cos \theta}{2r}\right) = r - r' \cos \theta \quad (\text{A3})$$

so that

$$k|\mathbf{r}-\mathbf{r}'| = kr - kr' \cos \theta \quad (\text{A4})$$

where θ is the angle between \mathbf{r} and \mathbf{r}' . If we define \mathbf{k}_r to be a vector in the same direction as \mathbf{r} with magnitude k then

$$k|\mathbf{r}-\mathbf{r}'| = kr - \mathbf{k}_r \cdot \mathbf{r}' \quad (\text{A5})$$

If we substitute this result into equation (3.19) and ignore the last term for the denominator of the Green's function then we get

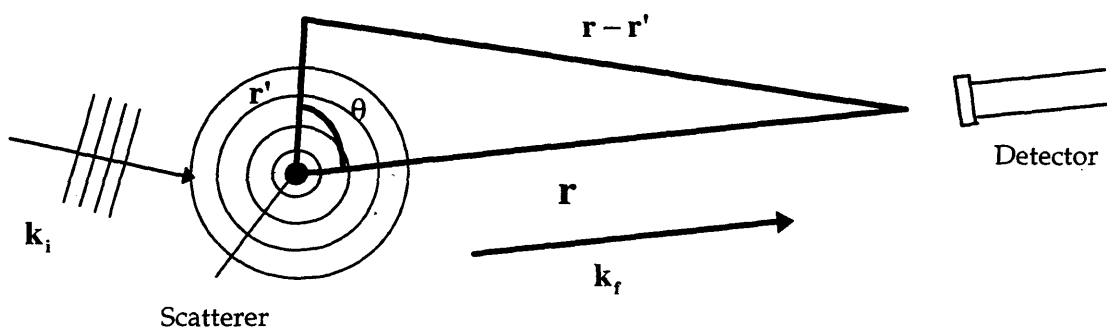


Figure A1. The relationship between the vectors \mathbf{k}_i , \mathbf{k}_f , \mathbf{r} and \mathbf{r}' .

$$E_i(\mathbf{r}) + E_s(\mathbf{r}) = E_0 e^{-i\mathbf{k}_i \cdot \mathbf{r}} - r_e E_0 \frac{e^{-i\mathbf{k}_f \cdot \mathbf{r}}}{r} \int e^{i\mathbf{k}_f \cdot \mathbf{r}'} \rho(\mathbf{r}') e^{-i\mathbf{k}_i \cdot \mathbf{r}'} d\mathbf{r}' \quad (\text{A6})$$

so that we obtain equation 3.18.

$$E_s(\mathbf{r}) = -r_e E_0 \frac{e^{-i\mathbf{k}_f \cdot \mathbf{r}}}{r} \int e^{i\mathbf{q} \cdot \mathbf{r}'} \rho(\mathbf{r}') d\mathbf{r}' \quad (\text{A7})$$

where $\mathbf{q} = \mathbf{k}_f - \mathbf{k}_i$ the momentum transfer vector, and \mathbf{k}_i and \mathbf{k}_f are the incident and scattered wave vectors.

Appendix B

Evaluation of the Area Element in Terms of the Miller Indices.

In deriving the integrated intensity it is useful to express the area element in terms of the Miller indices (see chapter 3). Treating the Miller indices as continuous an area element in reciprocal space will have the form

$$dA = |\mathbf{b}_1 \times \mathbf{b}_2| dhdk \quad (\text{B1})$$

Using the definitions of the reciprocal lattice given by (3.38)

$$dA = 4\pi^2 \left| \frac{(\mathbf{a}_2 \times \mathbf{a}_3) \times (\mathbf{a}_3 \times \mathbf{a}_1)}{(\mathbf{a}_1 \cdot \mathbf{a}_2 \times \mathbf{a}_3)^2} \right| dhdk \quad (\text{B2})$$

and then making use of the vector identity

$$\mathbf{A} \times (\mathbf{B} \times \mathbf{C}) = \mathbf{B}(\mathbf{A} \cdot \mathbf{C}) - \mathbf{C}(\mathbf{A} \cdot \mathbf{B}) \quad (\text{B3})$$

will yield

$$dA = 4\pi^2 \left| \frac{\mathbf{a}_3(\mathbf{a}_2 \times \mathbf{a}_3 \cdot \mathbf{a}_1) - \mathbf{a}_1(\mathbf{a}_2 \times \mathbf{a}_3 \cdot \mathbf{a}_3)}{(\mathbf{a}_1 \cdot \mathbf{a}_2 \times \mathbf{a}_3)^2} \right| dhdk \quad (\text{B4})$$

Since $\mathbf{a}_2 \times \mathbf{a}_3 \cdot \mathbf{a}_3 = 0$ and observing the cyclic order of the triple product so that $\mathbf{a}_1 \cdot \mathbf{a}_2 \times \mathbf{a}_3 = \mathbf{a}_3 \cdot \mathbf{a}_1 \times \mathbf{a}_2$ we obtain

$$dA = \frac{4\pi^2}{|\mathbf{a}_1 \times \mathbf{a}_2|} dhdk \quad (\text{B5})$$

but the denominator is the area of the unit cell A_u . So that equation (B1) can be rewritten as

$$dA = \frac{4\pi^2}{A_u} dhdk$$

(B6)

Appendix C

Publications and Reports

Publications

Relaxation of TiO₂(110) - (1x1) using Surface X-ray Diffraction

G. Charlton, P. B. Howes, C. L. Nicklin, P. Steadman, J. S. G Taylor, C. A. Muryn, S. P. Harte, J. Mercer, R. McGrath, D. Norman, T. S. Turner and G. Thornton, Phys. Rev. Lett. 78 (1997) 495-498

The Growth of Sm on Mo(110) Studied by Surface X-ray Diffraction

C. L. Nicklin, C. Norris, P. Steadman, J. S. G. Taylor and P. B. Howes, Physica B 221 (1996) 86-89

Oxygen Modified Growth of Gd on(110)

S. N. Mozley, C. L. Nicklin, M. A. James, P. Steadman, C. Norris and M. Lohmeier, Surf. Sci. 331-333 (1995) 961-964

The Growth and Atomic Structure of 3d Metal Films on GaAs(001)

M. A. James, C. Norris, C. L. Nicklin, P. Steadman, R. G. van Silfhout and P. B. Howes,
To be published

Interdiffusion and Roughening of Ultrathin Films of Cr on Ag(001)

P. Steadman, C. Norris, C. L. Nicklin, N. Jones, S. A. de Vries, J. S. G. Taylor and S. L. Bennett
To be published

The growth and Structure of Cr on Cu(001)

P. Steadman, C. Norris, C. L. Nicklin, N. Jones, G. Charlton, J. S. G. Taylor and S. L. Bennett

To be published

Reports

Oxygen Modified Growth of Gd on Mo(110)

S. N. Mozley, C. L. Nicklin, M. A. James, P. Steadman, C. Norris and M. Lohmeier,

Daresbury Annual Report 1994/95 p. 650-651

The Growth of Sm on Mo(110) Studied by Surface X-ray Diffraction

C. L. Nicklin, C. Norris, P. Steadman and J. S. G. Taylor,

Daresbury Annual Report

Surface Reconstructions of InSb(001)

N. Jones, C. Norris, C. L. Nicklin, P. Steadman, S. H. Baker, J. S. G. Taylor, A. D. Johnson and M. S. Finney

Daresbury Annual Report

Stabilisation of 3d Metal Overlayers on GaAs(001)

M. A. James, C. Norris, C. L. Nicklin, P. Steadman, R. G. van Silfhout, A. D. Johnson and T. S. Turner,

Daresbury Annual Report 1994/95 p. 644-645

The Epitaxial Growth of Cr on Ag(001)

P. Steadman, C. Norris, C. L. Nicklin, N. Jones, J. S. G. Taylor, S. de Vries and S. L. Bennett

Daresbury Annual Report

References

- Abu-Joudeh, M. A., Davies, B. M. and Montano, P. A., *Surf. Sci.* **171** (1986) 331-348
- Alkemade, P. F. A., Turkenburg, W. C. and van der Weg, W. F., *Nucl. Instrum. Methods* **B15** (1986) 126-129
- Alan, G., *Surf. Sci.* **74** (1978) 79-88
- Alan, G., *Phys. Rev.* **B19** (1979) 4774-4779
- Alan, G., *Phys. Rev.* **B44** (24) 13641-13644
- Allenspach, R. and Bischof, A., *Phys. Rev. Lett.* **69** (1992) 3385
- Arndt, U. W. and Willis, B. T. M., *Single Crystal Diffractometry* (Cambridge 1960)
- Arnott, M., McCash, E. M. and Allison, W., *Surf. Sci.* **269/270** (1992) 724-730
- Bacon, G. E., *Acta Cryst.* **14** (1961) 823-829
- Bader, S. D. and Moog, E. R., *J. Appl. Phys.* **61** (8) (1987) 3729-3734
- Bader, S. D., Moog, E. R., Montano, P. A., Zajac, G. and Fleisch, T. H., *Superlatt. Microstruct.* **3** (1987b) 4
- Bauer, E., *Z. Kristallogr.* **110** (1958) 372
- Baynham, D. E., Clee, P. T. M. and Thompson, D. J., *Nucl. Instr. Meth.*, **152** (1978) 31-35
- Blugel, S., *Phys. Rev. Lett* **68** (6) 1992 851-854
- Blume, M., *J. Appl. Phys.* **57** (1985) 3615-3618

Brodsky, M. B., J. Appl. Phys. **52** (3) (1981) 1665-1669

Bruckel, T., Lippert, M., Bouchard, R., Schmidt, T., Schneider, J. R. and Jauch W., Acta Cryst. **A49** (1993) 679-682

Chambers, S. A., Wagener, T. J. and Weaver, J. H., Phys. Rev. **B36** (1987) 8992-9002

Chambliss, D. D., Johnson, K. E., Wilson, R. J. and Chiang, S., J. Mag. Magn. Mat. **121** (1993) 1-9

Chen, C. H. and Sansalone, F. J., Surf. Sci. **164** (1985) L688

Clark, A., Rous, P. J., Arnott, M., Jennings, G. and Willis, R. F., Surf. Sci. **192** (1987) L843-L848

Cowley, J. M., *Diffraction Physics* (North-Holland, Amsterdam, 1984)

Dastoor, P., Arnott, M., McCash, E. M. and Allison, W., Surf. Sci. **272** (1992) 154-160

Davis, H. L. and Noonan, J. R., J. Vac. Sci. Technol. **20** (1982) 842-845

Davis, H. L. and Noonan, J. R., Surf. Sci. **126** (1983) 245-252

Detzel, Th., Memmel N. and Fauster, Th., Surf. Sci. **293** (1993) 227-238

Dongqi, Li., Freitag, M., Pearson, J., Qui, Z. Q., Bader, S. D. and Bader S. D., Phys. Rev. Lett. **72** (1994) 3112-3115

Feidenhans'l, R., Surf. Sci. Rep. **10** (1989) 105

Finney, M. S., *The Growth and Atomic Structure of the Si(111)-Indium Interface Determined by Surface X-ray Diffraction*, PhD Thesis, University of Leicester (1992).

Finney, M. S., Norris, C., Howes, P. B. and Vlieg, E., Surf. Sci. **277** (1992) 330-336

Finnis, M. W. and Heine, V., J. Phys. **F4** (1974) L37

Flores, T., Hansen, M. and Wuttig, M., Surf. Sci. **279** (1992) 251-264

Foiles, S. M., Baskes, M. I. and Daw, M. S., Phys. Rev. **B33** (1986) 7983-7991

Freeman, A. J. and Fu, C. L., J. Appl. Phys. **61** (8) (1987) 3356-3361

Freeman, A. J. and Ru-qian Wu, J. Magn. Magn. Mat. **100** (1991) 497-514

Fu, C. L., A. J. Freeman and Oguchi T., Phys. Rev. Lett. **54** (1985) 2700-2703

Fuoss, P. H. and Robinson, I. K., Nucl. Instr. Meth. **222** (1984) 171-176

Germar, R., Durr, W., Krewer, J. W., Pescia, D. and Gudat, W., Appl. Phys. **A47** (1988) 393

Giergiel, J., Kirschener, J., Landgraf, J., Shen, J. and Woltersdorf, J., Surf. Sci. **310** (1994) 1-15

Glatzel, H., Fauster, T., Scherzer, B. M. U. and Dose, V., Surf. Sci. **254** (1991) 58-64

Grempel, D. R., Phys. Rev. **B24** (7) (1981) 3928-3938

Haase, O., Z. Naturforsch **11-A** (1956) 862

Hanf, M. C., Pirri C., Peruchetti, J. C., Bolmont, D. and Gewinner, G., Phys. Rev. **B39** (3) 1989 1546-1556

Hansen, M., *Constitution of Binary Alloys* (McGraw Hill, New York, 1958).

Haughan, M. E., Chen, Q., Onellion, M. and Himpsel, F. J., Phys. Rev. **B49** (19) (1994) 14028-14031

International Tables for X-ray Crystallography, vol. III eds. Macgillavry, C. H. and Rieck, G. D. (Reidel, Dordrecht,1983); *id. Vol. IV*, eds. Ibers, J. A. and Hamilton, W. C. (Kynoch Press, Birmingham 1974)

James, M. A., *The Epitaxial Growth and Structure of Metal Overlayers on Oriented Substrates Studied by Surface X-ray Diffraction*, PhD Thesis, University of Leicester (1995)

Jandeleit, J., Gauthier, Y. and Wuttig, M., Surf. Sci. **319** (1994) 287-297

Jesser, W. A. and Matthews, J. W., Philos. Mag. **15** (1967) 1097

Jesser, W. A. and Matthews, J. W., Philos. Mag. **17** (1968) 595

Jiang, Q. T., Fenter, P. and Gustafsson, T., Phys. Rev. B **44** (1991) 5773-5778

Johnson, A. D., Bland, J. A. C., Norris, C. and Lauters, H., J. Phys. C: Solid State Phys. **21** (1988) L899-L904

Johnson, K. E., Chambliss, D. D., Wilson, R. J. and Chiang. S., J. Vac. Sci. Technol. **A11** (1993) 1654-1660

Johnson, K. E., Chambliss, D. D., Wilson, R. J. and Chiang. S., Surf. Sci. **313** (1994) L811-L816

Jona, F., J. Phys. **11** (1978) 4271

Kerker, G. P., Ho, K. M. and Cohen, M. L., Phys. Rev. Lett. **40** (1978) 1593

Klebanoff, L. E., Robey, S. W., Liu, G., and Shirley, D. A., Phys. Rev. **B30** (1984) 1048-1051

Klebanoff, L. E., Victoria, R. H., Falicov, L. M. and Shirley, D. A., Phys. Rev. **B32** (4) (1985) 1997-2005

Krembel, C., Hanf, M. C., Peruchetti, J. C., Bolmont, D. and Gewinner, G., J. Magn. Magn. Mat. **93** (1991a) 529-533

Krembel, C., Hanf, M. C., Peruchetti, J. C., Bolmont, D. and Gewinner, G., J. Vac. Sci. Technol. **A 10** (5) (1992a) 3325-3332

Krembel, C., Hanf, M. C., Peruchetti, J. C., Bolmont, D. and Gewinner, G., Phys. Rev. **B 44** (15) (1991b) 8407-8410

Krembel, C., Hanf, M. C., Peruchetti, J. C., Bolmont, D. and Gewinner, G., Phys. Rev. **B 44** (20) (1991c) 11472-11481

Krembel, C., Hanf, M. C., Peruchetti, J. C., Bolmont, D. and Gewinner, G., Solid State Comm. **81** (2) (1992b) 219-222

Kyuno, K., Hara, S., Kaneko, T. and Yamamoto, R., J. Phys: Condens. Matter **4** (1992) 5125-5136

Lawler, J. F., van der Kraan, R. G. P., van Kempen, H. and Quinn, A. J., Phys. Rev. **B 53** (16) (1996) 11159-11163

Lind, D. M., Dunning, F. B., Walters, G. K. and Davis, H. L., Phys. Rev. **B35** (17) (1987) 9037-9044

Liu, C., Moog, E. R. and Bader, S. D., Phys. Rev. Lett. **60** (23) (1988) 2422-2425

Lohmeier, M. and Vlieg, E., J. Appl. Cryst., **26** (1993) 706-716

Lohmeier, M., de Vries, S., Custer, J. S., Vlieg, E., Finney, M. S., Priolo, F. and Battaglia, A., Appl. Phys. Lett., **64**, (1994) 1803-1805

Macedo, W. A. A., Keune, W. and Ellerbrock, E. D., *J. Magn. Magn. Mater.* **93** (1991) 552

Magnan, H., Chandesris, D., Villette, B., Heckmann, O. and Lecante, J., *Phys. Rev. Lett.* **67** (1991a) 859-862

Magnan, H., Chandesris, D., Villette, B., Heckmann, O. and Lecante, J., *Surf. Sci.* **251** (1991b) 597-601

Miedema, A. R., *Z. Metallk.* **69** (1978) 455

Ming J., Zhu, D. M. Bylander and Kleinman, L., *Phys. Rev.* **B43** (5) (1991) 4007-4010

Mizuno, S., Tochihara, H. and Kawamura, T., *Surf. Sci. Lett.* **292** (1993) L811-L816

Moruzzi, V. L. and Marcus P. M., *Handbook of Ferromagnetic Materials*, 2nd ed. (Elsevier, New York, 1990)

Moruzzi, V. L. and Marcus P. M., *Phys. Rev.* **B38** (1988) 1613-1620

Moruzzi, V. L. and Marcus P. M., *Phys. Rev.* **B39** (1989) 6957

Müller, S., Bayer, P., Kinne, A., Schmailzl, P. and Heinz, K., *Surf. Sci.* **322** (1995) 21-33

Newstead, D. A., Norris, C., Binns, C., and Stephenson, P. C., *J. Phys. C: Solid State Phys.* **20** (1987) 6245-6254

Newstead, D. A., *Photoelectron Spectroscopy of Ultrathin Metallic Layers*, PhD Thesis, University of Leicester (1987).

Norris, C., *Phil. Trans. R. Soc. Lond. A* **344** (1993) 557-566

Norris, C., Finney, M. S., Clark, G. F., Baker, G., Moore, P. R. and van Silfhout, R., *Rev. Sci. Instrum.* **63** (1992) 1083-1086

Norris, C., Taylor, J. S. G., Moore, P. R., Harris, N. W. and Miller, M., *Daresbury Annual Report (1986/7)* 124

Ortega, J. E. and Himpsel, F. J., *Phys. Rev. B* **47** (24) (1993) 16441-16446

Patrician, T. J. and Wyman, C. M., *Phys. Stat. Sol. A* **6** (1971) 449

Pearson, W. B., *A Handbook of Lattice Spacings and Structures of Metals and Alloys*, (Pergamon, New York, 1958) p. 627.

Pendry, J. B., *Low Energy Electron Diffraction: the theory and its Application to Determination of Surface Structure*, (Academic Press, London 1974)

Pescia, D., Stapanoni, M., Bona, G. L., Vaterlaus, A., Willis, R. F. and Meier, F., *Phys. Rev. Lett.* **58** (1987) 2126

Pleth Nielsen, L., Besenbacher, F., Stensgaard, I., Laegsgaard, E., Engdahl, C., Stoltze, P., Jacobsen, K. W. and Nørskov, J. K., *Phys. Rev. Lett.* **71** (1993) 754-757

Posternak, M., Krakauer, H., Freeman, A. J., and Koelling D. D., *Phys. Rev.* **B21** (1980) 5601

Prinz, G. A., *J. Magn. Magn. Mat.* **100** (1991) 469-480

Rawlings, K. J. and Dobson, P. J., *Thin Solid Films* **67** (1980) 171

RBS analysis was carried out by C. Jeynes and N. Barradas at the University of Surrey, England.

Robinson, I. K., *Phys. Rev.* **B33** (6) (1986) 3830-3836

- Robinson, I. K. and Tweet, D. J. *Rep. Prog. Phys.* **55** (1992) 599
- Rouyer, D., Krembel, C., Hanf, M. C., Bolmont, D. and Gewinner, G., *Surf. Sci.* **287-288** (1993) 935-940
- Rouyer, D., Krembel, C., Hanf, M. C., Bolmont, D. and Gewinner, G., *Surf. Sci.* **307-309** (1994) 477-482
- Rouyer, D., Krembel, C., Hanf, M. C., Bolmont, D. and Gewinner, G., *Surf. Sci.* **331-333** (1995) 957-960
- Rouyer, D., Krembel, C., Hanf, M. C., Peruchetti, J. C., Bolmont, D. and Gewinner, G., *Surf. Sci.* **322** (1995b) 34-40
- Schatz, A., Dunkhorst, S., Lingnau, S., Vonhorsten, U. and Keune, W., *Surf. Sci.* **310** (1994) L595-L600
- Schmitz, P. J., Leung W.-Y., Graham G. W. and Thiel, P. A., *Phys. Rev.* **B40** (1989) 11477-11487
- Smoluchowski, R., *Phys. Rev.* **60** (1941) 661
- Steigerwald, D. A. and Egelhoff, W. F., *Surf. Sci.* **192** (1987) L887-L892
- Steigerwald, D. A., Jacob, I. and Egelhoff, W. F., *Surf. Sci.* **202** (1988) 472-492
- Stearns, D. G., *J. Appl. Phys.* **65** (2) (1989) 491-506
- Takahashi, T., and Basset, W. A., *Science* **145** (1964) 483
- Taylor, J. S. G. and Norris, C., *A Two Stage Differentially Pumped Rotary Seal for Surface X-ray Diffraction*. CMP Group Internal Report, Department of Physics and Astronomy, University of Leicester (1991).

Taylor, J. S. G. and Norris, C., *A Liquid Helium Cooled Sample Holder Assembly for Surface X-ray Diffraction*, CMP Group Internal Report, Department of Physics and Astronomy, University of Leicester (1994).

Taylor, J. S. G. and Norris, C., *Rev. Sci. Instrum.* **68** (1997) 3256-3257

Taylor, J. S. G., Norris, C., Vlieg, E., Lohmeier, M. and Turner, T. S., *Rev. Sci. Instrum.* **67** (1996) 2658-2659

Thomassen, J., May, F., Feldmann, B., Wuttig, M. and Ibach, H., *Phys. Rev. Lett.* **69** (1992) 3831

Thomassen, J., Feldman, B. and Wuttig, M., *Surf. Sci.* **264** (1992) 406-418

Thomassen, J., May, F., Feldman, B., Wuttig, M. and Ibach, H., *Phys. Rev. Lett.* **69** (1992) 3831

Tosatti, E., *Solid State Commun.* **25** (1978) 637

van der Vegt, H. A., Huisman, W. J., Howes, P. B. and Vlieg, E. *Surf. Sci.* **330** (1995) 101

Venkatraman, M. and Neumann, J. P., *Bulletin of Alloy Phase Diagrams*, **11** (3) (1990) 263

Victoria, R. H. and Falicov, L. M., *Phys. Rev.* **B31** (1985) 7335-7343

Vlieg, E., Denier van der Gohn, A. W., van der Veen, J. F., Macdonald, J. E. and Norris, C., *Phys. Rev. Lett.* **61** (19) (1988) 2241-2244

Vlieg, E., van der Veen, J. F., Gurman, S. J., Norris, C. and Macdonald, J. E., *Surf. Sci.* **210** (1989) 301-321

Vlieg, E., van der Veen, J. F., Macdonald, J. E. and Miller, M., *J. Appl. Cryst.* **20** (1987) 330-337

Wang, Z. Q., Li, Y. S., Lok, C. K. C., Quinn, J., Solid State Commun. 62 (1987) 181-185

Warren, B. E., *X-ray Diffraction* (Addison-Wesley, Reading 1969)

Wu, S. C., Lu, S. H., Wang, Z. Q., Lok, C. K. C., Quinn, J., Li, Y. S., Tian, D. and Jona, F., Phys. Rev. B38 (1988) 5363-5370

Wuttig, M., Feldman, B. and Flores, T., Surf. Sci. 331-333 (1995) 659-672

Wuttig, M., Feldmann, B., Thomassen, J., May, F., Zilligen, H., Brodde, A., Hannemann, H. and Neddermeyer, H., Surf. Sci. 291 (1993) 14-28

Wuttig, M., Gauthier, Y., and Blugel, S., Phys. Rev. Lett. 70 (1993) 3619-3622

Wuttig, M. and Thomassen, J., Surf. Sci. 282 (1993) 237-245

Wyckoff, R. W. G., *Crystal Structures*, 2nd ed. (Interscience Publishers, New York, 1971).

Zajac, G., Bader, S. D. and Friddle, R. J., Phys. Rev. B31 (8) (1985) 4947-4953